COMMUNICATIONS

COMMUNICATIONS

Dear readers,

I often try to answer the following question: when will the world be so developed that people lose their ability to promptly react to occurring changes? If we chose the criterion of adaptation (evolution) as the measure of development, we would be surprised not only at the order of values but also at the sharp deceleration in the development of society.

A significant step to prevent this from happening is to give both space and time to highly qualified and motivated people engaged in building a sustainable future: not only to theoreticians but also to practitioners. The problem does not have to be the lack of enthusiasm and talent to work but it can also be unsuitable working conditions and environmental culture.

Hardly anybody knows how or whether successful leaders are able to turn a good idea into a sophisticated reality. Many, not only ordinary, but also recognized and successful people (not only politicians but also scientists) aim at mimicking. They do not realize that it is purely a superficial phenomenon. A person sitting in front of a computer all day will not become a scientist. To become a scientist he has to prove it with the results of his work. If the results are to be above standard, people have to work hard on their personal development. If they want to be successful in their lives and in decision making processes, they have to remain curious in order to discover new things.

I think that the articles included in this volume prove that their authors are recognized professionals in their fields. On the basis of the reviews I can say that they do not mimic anybody or anything.

I hope you will enjoy the reading and will get inspired and motivated.

Vladimir Hlavna

COMMUNICATIONS

Jaromir Prihoda – Pavel Zubik – Jan Sulc – Milan Sedlar *

EXPERIMENTAL AND NUMERICAL MODELLING OF TURBULENT FLOW OVER AN INCLINED BACKWARD-FACING STEP IN AN OPEN CHANNEL

The contribution deals with the experimental and numerical modelling of the turbulent flow over an inclined backward-facing step in an open water channel. The modelling was carried out in the wide range of the Froude number covering the subcritical, supercritical and near critical regimes as well. The study was concentrated particularly on the development of flow separation and on changes of free surface. Numerical results obtained using the commercial software ANSYS CFX 12.0 for the two-equation SST model and the EARSM model were compared with experimental data obtained by means of PIV and LDA measuring techniques.

Keywords: *Open channel flow, inclined backward-facing step*

1. Introduction

Turbulent flow over an inclined backward-facing step in the open channel occurs very often in hydraulic applications. The character of flow over the inclined step depends on the inclination angle changing from the perpendicular backward-facing step with flow separation at the step edge up to a small inclination without flow separation. The flow pattern is relatively complicated in spite of a simple geometry because it includes an extensive separation region and secondary flows near side walls behind the inclined step. The character of flow is as well very influenced by gravitational forces and depends on flow conditions.

Turbulent flow over the inclined backward-facing step situated in the open channel was investigated experimentally and numerically for a wide range of flow parameters. Flow conditions are described notably by the Froude number Fr covering the range from $Fr = 0.42$ up to $Fr = 2.14$. The contribution summarizes results of the investigation of turbulent flow over an inclined backward-facing step with subcritical, supercritical and near-critical regimes as well (see Prihoda et al. [1], [2], [3]). Results of experimental investigation of turbulent flow over an inclined step in the closed channel and in an open channel with sub- and supercritical flow are given by Zubik et al. [4].

While the subcritical regime is characterized by a large separation region near the channel bottom and a slightly rippled free surface, the supercritical flow is practically without separation and free surface traces the inclined step. The critical regime called the hydraulic jump comes about during the transition from the supercritical to subcritical flow. A comprehensive review of experimental results related to the hydraulic jump was given by Chanson [5]. The presented contribution includes the overview and comparison of all mentioned regimes of turbulent flow over the inclined backward-facing step in an open channel.

2. Experimental investigation

Experiments were carried out in a straight channel of constant cross-section 0.2×0.2 m with the length 4.475 m and with the slope of the bottom corresponding to the chosen flow conditions. The open channel was linked to the water tank with a pump driven by a motor equipped with a frequency converter. The pump with the maximum flow rate of $Q = 7.2$ m^3/min. enabled the maximum speed in the channel of 3 m/s. To stabilize the inflow rate, a wire mesh screens and a honeycomb were installed at the entry of the straight inflow part. The channel is made of transparent plastic material allowing the use of contactless optical measuring techniques. The laser Doppler anemometry (LDA) for measurements of one and/or two velocity components in selected points of the flow field and the particle image velocimetry method (PIV) were used for measurements of the velocity field in selected channel sections. The extended uncertainty guess of flow velocity determination at reliability level of 95% was less than 5% for LDA and 15% for PIV techniques.

The sketch of the test section of the channel with an inclined backward-facing step with the inclination angle $\alpha = 20°$ is given in Fig. 1. The distance of the edge of the inclined step from the channel entry is 0.9 m. The height of the inclined step is $H = 100$ mm. The whole length of the investigated section is 2.1 m. Boundary con-

* **Jaromir Prihoda[1], Pavel Zubik[2], Jan Sulc[2], Milan Sedlar[3]**
[1] Institute of Thermomechanics AS CR v.v.i., Praha, Czech Republic, E-mail: prihoda@it.cas.cz,
[2] Institute of Hydraulic Structures, Faculty of Civil Engineering, Brno University of Technology, Brno, Czech Republic
[3] SIGMA – Research and Development Institute, Lutin, Czech Republic

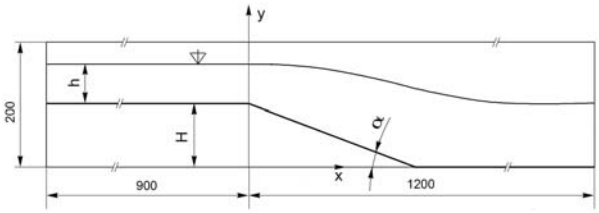

Fig.1 Sketch of the geometrical arrangement

ditions for the numerical simulation were examined in cross-sections $x = -0.9$ and -0.6 m using the PIV and LDA methods. The PIV measurements were taken at vertical and horizontal planes parallel with the channel axis with the aim to determine the general view of the flow with separation and secondary flows behind the step as well. In the mean vertical plane, profiles of mean and fluctuation longitudinal velocities were determined by the LDA method at selected sections x = const.

The free-surface flow over the inclined backward-facing step is characterized by the Reynolds number $Re = U_m H/v$ and the Froude number $Fr = U_m/(gh)^{1/2}$ where U_m is the mean bulk velocity and h is the initial height of the water level. The turbulence level in the stream core was about 2.4 % at the inlet of the channel.

3. Numerical simulation

The numerical simulation of the turbulent flow over the inclined step in an open channel was accomplished by means of the commercial software ANSYS CFX version 12.0 solving Reynolds-averaged Navier-Stokes equations including the gravity effect. A second-order scheme was used for calculations. The numerical solution of free-surface flow was carried out by means of the Volume-of-Fluid (VOF) method based on the monitoring of the volume fraction α_i of both fluids in the each computational cell. The "non-homogeneous" model where the governing equations for the both fluids are solved separately was chosen for the calculation. The SST $k-\varepsilon/k-\omega$ model proposed by Menter [6] and the EARSM (Explicit Algebraic Reynolds Stress Model) model were used for the sub- and supercritical flow. As the turbulent flow near the critical regime should be solved as unsteady, the only SST model was used due to the enormous time demands. The EARSM model is based on a nonlinear relation between the Reynolds stresses and the mean strain rate and vorticity tensors. The used version corresponds to the model proposed by Wallin and Johansson [7].

The distribution of mean velocity, turbulent energy, and dissipation rate was prescribed as inflow boundary conditions according to experimental data. The mean value of static pressure was prescribed as the outflow boundary condition and the open-boundary condition was applied at the upper boundary. The scalable wall functions according to Grotjans and Menter [8] were used as wall boundary conditions. The non-dimensional distance y+ of the first grid point from the wall was $y^+ = 1 \div 5$. The computational domain begins in the cross-section $x = -0.6$ mm before the edge of the inclined step and finishes at the distance $x = 1.2$ m. The domain consists of one half of the channel width with the symmetric boundary condition in the symmetry plane ($z = 0$). A structured monoblock type grid refined near walls and near the free-surface was used for calculations. The grid refinement was adapted to the shape of free surface obtained by preliminary calculations. According to the initial height of the free surface, the height of the computation domain 0.2 m was chosen. The grid consists of $367 \times 169 \times 51$ grid points, i.e. approximately 3.1×10^6 grid points. The detail of the computational grid near the inclined step is shown in Fig. 2.

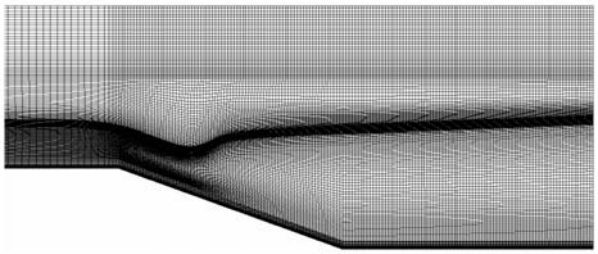

Fig. 2 Detail of the computational grid

4. Results

The analysis of experimental and numerical results was concentrated mainly on the development of flow separation behind the inclined step and on the corresponding changes of free surface. Further, the origin and development of secondary flow near side walls of the channel behind the inclined step was investigated.

4.1 Subcritical flow

The measurement of the subcritical free-surface flow was carried out with the slope of the bottom 0.23 deg for the mean bulk velocity $U_m = 0.38$ m/s and for the initial height of the water level $h = 0.082$ m, i.e. for the Reynolds number $Re = 44100$ and the Froude number $Fr = 0.42$.

Fig. 3 shows mean longitudinal velocity profiles in the symmetry plane over the step and in the outlet channel. Velocity profiles obtained by the EARSM and the SST models are compared with experimental data from PIV technique. It follows from the comparison that the turbulence model based on the assumption of the turbulent viscosity is not able to predict correctly the complicated flow pattern in the relatively narrow open channel with an inclined step. A satisfactory agreement with experimental data was obtained for the EARSM model only. Due to 3D character of flow with secondary effects near side walls, the velocity profiles obtained by the SST model in the middle plane are not believable.

The form of free surface and the extent of the separated region in the middle plane are compared in Fig. 4 with experimental data.

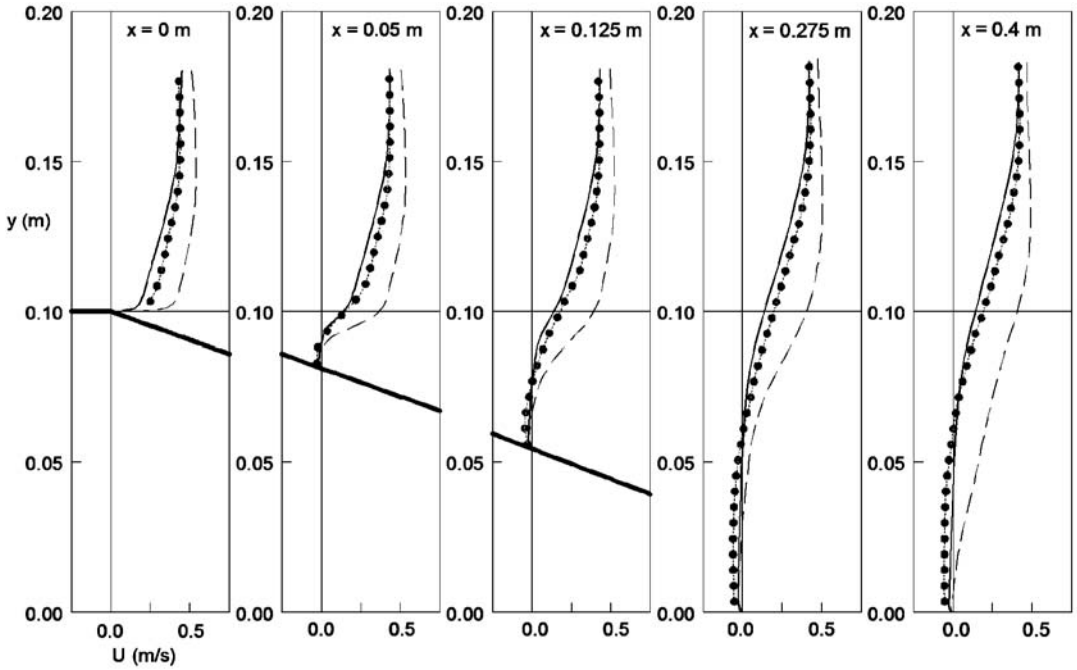

Fig. 3 Mean velocity profiles in the channel for the subcritical regime (full line - EARSM model; dashed line - SST model)

The free surface is in the whole investigated area slightly rippled only. The predicted separated region corresponds to predicted velocity profiles. The extent of the region of the separated flow obtained by the EARSM model is in a good accordance with the experiment, while the SST model gives a smaller separation region. The length of the separation region behind the inclined step is approximately $x_s/H \approx 7.2$, while the length predicted by the EARSM model is $x_s/H \approx 7.6$.

The distribution of turbulent energy in the middle plane of the channel determined by means of the SST and the EARSM model is given in Fig. 5. According the SST model the maximum of turbulent energy is more noticeable in the mixing region immediately behind the flow reattachment. The maximal values of turbulent

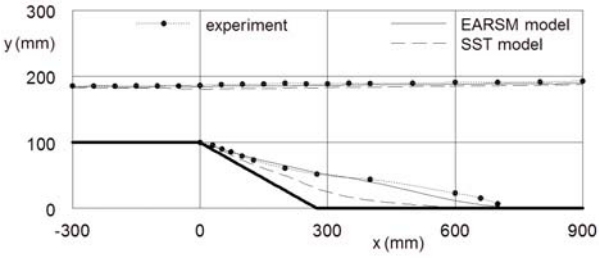

Fig. 4 The extent of the separation region and the form of the free surface for subcritical flow (full line - EARSM model; dashed line - SST model)

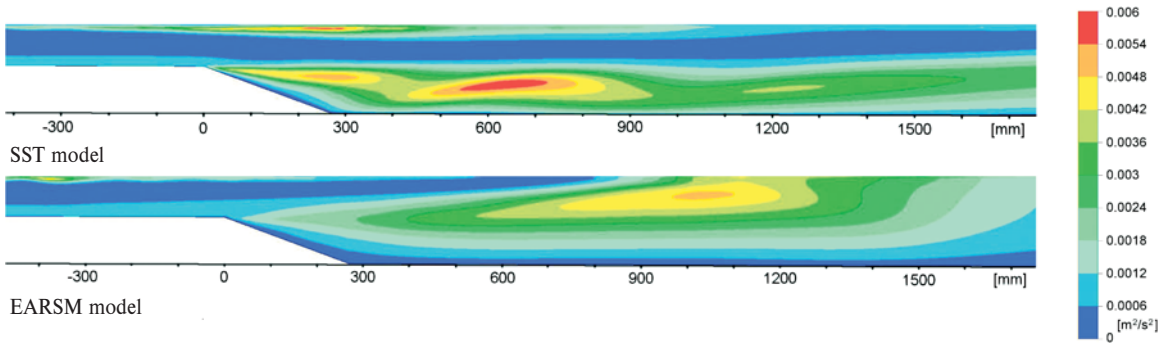

Fig. 5 Distribution of turbulent energy in the middle plane of the channel

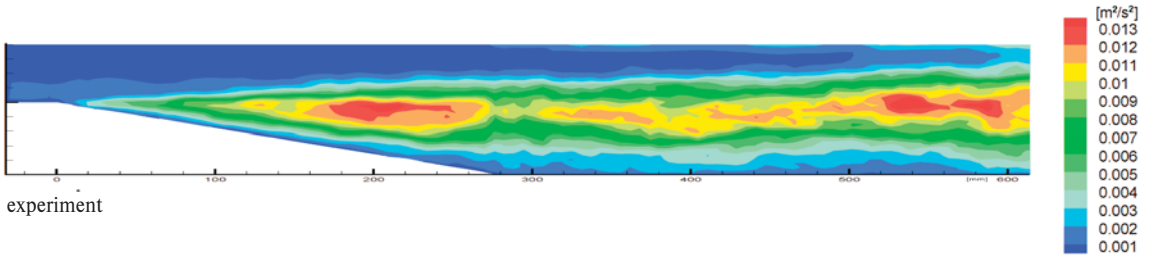

Fig. 6 Distribution of normal stress in the middle plane of the channel

energy obtained by the EARSM model are smaller and the maximum moves to the proximity of free-level. The distribution of the longitudinal component of turbulent normal stress obtained by the PIV technique behind the step is given in Fig. 6 for comparison.

4.2 Supercritical flow

The measurement of the supercritical free-surface flow was carried out with the slope of the bottom 2.025 deg for the mean bulk velocity $U_m = 1.92$ m/s and for the initial height of the water level $h = 0.086$ m, i.e. for the Reynolds number $Re = 200100$ and the Froude number $Fr = 2.14$. At the chosen mean bulk velocity, the turbulence level in the stream core was about 2 %. Fig. 7 shows mean longitudinal velocity profiles in the symmetry plane over the step and in the outlet channel. Velocity profiles obtained by the EARSM model are compared with experimental data from PIV measurement. A surprisingly satisfactory agreement with experimental data was obtained for the EARSM model. The SST model gives nearly same velocity profiles unlike the subcritical flow with a large separation region, where the differences between various turbulence models were distinct.

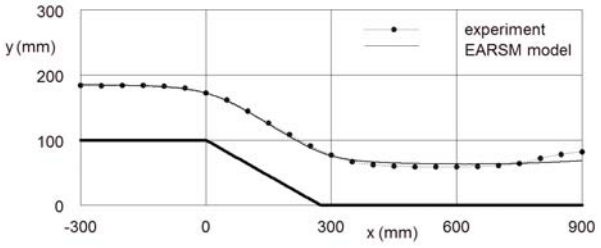

Fig. 8 The extent of the separation region and the form of the free surface for supercritical flow

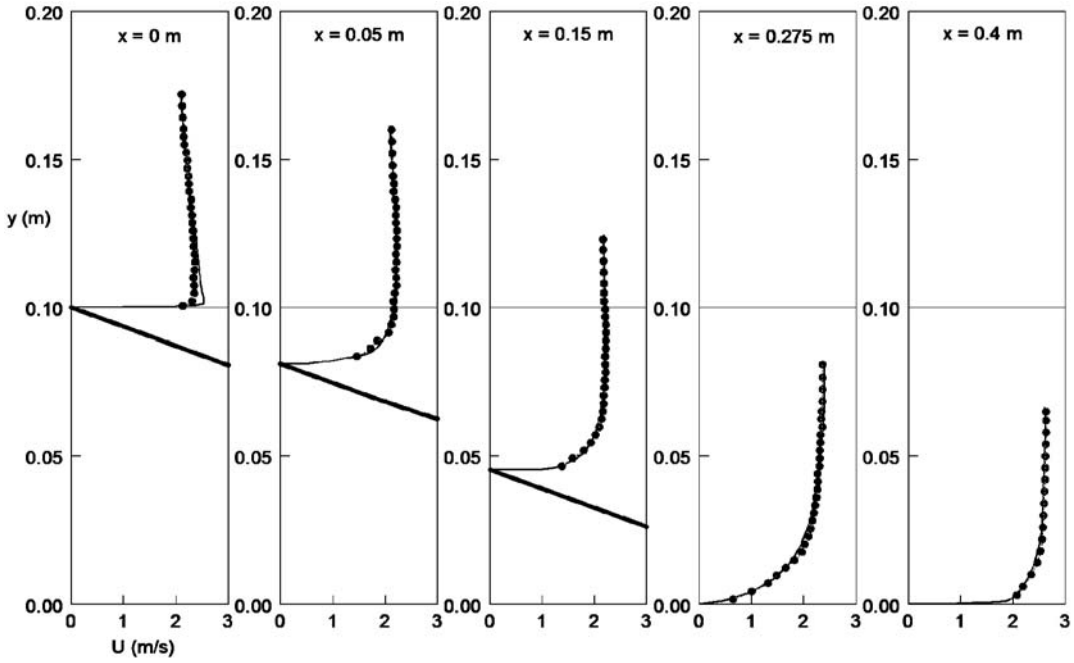

Fig. 7 Mean velocity profiles in the channel for the supercritical regime

The form of free surface in the middle plane is compared in Fig. 8 with experimental data. The supercritical flow over the inclined step is practically without any separation. The form of free surface imitates the bottom of the channel. The free surface is slightly waving behind the root of the step. Besides transversal waves, two distinct oblique waves arise at side walls. The form of free surface predicted by the EARSM model corresponds very well with experiment, even though the response of the numerical model on any change is rather slower than in reality.

4.3 Near-critical flow

The measurement of the free-surface flow near critical conditions was carried out with the slope of the bottom 0.16 deg for the mean bulk velocity $U_m = 0.97$ m/s and for the initial height of the water level $h = 0.056$ m, i.e. for the Reynolds number $Re = 101400$ and the Froude number $Fr = 1.31$. The turbulence level in the stream core was about 2.4 % at the inlet of the channel. The numerical simulation started for flow conditions corresponding to experimental results. For these conditions, the numerical simulation gives flow field corresponding to the supercritical flow. Mean longitudinal velocity profiles in the symmetry plane over the step are shown in Fig. 9. Velocity profiles obtained by the SST model are compared with experimental data from LDA measurements. It can be seen that a satisfactory agreement of predicted mean velocity profiles with experimental data was obtained for the supercritical flow except a short region behind the step edge.

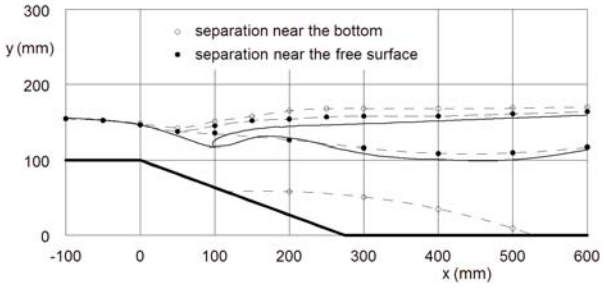

Fig. 10 Extent of the separation region and the form of the free surface for the near-critical flow (symbols as in Fig. 9)

The form of free surface and the extent of the separated region in the middle plane are compared with experimental data in Fig. 10. The free surface for both cases is very similar with a mild waving just behind the step edge only. For the flow regime with separation near the bottom, the separation region does not start at the step edge as for the subcritical flow but approximately at $x/H = 1.2$ and reaches up to $x/H = 5.2$. The extent of the back flow near the free surface in the supercritical case is much longer and separation region takes up to $x/H = 9$.

As the numerical simulation gives for these boundary conditions the supercritical regime only, the further simulation of the

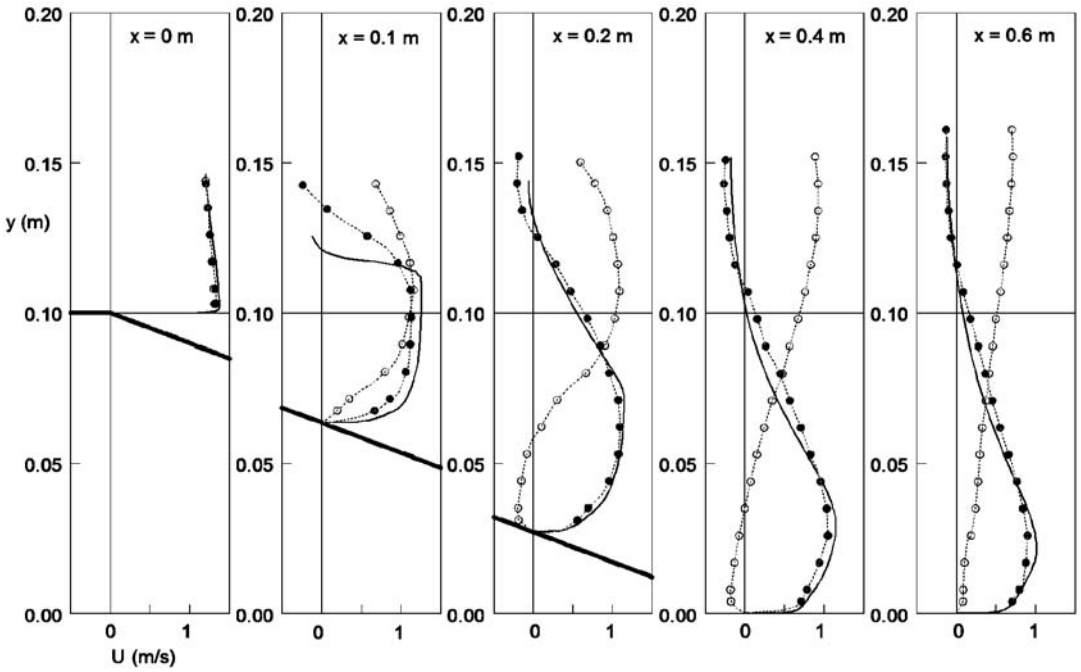

Fig. 9 Mean velocity profiles for the near-critical flow at $U_m = 0.97$ m/s
(full line - SST model simulation, - supercritical regime - subcritical regime)

unsteady flow was realised for various inlet velocities. The critical regime with the transition from the supercritical to subcritical flow was achieved for the mean bulk velocity $0.78U_m$ corresponding to the Froude number $Fr = 1.02$. The simulation using the time step $\tau = 0.05$ s gives a periodic process with the period approx. 15 s. Unfortunately, the simulation of one second of the flow needs 5:45 hours of the computational time using the computational cluster with two parallel processors. Therefore the numerical simulation was limited to 55 sec, i.e. approximately 3½ periods of the process only.

Mean velocity profiles in the symmetry plane of the channel are shown for the mean bulk velocity $0.78U_m = 0.76$ m/s in Fig. 5. The flow regime is unstable starting with the supercritical character (time $t_o + 0.15$ sec) and switches to the subcritical character approximately after 39 sec (time $t_o + 39.15$ sec). Further, the process is periodic with the period about 15 sec (see full line for time $t_o + 46.15$ sec).

The character of mean velocity profiles for both regimes is very similar to experimental data obtained for the mean velocity U_m. Predicted extent of the separation region and the form of the free surface in the middle plane for the mean bulk velocity $0.78U_m$ are given in Fig. 5. The form of free surface is like the mean velocity profiles similar to the basic case with the mean velocity U_m but the extent of the separation region for both regimes is much longer. The separation near the bottom starts at approx. $x/H = 0.2$ while the separation near the free surface occurs at $x/H = 0.6$. The length of the separation region is approx. $x/H \approx 10$ for both regimes.

The character of the turbulent energy fields corresponds to mean velocity profiles. The level of turbulent energy is maximal in the mixing layer between the attached and back flow in all cases but the maximum of turbulent energy is approximately twice higher for the case with the separation near the free surface (supercritical regime) than for the case with separation near the bottom (subcritical regime).

5. Conclusions

Experimental and numerical investigation of turbulent flow over an inclined backward-facing step in an open channel was carried out for a wide range of flow conditions covering the subcritical, supercritical and near-critical regimes as well. The preliminary analysis of experimental and numerical results was concentrated mainly on the development of flow separation behind the inclined step and on the corresponding changes of free surface.

The subcritical free-surface flow over a backward-facing inclined step showed the complicated three-dimensional character of flow. The relatively long separation region occurs behind the inclined step while the free-level is slightly rippled only. Secondary flows arise behind the step edge near side walls partly close to the channel bottom and partly to the free-level. It follows from the testing of turbulence models that models based on the turbulent viscosity are not able to predict correctly the complicated flow pattern in this case. A satisfactory agreement with experimental data was obtained for the EARSM model only.

The supercritical free-surface flow is practically without any separation and free surface imitates the bottom of the channel. A very satisfactory agreement with experimental data was obtained for the EARSM model. Unlike the subcritical flow, the free surface of the supercritical flow is slightly waving behind the root of the step. Besides transversal waves, two distinct oblique waves arise at side walls. The predicted free surface corresponds very well with experiment, even though the response of the numerical model on any change is rather slower than in reality.

The critical regime with the abrupt change of the flow character from the supercritical flow to the subcritical flow was experimentally obtained for the mean bulk velocity $U_m = 0.97$ m/s corresponding to the Froude number $Fr = 1.31$. The supercritical regime with the separation near the free surface switches to the subcritical one with the separation near the bottom by a very small change of the velocity. The numerical simulation of the unsteady two-phase turbulent flow using the SST turbulence model gives for these conditions the flow field corresponding to the supercritical flow only. A satisfactory agreement of predicted mean velocity profiles with experimental data obtained by the LDA measuring technique was obtained for the supercritical regime except a short region behind the step edge. On the basis of the series of simulations of the unsteady flow for boundary conditions, the critical regime was determined for the mean velocity $0.78U_m$ i.e. for the Froude number $Fr = 1.02$. In this case the prediction gives the unstable flow regime starting the supercritical character and switches to the subcritical character approx. after 39 sec. Further, the process is periodic with the period about 15 sec. The character of the flow field for these boundary conditions is very similar to experimental data obtained for the nominal mean velocity. Nevertheless, the predicted extent of the separation region in both regimes with the separation near the free surface and near the bottom is noticeably longer than experimental results for the nominal velocity.

The presented results are the first attempt on the detailed experimental and numerical modelling of the two-phase turbulent flow over an inclined backward-facing step including the near-critical regime and be applied in the further research and in hydraulic applications.

Acknowledgement

The work was supported by the grant project No. 103/09/0977 of the Czech Science Foundation and with the institutional support RVO 61388998.

References

[1] PRIHODA, J., ZUBIK, P., SULC, J., SEDLAR, M.: *Modelling of Subcritical Free-surface Flow over an Inclined Backward-facing Step in a Water Channel,* Proc. conference Experimental Fluid Mechanics 2010, 555–560, Liberec, 2010

[2] PRIHODA, J., ZUBIK, P., SULC, J., SEDLAR, M: *Modelling of Supercritical Turbulent Flow over an Inclined Backward-facing Step in an Open Channel,* Proc. conference. Engineering Mechanics 2011, 495–498, Praha, 2011

[3] PRIHODA, J., ZUBIK, P., SULC, J., SEDLAR, M: *Modelling of Critical Regime in the Free-surface Flow over an Inclined Backward-facing Step,* Proc. *conference Application of Experimental and Numerical Methods in Fluid Mechanics and Energy* 2012, 212–217, Zilina, 2012

[4] ZUBIK, P., SULC, J., PRIHODA, J., SEDLAR, M.: *Experimental and Numerical Modeling of Fluid Flow with Separation.* Proc. 9th conference Power System Engineering, Thermodynamics and Fluid Flow, CD-ROM, 8 p., Plzeň, 2010

[5] CHANSON, H.: Current Knowledge in Hydraulic Jumps and Related Phenomena. A Survey of Experimental Results, *European J. of Mechanics B/Fluids,* 28, 191-210, 2009

[6] MENTER, F. R.: Two-equation Eddy-viscosity Turbulence Models for Engineering Applications, *AIAA Journal*, 32, 1598–1605, 1994

[7] WALLIN S., JOHANSSON, A.: A Complete Explicit Algebraic Reynolds Stress Model for Incompressible and Compressible Flows, *J. of Fluid Mechanics,* 403, 89–132, 2000

[8] GROTJANS, H., MENTER, F. R.: *Wall Functions for General Application CFD Codes.* Proc. European Conference on Computational Fluid Dynamics ECCOMAS 98, John Wiley, 1112–1117, 1998.

Frantisek Kavicka – Josef Stetina – Bohumil Sekanina – Milos Masarik *

DEFINITION OF BOUNDARY CONDITIONS FOR THE NUMERICAL MODEL OF TRANSIENT TEMPERATURE FIELD OF A CONCAST STEEL SLAB

The solidification and cooling of a continuously cast billet, slab or cylinder (generally a concasting) is a very complicated problem of 3-D transient heat and mass transfer. This paper is focused on the derivation of boundary conditions, i.e. the values of the heat transfer coefficient (HTC) on all boundaries of the concasting machine (CCM). The definition of boundary conditions is the most difficult part of the investigation of the thermokinetics of this process. The boundary conditions in the numerical model of the temperature field of the concasting are defined as the heat transfer by convection. This HTC includes the so-called reduced convection coefficient corresponding to heat transfer by radiation. This paper therefore continues with a discussion on heat transfer coefficients under air-water cooling jets, which spray the concasting in the so-called secondary-cooling zone.

Keywords: *Concast slab, boundary conditions, cooling characteristics*

Nomenclature

a	thermal diffusivity, $m^2.s^{-1}$
c	specific heat capacity, $J.kg^{-1}.K^{-1}$
i_v	specific volume enthalpy, $J.m^{-3}$
Q	heat flow, W
Q_{source}	internal heat source, $W.m^{-3}$
T	temperature, °C
V	volume, m^3
x,y,z	axes in given direction
w	shift rate, $m.s^{-1}$
λ	heat conductivity, $W.m^{-1}.K^{-1}$
τ	time , s
ρ	density, $kg.m^{-3}$

1. Introduction

One of the more significant differences between a concasting machine (CCM) for the casting of billets and that for the casting of slabs (Fig. 1) is in the cooling within the secondary-cooling zone. This is due to the convection of a greater amount of heat from the voluminous slab casting, where the secondary-cooling zone in *EVRAZ VITKOVICE STEEL* is subdivided into thirteen sections. The first section engages water jets from all sides of the concasting. The remaining twelve sections engage air-water cooling jets, which are positioned only on the upper and underside of the concasting. It is therefore very important to determine the correct boundary conditions for the numerical model of the temperature field [1–6].

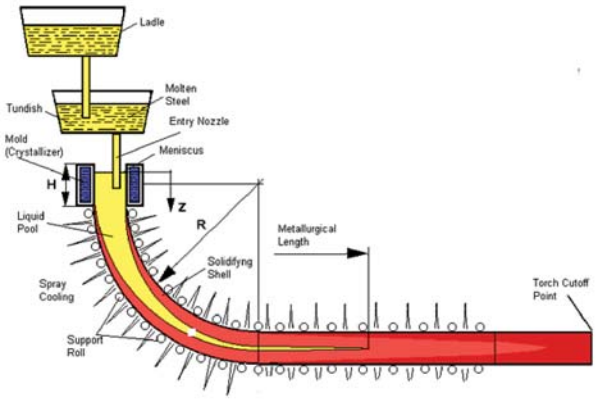

Fig.1 A concasting machine (CCM)

2. A numerical model of the temperature field of a slab

The solidification and cooling of a concasting and simultaneous heating of the crystallizer is a very complicated problem of 3D

* **Frantisek Kavicka[1], Josef Stetina[1], Bohumil Sekanina[1], Milos Masarik[2]**
[1] Department of Power Engineering, Faculty of Mechanical Engineering, Brno University of Technology, Brno, Czech Republic, E-mail: kavicka@fme.vutbr.cz
[2] EVRAZ VITKOVICE STEEL, a.s. Ostrava, Ostrava, Czech Republic

transient heat and mass transfer. The 3D transient temperature field of the concasting, passing through the CCM (the zones of primary, secondary and tertiary cooling), can be described by the Fourier-Kirchhoff equation

$$\frac{\partial T}{\partial \tau} = \frac{\lambda}{\rho \cdot c}\left(\frac{\partial^2 T}{\partial x^2} + \frac{\partial^2 T}{\partial y^2} + \frac{\partial^2 T}{\partial z^2}\right) + \left(w_x \frac{\partial T}{\partial x} + w_y \frac{\partial T}{\partial y} + w_z \frac{\partial T}{\partial z}\right) + \frac{Q_{SOURCE}}{\rho \cdot c} \quad (1)$$

The derivation of the temperature by time becomes zero upon the reaching of the steady state. Equation (1), when considering movement in the direction of the z-axis only, can be simplified to

$$\frac{\partial T}{\partial \tau} = a.\Delta T + w_z \frac{\partial T}{\partial z} + \frac{Q_{source}}{\rho \cdot c} \quad (2)$$

The 3D transient temperature field of a crystallizer cooled by water is expressed by the Fourier equation, i.e (2) without the member $w_z(\partial T/\partial z)$. The authors had chosen the explicit difference method, which enables the application of the most convenient method of numerical simulation of the release of latent heat of phase or structural changes using the thermodynamic enthalpy function. In order to describe the temperature field of a concasting in all its three stages, i.e. in: the melt → the mushy zone → the solid phase equation (2) must be converted to

$$\frac{\partial i_v}{\partial \tau} = \lambda.\Delta T + w_z \frac{\partial i_v}{\partial z} + Q_{source} \quad (3)$$

The specific volume enthalpy $i_v = c \cdot \rho \cdot T$ is dependent on temperature. The specific heat capacity c, density ρ and heat conductivity λ are also functions of temperature. The authors have developed an original numerical model [7], which solves the Fourier and Fourier-Kirchhoff equation. The program also takes into account the non-linearity of the task, i.e. the dependence of the thermophysical properties of all materials entering the system being investigated, and the dependence of the heat-transfer coefficients on all boundaries of the system on the temperature of the working surface–of the concasting or crystallizer–and on other influences (e.g. shift rate, intensity of spraying). The exactness of the presented numerical model depends on the accuracy with which the thermophysical properties of the materials of all parts of the system are determined. These properties can be set either via a table or with the help of coefficients of approximation polynomials describing the curve [8].

3. Definition of boundary conditions of solution

Furthermore, the exactness of the numerical model depends on the derivation of boundary conditions. Therefore the setting of the properties is followed by the setting of the boundary conditions, i.e. the values of the heat transfer coefficient (HTC) on all CCM boundaries. The dependences of these coefficients on temperature and other operation parameters must also be given. The definition of boundary conditions is the most difficult part of the investigation of the thermokinetics of this process. The boundary conditions in the numerical model of the temperature field of the concasting are defined as the heat transfer by convection (Fig. 2). This HTC includes the so-called reduced convection coefficient corresponding to heat transfer by radiation.

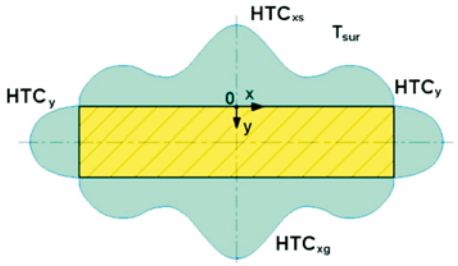

Fig. 2 Boundary conditions on the slab surface

For example the boundary condition of the slab-crystallizer interface depends on the thermophysical properties and the state of the casting powder, and also on the shape and size of the gap (Fig. 3).

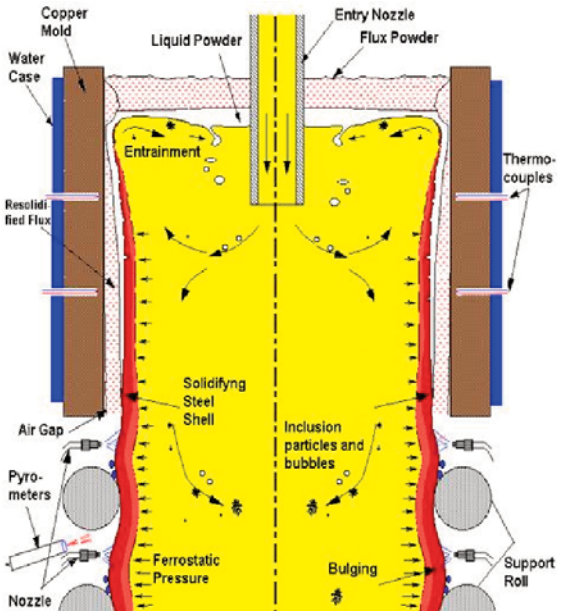

Fig. 3 The boundary condition of the slab-crystallizer interface

The only, but extremely important, coefficient, after leaving the crystallizer, is the HTC on the surface of the concasting, and is mainly dependent on the temperature of the surface, the shift rate and the intensity of spraying. This paper therefore continues with a discussion on heat transfer coefficients under air-water cooling jets, which spray the concasting in the so-called secondary-cooling zone. On a real CCM, where there are many types of jets with various settings positioned inside a closed cage, it is practically impossible to conduct measurement of the real boundary condi-

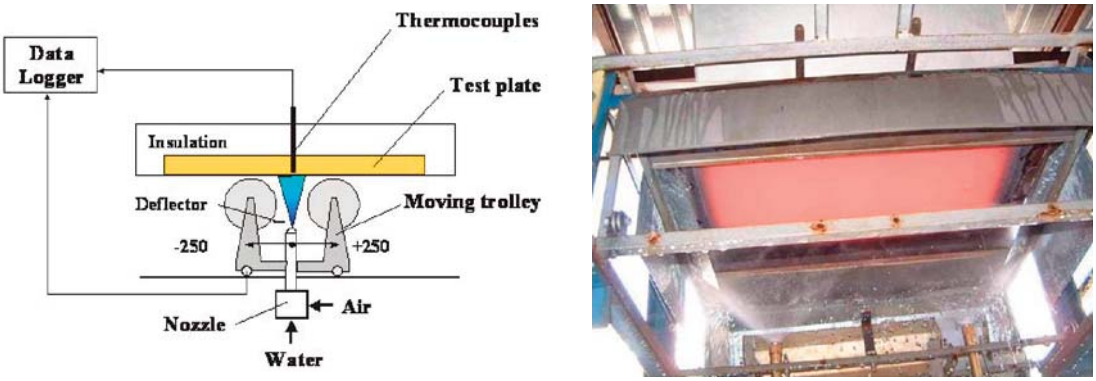

Fig. 4 Experimental laboratory device

tions. Therefore, a laboratory device was introduced in order to measure the cooling characteristics of the jets (Fig. 4). This experimental laboratory device simulates not only the movement, but also the surface of a slab. Real CCM contains a total 8 types of jets and geometrical layouts.

This laboratory device enables the measurement of each jet separately. It comprises a steel plate mounted with 18 thermocouples, heated by an external electric source. The steel plate is heated to the testing temperature, then it is cooled by a cooling jet. Based on the temperatures measured in dependence on time, the *HTC*s are calculated by an inverse task. They are then processed further using an expanded numerical and an identification model and converted to coefficients of the function $HTC(T,y,z)$, which expresses the *HTC* in dependence on the surface temperature, and also the position of the concasting with respect to the jet.

Figures 5 and 6 illustrate the area of influence of the cooling jet and the 3D course of the heat transfer coefficient under the cooling jet. Fig. 7 illustrates the *HTC* in dependence on the surface temperature.

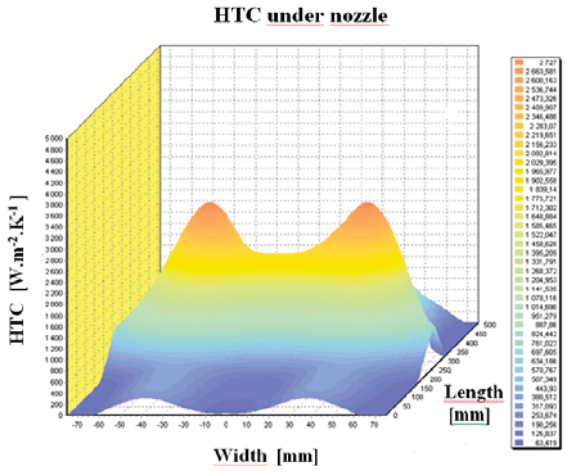

Fig. 5 3D diagram of HTC under the cooling jet

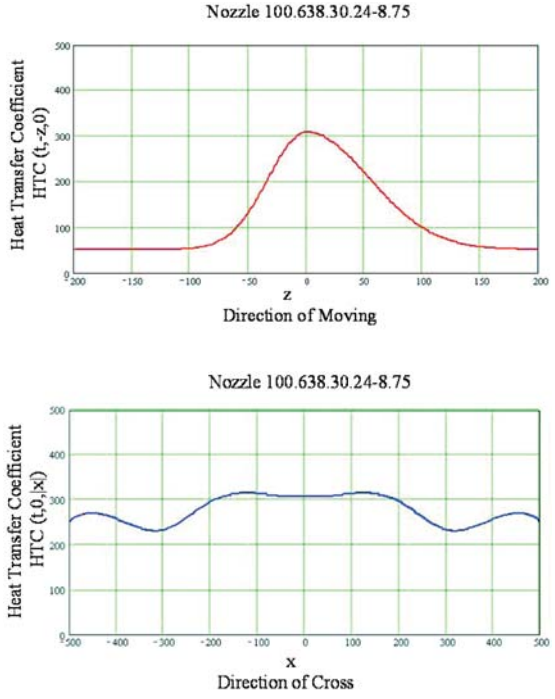

Fig. 6 The HTC for two directions under the cooling jet

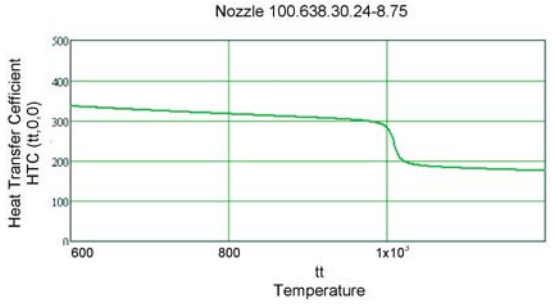

Fig. 7 The HTC in dependence on the surface temperature

4. Application of the numerical model on a concast steel slab

The numerical model described above is applied in order to investigate a concast steel slab with a profile of a × b in any stage of the process, where a is the width ranging from 800 to 1600 mm and b is the thickness ranging from 120 to 250 mm [9 and 10]. A diagram of the longitudinal section of the CCM for radial concasting was illustrated in Fig. 1.

It was decided to simulate the temperature field of a 1530 × × 250 mm steel slab. The conditions of pouring were characterized by the temperature in the tundish (1548 °C), by the temperature of the liquid (1515 °C), by the temperature of the solidus (1479 °C), and by the shift rate of the slab (0.7 m.min^{-1}).

The maximum number of nodal points is 2.5 × 10^6 (Fig. 8), which could also be sufficient in order to cover a more complex cross section. Such a density of the net enables the linear interpolation of the temperatures among the points of the net, and also among the time sectors.

After the computation, it is possible to obtain the temperatures at each node of the network and at any time during the process. Very useful is the temperature history graph (Fig. 9), which shows the temperature at defined points of the cross-section of the slab. The course of the temperatures can also be displayed in any other user-defined point.

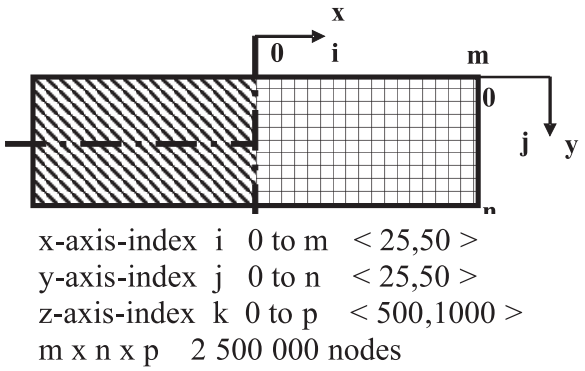

Fig. 8 The slab profile and the numerical network

Figure 9 illustrates the repetitive drops in temperature in the secondary-cooling zone, which are caused by the intensive cooling by jets. Each successive temporary increase in temperature, which is reflected in the saw-tooth character of the curve, is caused by the movement of the slab – the given point moves out of reach of the previous jet and passes through an unsprayed zone before it moves into the scope of the next jet in line. The vertical shaded band in Fig. 9 shows the range of depths (17–17.625 m) beneath the level of the melt in the crystallizer, within which the slab becomes completely solid. The radio-isotope measurement confirmed this so-called metallurgical length to be 17.4 m.

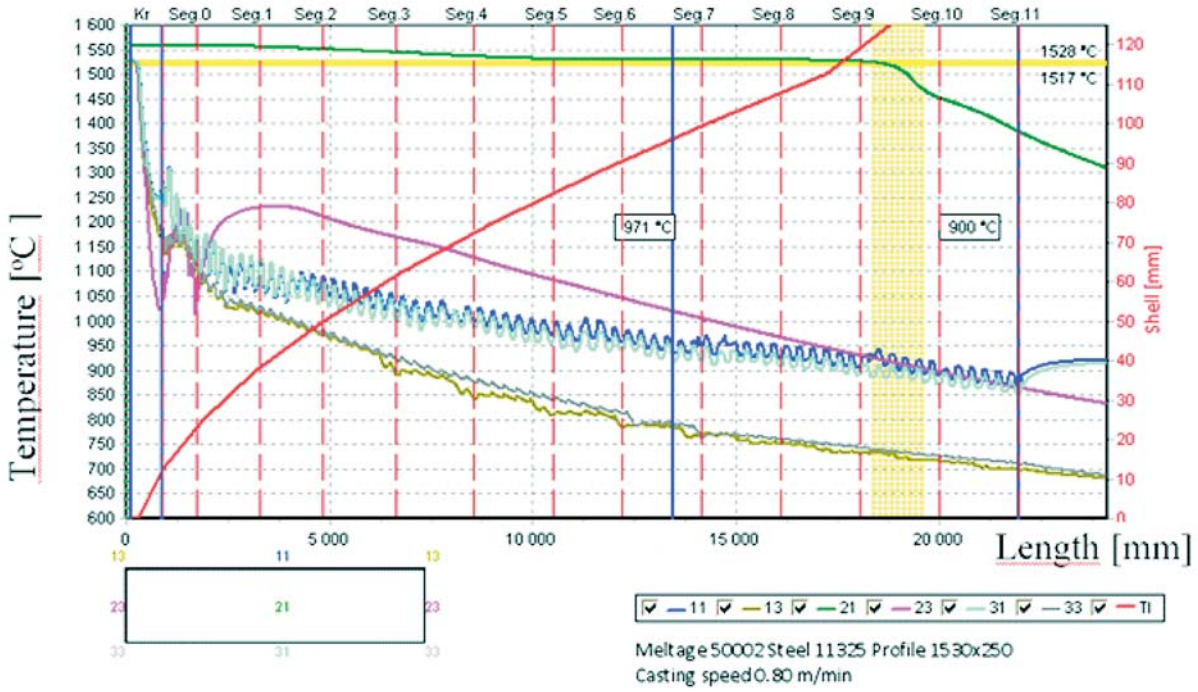

Fig. 9 The temperature history in the selected points of the cross-section

The comparison of the computed and pyrometer-measured temperatures at a distance of 1000 mm beneath the level of the melt within the crystallizer proved that the model is appropriate.

5. Conclusion

The value of the *HTC* coefficient on the surface of the slab, as it enters the secondary-cooling zone, significantly affects the process simulation from the viewpoint of the temperature field, the technological length, and also other technological properties. It therefore affects prediction of the quality of the slab.

In order to be able to simulate this boundary condition within the numerical model as accurately as possible, it is necessary to conduct experimental measurement on each jet in the secondary-cooling zone individually.

Each of the eight jets had been measured separately on the hot model, on which the hot surface of the slab, which is cooled by a moving jet, can be modeled. The temperatures measured on the surface of the model can be entered into an inverse task to calculate the intensity of spraying, which, in turn, can determine the *HTC* by a special mathematical method.

These values (of the coefficients of all jets), which correspond satisfactorily with experimentally attained temperatures and technological length, have been successfully applied in the calculation of the temperature field of slabs.

Acknowledgement

This analysis was conducted using a program devised within the framework of the GA CR projects No 107/11/1566, 106/08/0606 and 106/09/0940.

References

[1] LECHNER, M., REITER, J., BERNHARD, C., FORSTHUBER, M., ZACH, O.: Bestimmung und Bedeutung der Randbedingungen fuer die Simulation von Stranggiesprozessen, *BHM*, 3, 2004, pp.101–106.

[2] RICHARD, A., HARDING, KAI LIU, BECKERMANN, CH.: A Transient Simulation and Dynamic Spray Cooling Control Model for Continuous Steel Casting. *Metallurgical and Materials Transactions,* vol. 34B, 2003, pp. 297–302.

[3] HORSKY, J., RAUDENSKY, M., TSENG A. A.: *Heat Transfer Study of Secondary Cooling in Continuous Casting.* AISTech 2005, Iron & Steel Technology Conference and Exposition, 2005, Charlotte, USA.

[4] MAUDER, T. et al.: *An Optimal Relationship between Casting Speed and Heat Transfer Coefficients for Continuous Casting Process.* METAL 2011 Conference Proc. Papers Symp. A, Metal. Ostrava, Tanger. 2011. p. 42–48, ISBN 978-80-87294-24-6 (CD ROM Paper 649).

[5] PYSZKO, R., BURDA, J., FOJTIK, P., PRIHODA, M., CARNOGURSKA, M. *Surface Condition for the Model of Strand Temperature field in the CCM Secondary Zone.* Proc. of the XVIII. Intern. Sci. Conference The Application of Experimental and Numerical Methods in Fluid Mechanics and Energetics 2012. University of Zilina. Demanovska dolina, 2012, pp. 218–223. ISBN 978-80-554-0516-2

[6] CARNOGURSKA, M., PRIHODA, M., BRESTOVIC, T., MOLINEK, J., PYSZKO, R.: Determination of Permeability and Inertial Resistance Coefficient of Filter Inserts used in the Cleaning of Natural Gas. *J. of Mechanical Sci. and Technology,* vol. 26, No.1, pp. 103–111, 2012, ISSN 1738-494X, ISSN 1226-4865.

[7] STETINA, J.: *A Dynamic Model of Temperature Field of Concast Steel Slab.* PhD Thesis. VSB-TU Ostrava, Faculty of Metallurgy and Materials Engineering, Ostrava, 2007, p. 105.

[8] MIETTINEN, J., LOUHENKILPI,S., LAINE, J.: *Solidification Analysis Package IDS.* Proc. of General COST 512 Workshop on Modeling in Materials Science and Processing, M. Rappaz and M. Kedro eds., ECSC-EC-EAEC, Brussels, Luxembourg, 1996.

[9] KAVICKA F. et al.: The Optimization of a Concasting Technology by Two Numerical Models. *J. of Materials Processing Technology 185 (2007)*, pp.152–159.

[10] STETINA, J. et al.: *Optimization of a Casting Technology of a Steel Slab via Numerical Models.* Proc. 22nd Canadian Congress of Applied Mechanics, Dalhousie University Halifax, Nova Scotia, 2009, p. 4.

Milan Malcho – Jozef Jandacka – Martin Vantuch – Andrej Kapjor – Stanislav Gavlas *

TRANSFER OF LOW-POTENTIAL HEAT FROM A DEEP BOREHOLE BY MEANS OF A HEAT PIPE AND HEAT PUMP

The paper presents a design of equipment for the usage of low-potential heat collected from rock in a deep borehole by means of heat pipes (HP) and a description of its realization. The borehole model together with a CFD simulation of heat transfer from rock to a soil probe enabled dimensioning of a heat exchanger on the condenser part of the heat pipe and choice of a suitable heat pipe charge. Part of the paper deals with the processing of measurement results gathered from the comparative experimental equipment requiring forced and unforced circulation(heat pipe) of the working substance on the primary side of the heat pump.

Keywords: *Heat pipe, heat pump, low-potential heatofthe rock,output, deep borehole, soil probe.*

1. Introduction

Low-potential heat of the rock is a heat flow in the surface area of the Earth crust with a relatively low thermal potential corresponding to the standard geothermal gradient. This heat flow can either originate from solar radiation falling on the Earth surface or from radiogenic processes inside the Earth.

The heat falling on the Earth surface due to solar radiation is timely highly unstable and influences the heat flow in the Earth rocks up to the depth ranging from 10 to 20 meters. Yearly and daily changes in solar radiation intensity and outer air temperature cause temperature variations in the thin layer of the Earth's surface. Heat regime in the depth greater than the depth of the neutral zone (in Slovakia approx. 14 m), is formed due to the effects of heat characteristics of the Earth's core. The flow of radiogenic heat produced inside the Earth is practically stable and is not influenced by any seasonal or other changes of weather and temperature. The temperature of the Earth increases with the depth from the surface in compliance with the geothermic gradient of a particular geological structure (approximately 3 °C for every 100 m). The amount of radiogenic heat from inside the Earth differs for different areas of the Earth crust. The heat flow for Central Europe ranges from 0.05 to 0.12 $W.m^{-2}$.

A great advantage of low-potential geothermal heat is that it is not limited by a geothermal region or any region with a high potential of hot geothermal waters. It can theoretically be recovered anywhere on Earth's surface. It is the heat accumulated in the soil and ground waters. Rock temperatures range from 5 °C to 60 °C. Heat can be collected directly from the soil by means soil collectors, from boreholes up to the depth of 400 m or from ground waters. Low-potential heat (up to 60 °C) can be used to heat buildings, water, playgrounds, etc.Compared with high-potential heat the costs for low-potential heat collection are considerably lower.

When using low-potential geothermal energy there are two basic systems – the system with a forced circulation of a heat carrying medium or the system with thermosiphoneffect without a forced convection in a ground heat exchanger. In both systems the heat pump compressor circulation is predominantly used for the heat potential transformation [1], [2].

Heat carrying substances used for forced circulations in the heat pump primary circuit are usually mixtures of water and antifreeze, such as, e.g. ethylene glycol, tyfocor, salt brine, etc. Owing to the fact that relatively efficient circulation pumps need electricity for their operation, new ways of heat transfer without a forced circulation of heat carrying medium in the ground heat exchanger are looked for. Heat pipes with suitable charge seem to be a perspective way of collecting heat from rocks without a forced circulation of a working substance. In such a system the heat carrier flows in the pipe without additional energy supply with small temperature difference making use of the properties of heat transfer at phase changes. The device working on the mentioned principle of heat transfer is called a heat pipe. Heat pipes have been recently commonly used for the cooling ofelectronic components and electronic devices (processors, transformers, etc.) and are examples of real usage of heat transport without a forced circulation of a heat carrier. In heat technology heat pipes are used also for solar energy transfer in high-efficiency solar collectors and in systems for heat recovery.

* **Milan Malcho, Jozef Jandacka, Martin Vantuch, Andrej Kapjor, Stanislav Gavlas**
Department of Energy Technology,Faculty of Mechanical Engineering, University of Zilina, Slovakia, E-mail: milan.malcho@fstroj.uniza.sk

2. A design of device for low-potential heat collection

The device for low-potential heat collection from the rock in a deep borehole was realized by means of a conventional and unconventional way using heat pumps [3]. Due to the fact that there are two independent soil probes making use of two different ways of heat collection, we used two heat pumps to extract the heat (abbr. HP) of the type Ground/Water working independently from each other Fig. 1. The whole device together with all the measuring systems (with the exception of deep boreholes) was placed in laboratory premises. The pipes of primary circuit were led to the boreholes located in front of the laboratory building.

The whole device thus consists of two heat pumps connected through the primary circuit to two boreholes 150 meters deep drilled in the vicinity of Zilina University laboratories. The boreholes were performed by means of a drilling set equipped with a collapsible drilling tower with a grief stem, rotary table, and its own power unit (diesel engine). This drilling set is designed for engineering and geological boreholes and boreholes to extract heat from soil.

To avoid mutual thermal influencing of the boreholes, there is a distance of 14 meters between them. In the boreholes there are groundU-heat exchangers using two different ways of heat collection from soil:

- with a forced circulation of the working medium in the primary circuit (soil probe),
- with a natural thermosiphon circulation of the working medium in the primary circuit (heat pipe).

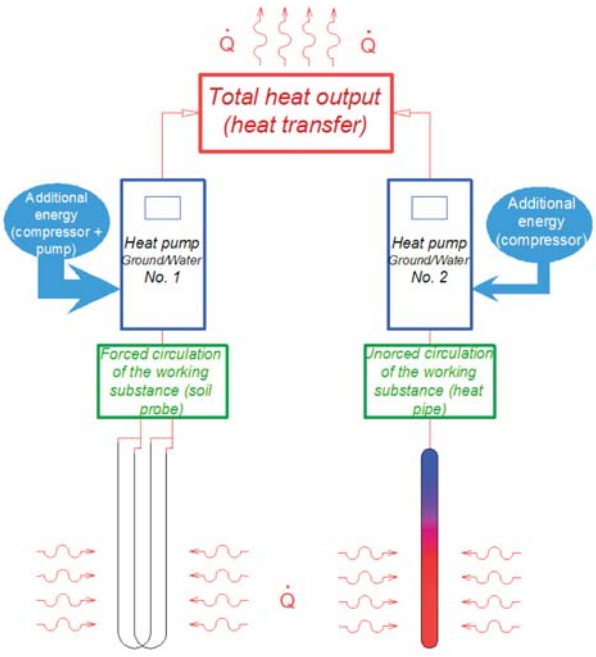

Fig.1 Scheme of experimental device for low-potential heat collection from deep borehole

3. A design of the heat pipe

3.1 Numerical model of heat transfer from the rock into the heat pipe

As the structure of the rock changes with the depths, its thermokineticcharacteristics also change. The process of the rock cooling will, therefore, be modeled according to various layers with different thermokinetic characteristics of the given layer of a 150 meter borehole.

Heat transfer from the rock into the heat pipe is described by Fourier's equation for heat conduction in cylindrical coordinates

$$\rho c_p \frac{\partial t}{\partial \tau} = \frac{\partial}{\partial x}\left(\lambda \frac{\partial t}{\partial x}\right) + \frac{\partial}{\partial y}\left(\lambda \frac{\partial t}{\partial y}\right) + \frac{\partial}{\partial z}\left(\lambda \frac{\partial t}{\partial z}\right) + q_v . \quad (1)$$

Supposing that physical characteristics of a body are constant, we can write relation (1) in the form

$$\frac{\partial t}{\partial \tau} = \frac{\lambda}{c_p \rho}\left(\frac{\partial^2 t}{\partial r^2} + \frac{1}{r}\frac{\partial t}{\partial r} + \frac{1}{r^2}\frac{\partial^2 t}{\partial \varphi^2} + \frac{\partial^2 t}{\partial z^2}\right) + \frac{q_v}{c_p \rho}. \quad (2)$$

Temperature in the cylinder axis can be written as

$$t(r,\tau) = t_0 + \frac{q_l}{4\pi\lambda}\int_0^{\tau} \frac{e^{\frac{-r^2}{4a\tau}}}{t} dt = t_0 + \frac{q_l}{4\pi\lambda} W(u), \quad (3)$$

where the indefinite integral can be expressed in the form of infinite series by means of a substitution

$$u = \frac{r^2}{4a\tau} \quad (4)$$

as

$$W(u) = -\gamma - \ln u + u - \frac{u^2}{2.2!} + \frac{u^3}{3.3!} + \frac{u^4}{4.4!} + \ldots, \quad (5)$$

where

γ is Euler-Mascheroni constant (0.5772).

The numerical model was set up on the basis of experimentally determined input thermokinetic parameters of the rock and boundary conditions with an objective to create the situation similar to real conditions. The objective of heat transfer simulation in the observed borehole was to determine the temperature field and heat flows in the rock in dependence on the borehole depth. The numerical model was set up in the program ANSYS Workbench – Fluent [4]. This CFD software serves the simulation of thermophysical and physical phenomena in a wide range of software simulations. Mathematical modeling of concrete physical phenomena is enabled through fundamental physical models and equations.

The course of temperature in the calculated temperature field near the borehole surface, mainly in the area of the probe output shows the drop of the temperature of medium at the output from the initial 4.8 °C to 1.8 °C after 22 days of heat collection simulation. The obtained heat output decreased with the increasing number of days Fig. 2. Its decrease depends on more parameters, but mostly on thermal conductivity and specific thermal capacity of the rock that are given as initial conditions. Numerical simulations showed that relevant data about thermokinetic parameters of the rock are needed for the exact simulation of heat collection from the rock in the vicinity of the deep borehole Fig. 3.

Numerical simulation illustrates very well changes of thermal fields in the rock massif, mainly temperature changes in dependence on the borehole depth and time at heat collection. Temperature changes in the borehole were decisive for an analysis of a possible change in the behavior of heat pipe working substance at heat collection and subsequent decrease of heat potential of the lower part of the borehole.

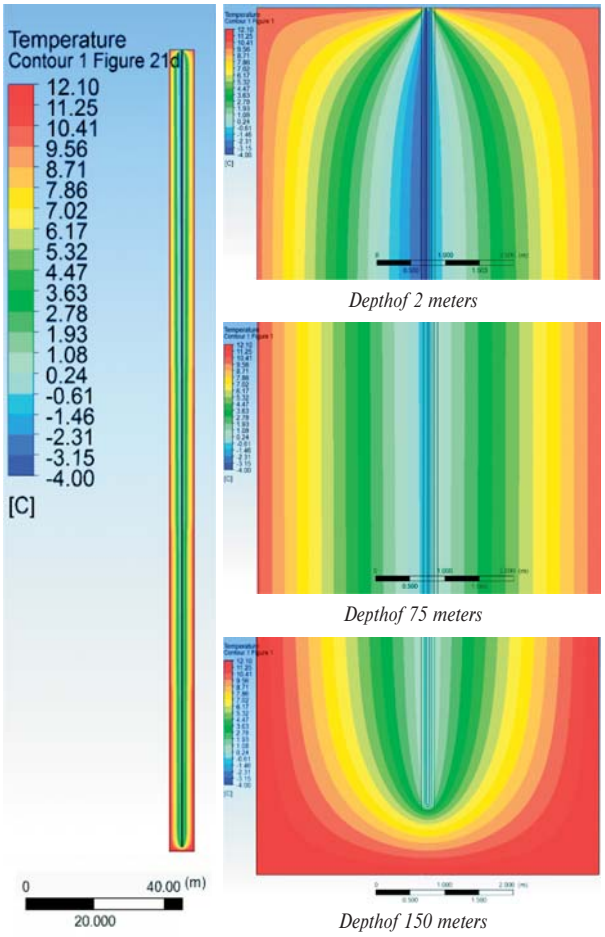

Fig. 2 Temperature field in the vicinity of the borehole after 21st day of heat collection

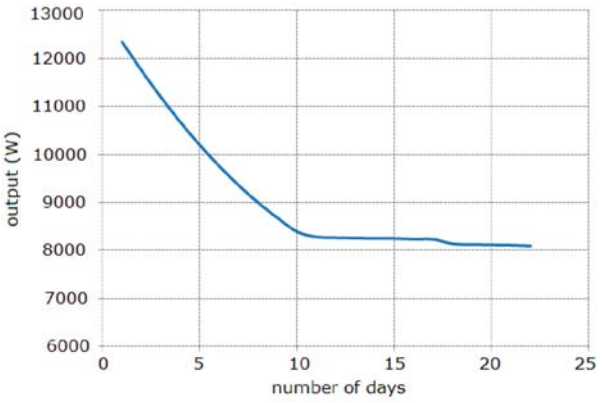

Fig. 3 Course of output obtained from borehole simulation

4. Measurement of heat pipes output parameters

The measurement was made after seven days when the temperatures in the borehole had been leveled off. The reason was to eliminate the influence of supplied ammonia on temperature changes in the deep borehole when the heat pipe was applied. During these seven days the heat pump was off and, consequently, the heat transfer from the borehole was stopped.

Due to the fact that the measurement was made in spring months which were extraordinarily warm, the secondary circuit of the heat pump had to be connected to the cooling tower to provide efficient heat removal on the secondary side of the heat pump. The continuous operation of the heat pump started when a stable appliance was connected to the heating (secondary) circuit.

Before the measurement 700 g of gaseous ammonia was removed from the heat pipe to avoid residual ballast gas and impurities in the upper condensation part of the heat pipe. During ammonia inlet, the heat pump operated at full output. When the heat pump was launched and ammonia removed, the process of phase change in the heat pipes immediately began. Immediate drop of temperatures in the heat pipe along the all depth of the borehole was recorded. The temperature decrease was recorded also in the next hours and also in the following day. During the heat pump operation the temperatures were decreasing nonlinearly mainly in the upper part of the heat pipe in the vicinity of the condensation heat exchanger. In these parts the temperature drop was the most intensive. The temperature in the depth of 5 meter dropped to the lowest minimum during the measurements, namely to 3 °C. Considerable temperature drop was recorded up to the depth of 100 m. The lowest temperature drop was recorded at the depth of 150 meters Fig. 4.

The efficiency of heat pipe was manifested on the temperature gradient of the heat pump primary circuit. At the start of measurement its difference was as many as 3.5 °C. Gradually, the temperature difference was mildly decreasing and at the end of measurement achieved 2.3 °C, which was seen also in gradual decrease of heat output obtained from the borehole by means of the heat pipe Fig. 5.

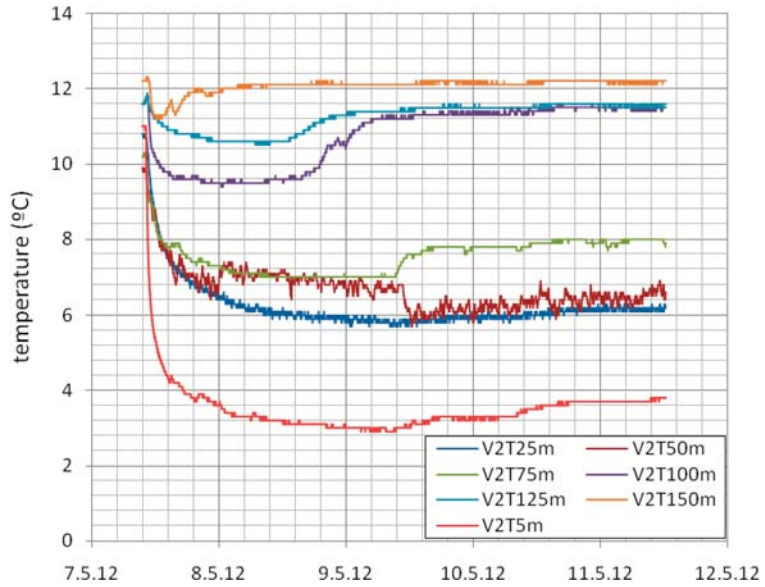

Fig. 4 Course of temperature changes in the borehole depths during heat pipe measurement.

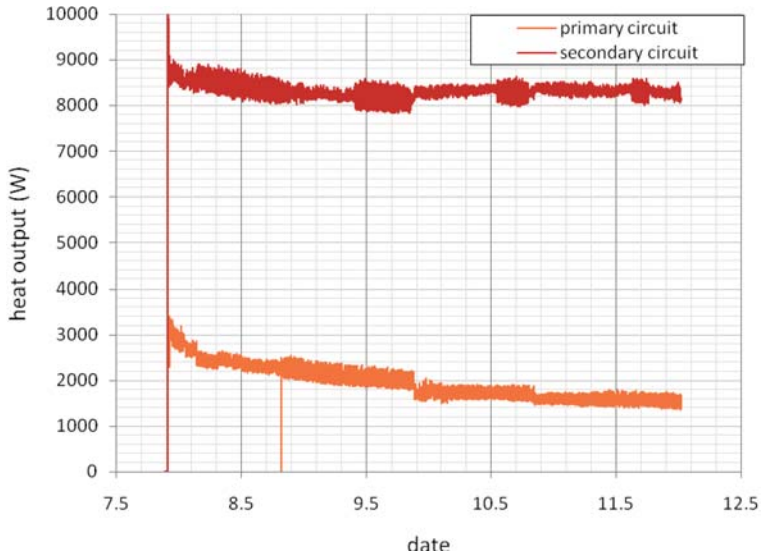

Fig. 5 Course of output change on the heat pump primary circuit

Resultant heat output measured on the heat pump primary circuit — Table1

Max. output*	3200 W
Min. output*	1550 W
Average output*	1900 W
Average overpressure in HP	3.42 Bar

* – heat output obtained from the soil during measurement take on the primary side of heat pump

The difference between the output obtained by a classical method of a forced circulation of the working substance and the one obtained by the heat pipe was considerableTable1. It is obvious that the heat pipe did not continuously work with the designed heat transfer [5]. This fact can be attributed to more factors having influence on the correct operation of the heat pipe. One problem was removed at the introductory measurement of the heat pipe and the output considerably increased and the heat pipe began working.

5. Conclusion

During the measurements taken one the heat pipe, more changes occurred and were manifested in the records of temperatures and output. One of them was a mild decrease of obtained output during all the measurements on the heat pipe. After a few days of measurements gradual leveling off the temperatures to the original value in greater depths was also recorded. There can be several causes of these facts:

- the heat pump was connected to the hot-air unit in the corridors of the building where was a surplus heat rejection. As the outer daily temperatures approached 28 °C, the heat pump control more often turned on and off in short time intervals. This could result in continuous interruption of the process of phase change in the heat pipe which led to heat output drop. This problem was solved through stationary cooling but the output increase was not significant.
- Another possibility which might occur in our case may be unequal dosing of the working substance for individual U tubes of the heat pipe. As the heat pipe consists of two independent U-tubes, the condensate dosing in the exchanger part can notbe influenced and it is impossible to provide and equal supply of the working substance into each of the U-tubes. This fact can cause that the condensate from the exchanger part leading to the lower part of the heat pipes flows to one U-tube only. It can result into the heat pipe output drop due to:
  - loss of efficiency of one of the U-tubes (as it is empty there is no phase change in it),
  - increases of pressure caused by the height of ammonia column in the full U-tube (it could, in the case of complete accumulation in one of the U-tubes, achieve the height of 60 m). Hydrostatic pressure will increase and the total pressure in theheatpipewillincreaseaswell. Ifthiscaseoccurred, the liquid ammonia boiling would be limited by the depth in which the pressure would not exceed the boiling point at the given temperature.

References

[1] KAPJOR, A., HUZVAR, J., PILAT, P.: *Effect of Operating Conditionsto a Temperaturein the Heat Pump Compressor (in Slovak),* Erin 2011, 5th annual intern. travelling conference for young researchers and PhD students, Vysoké Tatry, 2011.

[2] LENHARD, R., JANDACKA, J., JAKUBSKY, M.: *Devices for Simulating Low-potential Transformation of Geothermal Heat to Hheat Suitable for Heating (in Slovak),* Zilina 2010.

[3] PAPUCIK, S., VANTUCH, M., JANDACKA, J.: *Operating Measurement of Heat Pumps Air/Water (in Slovak),* Vetranie a klimatizacia 2011: Systemy vetrania a klimatizacie v budovach s nizkou spotrebou energie, Tatranska Lomnica, 2011.

[4] LENHARD, R.: *Numerical Simulation Device for the Transport of Geothermal Heat with Forced Circulation of Media,* Fourth Global Conference on PCO 2010, Kuching – Sarawak – Malaysia 2010.

[5] CAJA, A., NEMEC, P., MALCHO, M.: *The Dependence of Quantum and Filling Type to Heat Transport of Gravity Heat Pipe,* Experimental fluid mechanics 2010, Liberec 2010.

Martin Luxa – Jaroslav Synac – Pavel Safarik – David Simurda *

CAUSES AND SOLUTION OF APERIODICITY OF SUPERSONIC FLOW FIELD DOWNSTREAM OF A PROFILE CASCADE

The paper deals with problems of transonic flow field periodicity downstream of a profile cascade with finite number of blades. The origin of phenomena generating this aperiodicity in transonic wind tunnel is described. The solution of this problem by means of adjustable perforated tailboard is documented by results of optical measurements (interferometry, schlieren methods) on a turbine profile cascade consisting of six blades only. The conditions of formation of limit load regime are described.

Keywords: *Turbine cascade, exit flow periodicity, transonic flow, porous tailboard, limit load*

1. Introduction

One of the most important conditions for correctness and credibility of the results of blade cascade testing in wind tunnels is the inlet and the exit flow field periodicity. The periodicity of exit flow field is closely bound to number of profiles in the cascade. The optimal case is cascade with infinite number of blades (unfortunately impossible in aerodynamic experimental research). The lowest possible number of blades in a cascade ensuring the correct flow field parameters at least in the middle three channels of the finite profile cascade is recommended in ([1], [2]). However, these recommendations do not seem useful in the case of supersonic exit velocities because the exit flow field is affected by structures that come of free jet boundary behind the lateral profiles of the measured cascade. Aperiodic distributions of exit static and total pressure and exit flow angle along the cascade pitches as well as an increase of entropy are consequences of formation of the free jet boundary downstream the trailing edges at supersonic regimes of cascade operation. To prevent the origin of free jet boundary downstream of one of the lateral profiles, a perforated tailboard was used. A turbine profile cascade, which consists of six blades only, was used for checking of the effects of the perforated tailboard. The results of measurements with and without the perforated tailboard are compared.

2. Free jet boundary and cascade exit supersonic flow field

The exit part of flow field is affected by structures, which originate at free jet boundaries downstream of both outer blades of the measured cascade. It depends on the type of cascade, the shape of used profile, the stagger angle, the back pressure etc., whether the exit part of supersonic flow field in the cascade will be affected by flow structures that come either from free jet boundary behind the first or the last cascade profile, alternatively from both of them. The free jet boundaries arise on trailing edges of lateral profiles (see Fig. 1). The fan of expansion waves coming from trailing edge is followed by compression waves (due to the curvature of free jet boundary line), which are then again followed by a fan of expansion waves, etc. The process of alternating expansion and compression downstream the profile cascade is similar to the pseudo shock wave phenomenon [3]. Expansion and compression waves influence the exit flow field in different ways.

The expansion waves influence the flow field in the vicinity of the trailing edge. Flow on the surface exposed to the expansion waves is more accelerated and pressure conditions on the pressure and suction surface, which determine formation of near wake, are altered. Hence the base pressure behind each profile differs from blade to blade according to the angle of corresponding expansion wave. These pressure changes result in significant differences of flow structures in exit part of all affected interblade channels. At higher outlet velocities the aperiodic phenomena might promote earlier onset of the limit load regime. The limit load regime [4] is the fourth significant regime at operation of high – speed turbine blade cascades [5]. This regime determines conditions at which farther decrease of backpressure cannot affect flow development in the exit part of the profile cascade. The internal branch of exit shock waves either impinges on the trailing edge of the next profile or misses it completely. The supersonic exit flow deviation $\Delta\alpha_{ps}$ increases. The condition of limit load can be determined according to the relation:

$$|M_2 \sin \beta_2| \geq 1 \qquad (1)$$

* **Martin Luxa[1], Jaroslav Synac[2], Pavel Safarik[3], David Simurda[1]**
[1] Institute of Thermomechanics ASCR, v.v.i., Prague, Czech Republic, E-mail: luxa@it.cas.cz
[2] R&D dept., Skoda Power, Pilsen, Czech Republic
[3] Czech Technical University in Prague, Prague, Czech Republic

where M_2 is the exit Mach number and β_2 is the exit flow angle (oriented to the rotor peripheral direction).

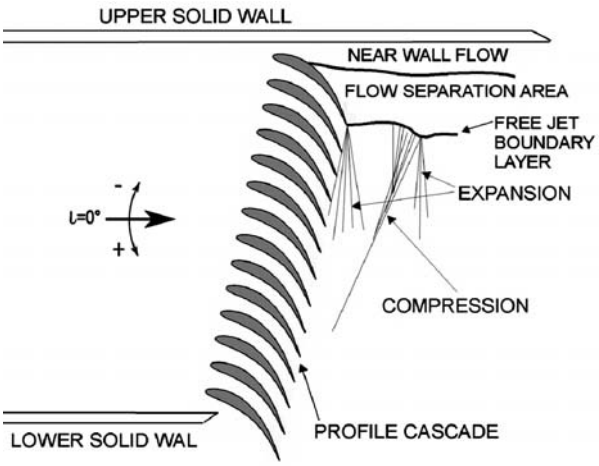

Fig. 1 Origin of aperiodic phenomena in the blade cascade exit flow field

The undesirable limit load regime, which is not caused by sufficiently small backpressure, can be reached in one or even in more interblade channels. The position of limit loaded channel (or channels) can be changed along the cascade according to the pressure condition downstream the cascade. The backpressure affects the formation of the free boundary layer and thus the mutual position of expansion and compression waves relative to the cascade. Figure 2 shows an example of exit flow field downstream a profile cascade affected by expansion waves in upper inter blade channels (here the limit load regime is seemingly reached); the flow field structures in exit parts of lower inter blade channels correspond to the real back pressure.

The compression waves combine together and form a shock wave. This undesirable shock wave can brake into the interblade channel and completely disturb the flow structures in the exit part of the channel. The interaction of these shock waves and the regular system of exit shock waves downstream the profile cascade is also inevitable. These phenomena, taking place due to formation and development of the free jet boundary behind a blade cascade with finite number of blades at supersonic regimes of cascade operation, result in aperiodic distributions of exit velocity and exit flow angle along the cascade pitches and increase of entropy.

Figures 3 and 4 show schlieren pictures taken at identical angle of incidence ι but different back pressure. These figures document how the exit flow field may or may not be influenced by previously described phenomena. Due to lower back pressure and hence different exit flow deflection, the free jet boundary and the position of additional shock waves shifts and at lower backpressures may not influence the cascade exit flow field in the region of measurements at all (Fig. 4).

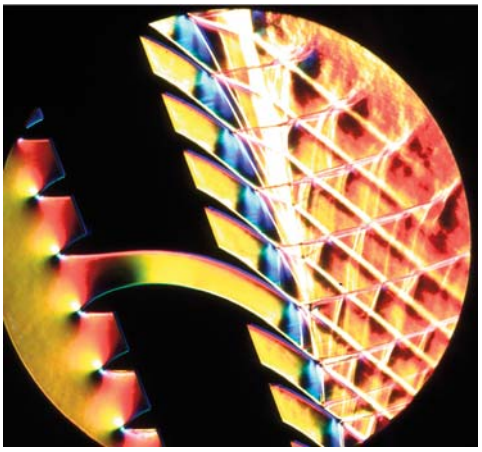

Fig. 2 The colour schlieren picture of the flow field in a profile cascade, $\iota = -30°$, $M_{2is} = 1.2$. The limit load condition is actually reached when $M_{2is} \sim 1.5$

Fig. 3 The schlieren picture of the flow field in a profile cascade, $\iota = 0°$, $M_{2is} = 1.402$. Additional shock waves appear in the exit flow field which is therefore disturbed and aperiodic

3. Technique of ensuring periodicity of the supersonic flow field behind a blade cascade

Various systems of perforated walls, solid, slotted or perforated tailboards, throttles etc. have been used in high speed experimental aerodynamic research to prevent the free jet boundary formation, e.g. [6]. In this study, configuration with only one perforated tailboard was used in the wind tunnel for 2D cascade testing. The perforated tailboard was mounted next to one of the lateral profiles (the suction side of this profile is outer suction side of the whole cascade), see Fig. 5. This way of tailboard design should prevent the origin of the free jet boundary and at the same time prevent the reflection of the system of exit shock waves back to the exit flow field.

Fig. 4 The schlieren picture of the flow field in a profile cascade, ι = 0°, M_{2is} = 1.828. No additional shock waves visible, perfect flow field periodicity in exit part of interblade channels

The holes – solid wall ratio R (or the open area ratio R) of the used perforated tailboard was chosen $R = 0.5$. The value of this ratio was obtained from linearized theory of wave cancellation in perforated wind tunnels (the entropy changes are neglected and the compressibility equations are linearized) [7]. This ratio is independent of Mach number and shock intensity for the "non-reflection" case. If the area ratio R of perforated walls is not selected correctly (i.e. $R = 0.5$) a partial reflection of an impinging shockwave will occur. The pressure rise Δp_r due to partial reflection of the primary shock wave can be determined from the relationship:

$$\frac{\Delta p_r}{\Delta p_{sh}} = 1 - 2R\,, \tag{2}$$

where Δp_{sh} is the pressure rise in the primary shock wave.

The value of angle between perforated tailboard and the plane of trailing edges α'_{ps} was set according to the simple "empirical cosine rule", used for predicting of fluid outlet angle in design of turbo machines [8]. According to this rule, the value of exit flow angle β_2 is

$$\beta_2 = \arccos\frac{\Theta + 2r_2}{t}\,, \tag{3}$$

and thus

$$\alpha'_{ps} = \frac{\pi}{2} - \beta_2 - \Delta\alpha_{ps} \tag{4}$$

where $\Delta\alpha_{ps}$ is the tailboard angle correction for the exit velocities close to limit load regime and higher, r_2 is the trailing edge radius, t is the pitch and Θ denotes the opening at the throat of the cascade.

Significantly complicated is the determination of proper value of tailboard angle α'_{ps} in the case of exit flow conditions close to the limit load regime. It is necessary take into account the additional exit flow angle deviation or alternatively the supersonic flow deviation in the formula (4). The support of computational fluid dynamics methods (CFD) shows to be very effective and helpful in this situation.

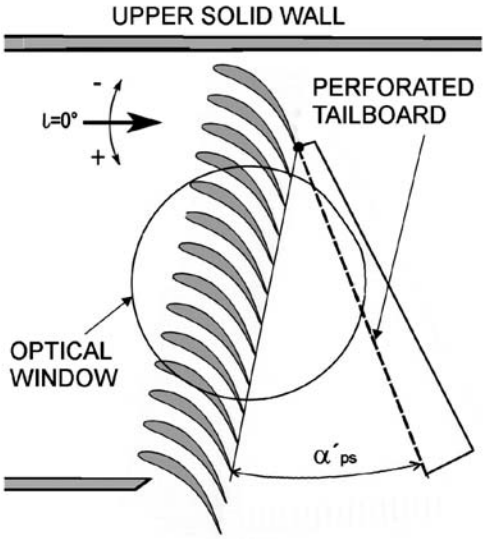

Fig. 5 An example of test section with installed tailboard

4. Procedure and results

The measured blade cascade represents a middle section of a long turbine rotor blade. The model blade cascade consists of six prismatic profiles only. The exit flow field and its periodicity were strongly affected in this case by structures which originate on the free jet boundary next to the suction side of the upper lateral profile [9].

The perforated tailboard was attached next to the trailing edge of the upper lateral profile (similarly to the situation in Fig. 5). The optimal value of angle between the tailboard and the plane of trailing edges (α'_{ps}) was checked by colour schlieren technique in wide range of incidence angles, exit Mach numbers, angles α'_{ps}, etc. No tailboard angle correction $\Delta\alpha_{ps}$ was necessary for exit velocities considerably smaller than those corresponding to the limit load regime. It was found out that the optimal value of the angle α'_{ps} corresponds to the rule (3). An example of flow field with $\Delta\alpha_{ps} = 0°$ and $\Delta\alpha_{ps} = -3°$, respectively, is shown in Fig. 6.

The optical methods were applied (interferometry, colour schlieren method and schlieren method in Toepler configuration) and results were compared with results of measurements without the tailboard. The experiments were carried out for isoentropic exit Mach numbers and incidence angles in the range.

The interferograms in Fig. 7 show different structures in the exit part of flow field in the case without tailboard (left) and with it (right).

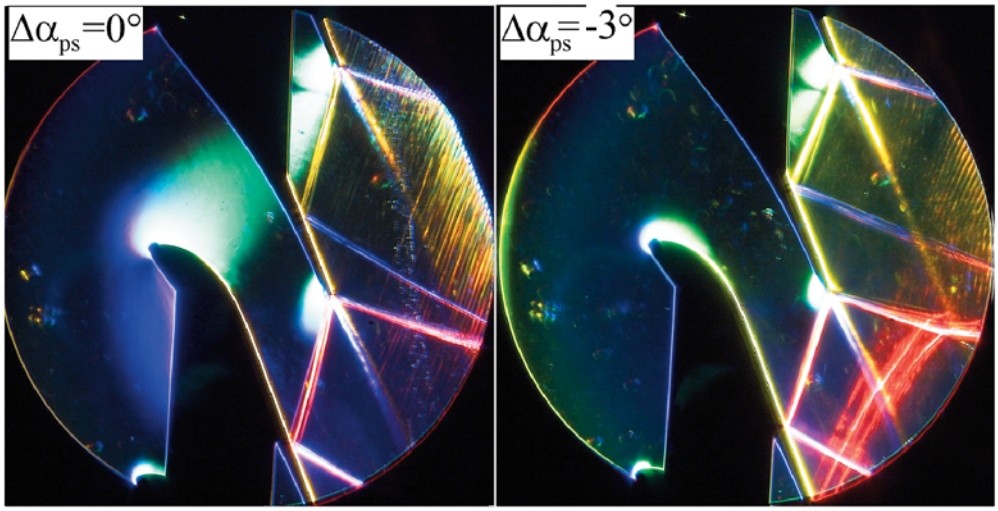

Fig. 6 The colour schlieren pictures taken for two different angles of perforated tailboard α'_{ps}, isoentropic exit Mach number $M_{2is} = 1.5$, incidence angle $\iota = +30°$

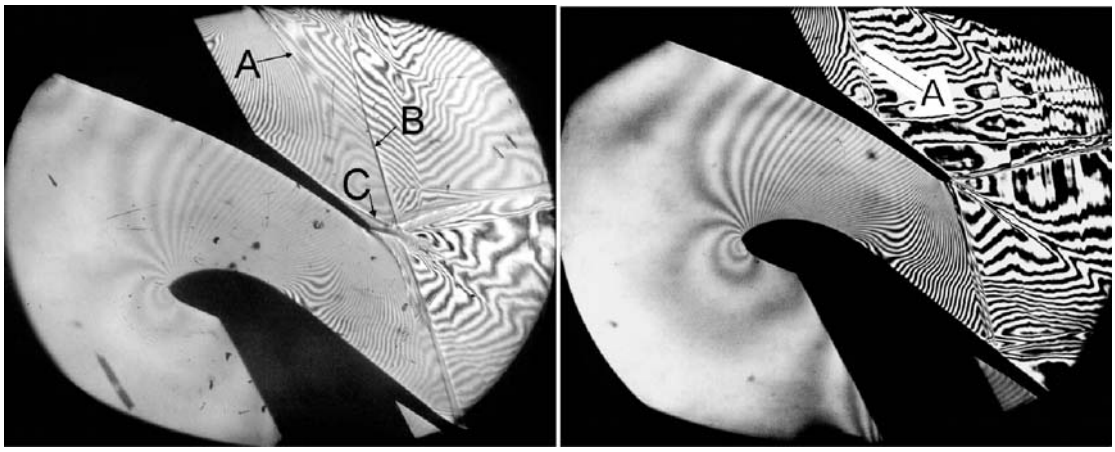

Fig. 7 Interferograms; isoentropic exit Mach number $M_{2is} = 1.5$, incidence angle $\iota = 0°$; flow field affected by structures formed on the free jet boundary (left); different, periodic exit flow field in the arrangement with perforated tailboard (right)

The left interferogram shows that the regular periodic flow structures are completely disturbed as a consequence of expansion waves and shock waves originating on the free jet boundary. Due to expansion waves influencing flow on the suction side before the leading edge, the exit flow is significantly deflected. This can be seen on the interferograms as an increased obliqueness of exit shock waves internal branch of which (A) completely misses suction side of the neighbouring blade. This deflection is so intense that the near wake is formed before trailing edge on the suction side (B). The additional shock wave (C) goes through the wake downstream the upper profile and have also influence on the flow structures in the middle inter blade channel. The situation is completely different in the right part of Fig. 7. The exit part of the flow field is substantially more periodic, both visible internal branches of exit shock waves are parallel. Only small disturbances, caused by the perforated tailboard, appear on the right side of the interferogram near the tailboard.

The isoentropic Mach number M_{is} distributions on the profile suction side at incidence angle $\iota = +30°$ and different exit isoentropic Mach numbers M_{2is} are shown in Fig. 8. The effect of the structures coming from the free jet boundary is evident in the upper diagram.

5. Conclusions

Phenomena originating on the free jet boundaries behind the lateral profiles of a blade cascade operating at transonic regimes pose a problem since these phenomena significantly influence flow

field at the exit of the blade cascade and farther downstream. Thus the qualitatively and quantitatively altered flow field largely differs from the case of periodic flow field and exhibits increased level of produced entropy. Therefore, periodicity of the flow field at the exit of blade cascades must be ensured. The solution of problem with periodicity of the supersonic flow field downstream of a profile cascade lies namely in the necessity to prevent the origin and development of the free jet boundary downstream the cascade. To achieve this, adjustable perforated tailboard was used in this research. The analysis of optical measurements proves noticeable differences in the flow field structures in exit parts of inter blade channels and downstream. The results of optical measurements with the tailboard confirm substantial exit flow field periodicity improvement. Nevertheless, successful application of the tailboard depends on correct choice of the perforation ratio and proper adjustment of the tailboard angle corresponding to the exit flow angle behind an infinite blade cascade. The shortcoming of using the perforated tailboard is origin of small disturbances caused by the tailboard perforation. These disturbances probably cause an increase in level of turbulence in the vicinity of the tailboard. However, intensity of these disturbances and its influence on the flow field in the described experiments are yet to be investigated.

Acknowledgement

The research was supported by the Czech Science Foundation under the grant No.GAP101/10/1329.

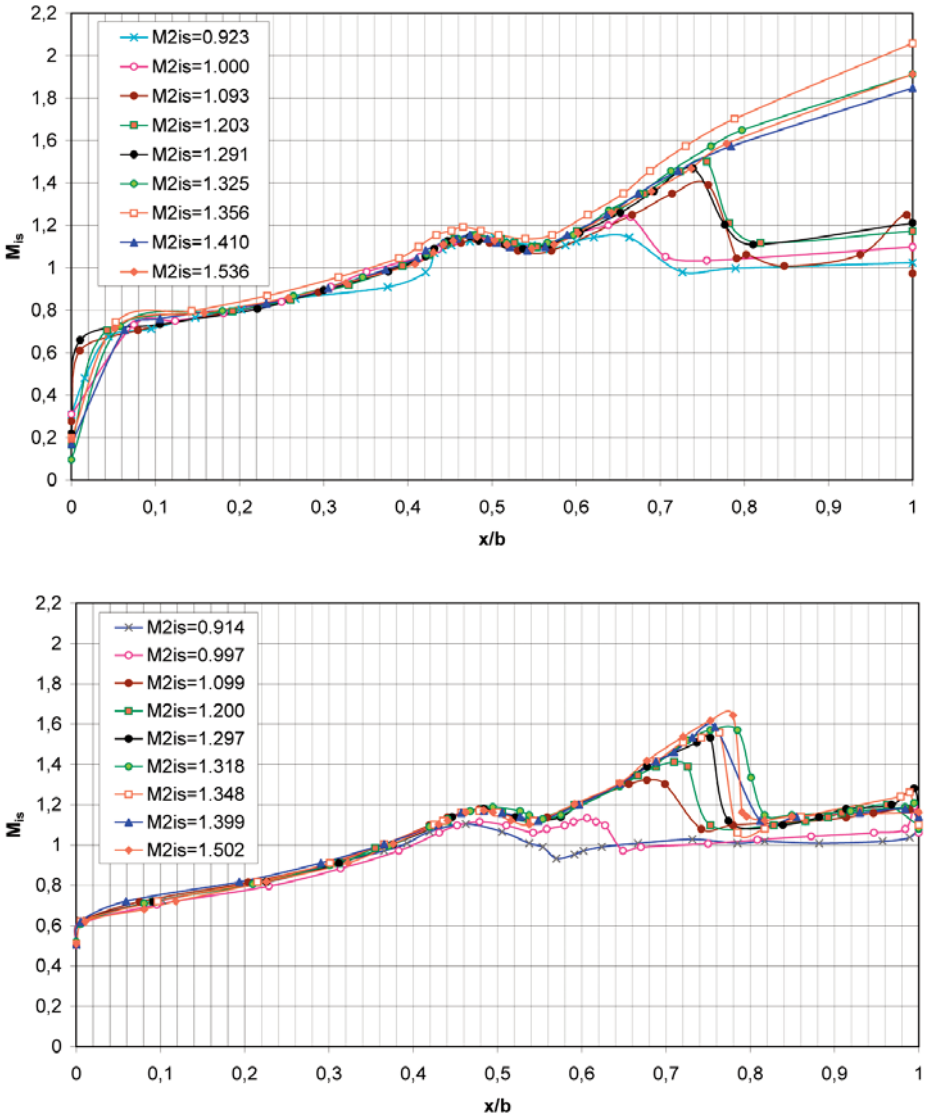

Fig. 8 Isoentropic Mach number distribution on the suction side on the profile. Isoentropic exit Mach number 0.914 ≤ M_{2is} ≤ 1.536, incidence angle ι = +30°; upper diagram: Mach number distribution affected by structures formed on the free jet boundary; lower diagram: Mach number distribution in the arrangement with perforated tailboard

References

[1] GUKASOVA, E. A.: *Aerodynamiceskoje soversenstvovanije lopatocnych apparatov i gazovych turbin* [Aerodynamic Design of Turbomachines]. Moskva, 1960

[2] STRAKA, P.: *Numericka simulace pri podpore experimentalniho vysokorychlostniho aerodynamickeho vyzkumu proudeni v primych lopatkovych mrizich* [Numerical Simulation as a Support of Experimental High-speed Aerodynamic Research in Straight Blade Cascades]. Ph.D. Thesis, Prague, 2010

[3] CROCCO, L.: One Dimensional Treatment of Steady Gas Dynamics. In: *Fundamental of Gas Dynamics,* ed. H.W. Emmons, High Speed Aerodymanics and Jet Propulsion, vol. III., Princeton U.P., 1958

[4] LUXA, M., SIMURDA, D.: Opticka mereni na mrizi TR-P-2 [Optical Measurements on Cascade TR-P-2]. *Research report IT CAS* v.v.i., No. 1472/11. Prague, 2011

[5] SAFARIK, P., LUXA, M., PICMAUSOVA, H., SIMURDA, D.: *On Measurement and Evaluation of Flow Conditions at Limit Load of Turbine Blade Cascade*. XXI Biannual Symposium on Measuring Techniques in Turbomachinery, Valencia, 2012.

[6] STARKEN, H.: A New Technique for Controlling the Exit Flow Periodicity of the Supersonic Cascades. *Measuring Techniques in Transonic and Supersonic Cascades and Turbomachines,* ed. A. Bolcs and T. Fransson, Zurich, 1977

[7] GOETHERT, B. H.: *Transonic Wind Tunnel Testing.* Oxford, 1961

[8] DIXON, S. L.: *Fluid Mechanics and Thermodynamics of Turbomachinery,* Amsterdam, 1998

[9] LUXA, M., SIMURDA, D.: Opticka mereni na transsonicke mrizi [Optical Measurements on Transonic Cascade]. *Research report IT CAS* v.v.i., No. 1476/11. Prague, 2011

Jan Rajzinger *

CALCULATION OF MAXIMUM WATER CONTENT IN VARIOUS NATURAL GASES BY USING MODIFIED PENG-ROBINSON EQUATION OF STATE

During the expansion of natural gas in the pipeline, the gas cools down due to the Joule-Thomson effect and due to the interaction between pipeline system and its surroundings to the conditions at which gas is saturated by water vapors, and gas is not able to keep excess humidity and its condensation and hydrate formation will occur. For that reason it is necessary to identify the critical parts of the pipeline systems, maximum water content in the gas, to choose appropriate physical model, and apply appropriate solutions which also will considerably influence energy consumption requirements. For the physical model development, method based on equality of fugacity concept with modified Peng-Robinson equation of state and Rachford-Rice appropriate solution algorithm are used to develop the model estimating the water content in equilibrium with natural gas. The results of the presented method are compared with selected experimental data from the literature.

Keywords: *Natural gas, water content, phase equilibrium, gas hydrate, equation of state*

Nomenclature:

f	fugacity, Pa
$k_{ij}(T)$	temperature dependent binary interaction parameter of PR EoS
$k_{ij,0}$	binary interaction parameter of PR EoS
$k_{ij,1}$	binary interaction parameter of PR EoS
p	pressure, Pa
T	temperature, K
x	set of liquid phase mole fractions
y	set of vapor phase mole fractions
$\alpha(T_r)$	dimensionless temperature dependent function of PR EoS
ϕ	fugacity coefficient
L	superscript denot as liquid
V	superscript denot as vapor
sat	superscript, saturated vapor
cal	subscript, calculated property
exp	subscript, experimental property
i,j	subscript, molecular species
id	subscript, ideal gas
initial	subscript, initial estimate for calculation
r	subscript, reduced parameter (temperature, pressure)
w	subscript denotes water

1. Introduction

The pressure of natural gas (NG) for final consumptions declines during the transmission and distribution to the values that are utilized in medium and low pressure distribution systems. NG contains certain amount of water that is expressed by water dew point temperature replenished with respective pressure. During the expansion of NG in the pipeline, the gas cools down due to the Joule-Thomson effect and due to the interaction between pipeline (and pipeline system equipments) and its surroundings (heat transfer processes) to the conditions at which different phase formation as water liquid, condensates and other solid materials (hydrates) might occur [1]. NG hydrates are crystalline solids composed of the water and the gas. The gas molecules (guest) are trapped in water cavities (host) that are composed of hydrogen-bonded water molecules [2]. Typical NG hydrate molecules include methane, ethane, propane, and carbon dioxide. Both hydrates and liquid slugs are damaging the gas pipeline system operation by corrosion, erosion, clogging and the mechanical stress to the system [3].

To avoid these problems, expensive dehydratation units, heating units, inhibitors units, etc., have been installed by natural gas companies. The design and cost of these installations depend on the exact knowledge of the water content at the dew point (contractually established). Though given water dew point is contracted, during NG transmission and distribution can be worsened mainly by new or mended pipelines. For that reason it is necessary to continue in developing new models for better identification of the critical points (water liquid or hydrate formation) in the gas pipeline systems.

Experience from industry have exposed that the maximum level of water content in vapor phase is bigger at higher pressures than the value that comes from the ideal gas model vapor-liquid equilib-

* **Jan Rajzinger**
Department of Thermal Power Engineering, Bratislava, Slovakia, Faculty of Mechanical Engineering, Slovak University of Technology in Bratislava, E-mail: jan.rajzinger@stuba.sk

rium calculation. In order to solve the problem and to approach the real behavior of water-gas system it is necessary to use more complicated calculation that has to be numerically counted. Peng-Robinson equation of state (PR EoS) is by far the most popular cubic EoS that is used in the gas and oil industry nowadays. This equation is used to calculate the properties of pure compounds and, more importantly, binary and multicomponent mixtures including both low and high pressure vapor-liquid equilibrium [4], [5]. Calculation of water content is complicated due to non-ideal behavior of water and NG. For that reason, it is impossible to simulate interaction correctly with the normally used PR EoS. Therefore the modified PR EoS is used to calculate species fugacities in both phases (liquid and vapor), of course with the composition and compressibility appropriate to each phase.

This article presents the method for NG maximum water content calculations based on equality of fugacity concept with following presented methods which are also compared with selected experimental data from the literature:

- Ideal gas model with ANSI S1.26-1995 equation (The American National Standard Institute) for water saturated pressure calculations.
- Standard PR EoS without modifications.
- Modified PR EoS using 'Chapoy' modification.
- Modified PR EoS using GERG water model published as part of the ISO 18453, proposed by the European Gas Research Group GERG (Group Européen de Recherche Gazière).

Selected natural gases from practice, 100% methane and called “Russian NG”, “Norwegian NG-type H” and “Norwegian NG-type L” are compared from maximum water content point of view at different pressures and temperatures ranges.

2. Methods and models

Gibbs theory showed that at thermodynamics equilibrium the pressure, temperature and fugacity (or chemical potential) of each component are the same for each coexisting phase. The starting point for vapor-liquid equilibrium is the equality of fugacities of each species in each phase, that is:

$$f_i^V(T, p, y) = f_i^L(T, p, x) \quad \text{(Pa)} \tag{1}$$

Equation (1) represents the starting point for any phase equilibrium calculation. However, the basic problem in this equation is to relate these fugacities to mixture composition. The fugacity of a component in a mixture depends on the temperature, pressure and composition of that mixture. Therefore to relate fugacities to temperature, pressure, and mole fraction, it is very useful to introduce the vapor and liquid-phase fugacity coefficient [6]:

$$\phi_i^V(T,p,y) = \frac{f_i^V(T,p,y)}{y_i p} = \frac{f_i^L(T,p,x)}{x_i p} = \phi_i^L(T,p,x) \text{ (-)} \tag{2}$$

Phase equilibrium calculations with equation of state are iterative and in this case the isothermal flash calculation is used [6]. The flash method is the type of calculation where the objective is to calculate the amount of phases present in an equilibrium mixture and to determine the composition of the coexisting phases. The temperature, pressure, and initial compositions are the input parameters. The objective function is solved by using Rachford-Rice algorithm. Then it uses the Newton-Rapson method for the correction steps.

2.1. Ideal gas model for vapor-liquid equilibrium calculation

The following simplifications are used for ideal gas model in terms of vapor-liquid equilibrium calculations:

- It is assumed that gases are not very well soluble in water, so solubility of gases in water is negligible and then liquid phase contains only clean liquid water.
- The gas impact on fugacity in liquid phase is neglecting.
- The total pressure is not very different from water saturated vapor pressure.

When the following simplifications are applied into Equation (1), the simple equation for calculation of maximum water content $y_{w,id}$ in vapor phase is in the form:

$$y_{w,id} = \frac{p_w^{sat}}{p} \text{ (-)} \tag{3}$$

For water saturated pressure calculations is used ANSI S1.26-1995 equation attributed to the World Meteorological Association [7]:

$$\begin{aligned}\log_{10}(p^{sat}) &= 10.79586\left[1-\left(\frac{273.16}{T}\right)\right] - \\ &- 5.02808\log_{10}\left(\frac{T}{273.16}\right) + \\ &+ 1.50474\times10^{-4}\left\{1-10^{-8.29692\left[\left(\frac{T}{273.16}\right)-1\right]}\right\} + \\ &+ 4.2873\times10^{-4}\left\{-1+10^{4.76955\left[1-\left(\frac{T}{273.16}\right)\right]}\right\} - \\ &- 2.2195983\end{aligned} \quad \text{(atm)} \tag{4}$$

This equation is said to have an uncertainty of 0.04 % for temperature range $233 < T < 273$ K and of 0.06% for $T > 273$ K.

2.2. Peng-Robinson equation of state

The PR EoS provides a mathematical relation between the temperature, pressure, and molar volume V of a pure fluid [6]. Various improvements of this equation are available in literature [8], [9], [10].

To have an accurate representation of vapor pressures of pure compounds a new energy term $\alpha(T_r)$ is proposed for modified PR EoS ('Chapoy' model) [11]:

$$\alpha(T_r) = \exp\left[c_1\left(1-\sqrt{T_r}\right)\right]\times \\ \times\left[1 + c_2\left(1-\sqrt{T_r}\right)^2 + c_3\left(1-\sqrt{T_r}\right)^3\right]^2 \quad (-) \qquad (5)$$

where c_1, c_2, and c_3 are new three adjustable parameters correlated as a functions of the acentric factor:

$$c_1 = 1.3569\omega^2 + 0.9957\omega + 0.4077 \quad (-) \qquad (6)$$

$$c_2 = 11.2986\omega^2 + 3.5590\omega + 0.1146 \quad (-) \qquad (7)$$

$$c_3 = 11.7802\omega^2 + 3.8901\omega + 0.5033 \quad (-) \qquad (8)$$

Detailed applications ranges and limitations of this modified PR EoS are published only for prediction of water vapor pressure [11].

Modified Peng-Robinson EoS (GERG-model), in order to ensure an accurate calculation of water vapor pressure above ice and liquid, the following energy term α(Tr) is used for water [9]:

$$\alpha(T_r) = \left[1 + A_1\left(1-\sqrt{T_r}\right) + \right. \\ \left. + A_2\left(1-\sqrt{T_r}\right) + A_3\left(1-\sqrt{T_r}\right)^4\right]^2 \quad (-) \qquad (9)$$

where the new energy term in Equation (29) is by temperature ranges divided into two parts with A_1, A_2 and A_3 coefficients, see [8]. Finally, for the binary systems water/methane, water/ethane, water/carbon dioxide, modified Peng-Robinson EoS (GERG-model) introduces temperature-dependent on the interaction of parameters to obtain a satisfactory description of the vapor-liquid equilibrium, see [9]:

$$k_{ij}(T) = k_{ij,0} + k_{ij,1}\left(\frac{T}{273.15} - 1\right) \quad (-) \qquad (10)$$

The parameters in Equation (30) of the modified PR EoS, based on GERG model, are Tailor-made specifically for the water content calculations in NG where the solid phase is treated as a 'pseudo' liquid phase. The GERG model with PR EoS has a range of application from 0.5 MPa to 10 MPa and from 258 K to 278 K with defined accuracy, and "applicable" working range 0.1 – 30 MPa and 223 – 313 K with unknown accuracy in the extra range. Detailed applications ranges and limitations of this GERG modified PR EoS and binary interaction parameters for other combinations of gases as well as the critical component properties are available in the literature [9], [10].

3. Results

Compositions of selected gas mixtures are showed in Table 1. Comparing the results of calculations from different methods used for determination of maximal water content in the gas of the methane-water system are together with the comparison of experimental values defined in Fig. 1.

Results prove that the maximal water content of methane-water system is always higher in the reality than in the ideal gas model. That means that gas is capable to keep much more water amount in the form of water vapors than it is presented in the results from

Compositions of selected natural gases [1] Table 1

Component name	NG n°1	NG n°2	NG n°3	NG n°4	NG n°5	NG n°6	NG n°7
	Methane	Laboratory synthetic gas	Laboratory synthetic gas	Laboratory synthetic gas	Russian (May 2012)	Norwegian-Type H	Norwegian-Type L
	Composition [mol %.]						
methane	100.0000	94.0000	89.0000	84.4000	96.2450	84.4230	82.6570
ethane	-	4.0000	7.0000	10.0000	1.8310	8.8540	3.4500
propane	-	-	-	4.0000	0.5360	3.1700	0.7460
iso-butane	-	-	-	0.6000	0.0750	0.3420	0.1026
n-butane	-	2.0000	4.0000	1.0000	0.0840	0.6523	0.1598
iso-pentane	-	-	-	-	0.0180	0.0912	0.0318
n-pentane	-	-	-	-	0.0130	0.0870	0.0231
n-hexane	-	-	-	-	0.0200	0.0293	0.0337
n-heptane	-	-	-	-	-	0.0051	0.0150
n-octane	-	-	-	-	-	0.0010	0.0050
hydrogen	-	-	-	-	-	0.0020	-
helium	-	-	-	-	-	0.0031	-
nitrogen	-	-	-	-	0.8690	0.4210	11.6950
carbon dioxide	-	-	-	-	0.3090	1.9190	1.0810

the ideal gas model. The tendency of deviations of calculated figures from the experimental values of maximal water content in the gas is growing with the increasing temperature and pressure. At the pressure 3.34 MPa and temperature 250.95 ≤ T ≤ 288.15 K the ideal gas model gives better results than standard PR EoS, see Fig. 1. The interesting thing is that in case of low temperatures 250.95 ≤ ≤ T ≤ 264.75 K (at pressure 3.44 MPa) and 250.55 ≤ T ≤ 264.15 K (at pressure 6.89 MPa) the deviations of the ideal gas model from experimental values are lower than values coming from the other models, including GERG model PR EoS, see Fig. 1. Very good results for the area of low temperatures are achieved in the ideal gas model thanks to the equation used for the calculation of the saturated water vapor pressure according to ANSI S1.26-1995. The differences among experimental and calculated figures of the ideal gas model are caused mainly by the fact that the model counts with the water itself (based on saturated water vapor pressure) that means with the pure water vapor without any interaction with other gases and also it does not consider the vapor solubility in the liquid phase of water. It is clear that, by using the ideal gas model the identical results of calculation of the maximal water content in the gas would be reached not only for methane-water but for any gas-water system. On the other hand, even the ideal gas model is more conservative – it gives lower maximal water content in the gas than it should be in the reality – it is an efficient tool for the quick engineering calculations.

On the contrary, no knowledge of limits of the ideal gas model and the equation used for the calculation of the saturated water vapor pressure according to ANSI S1.26-1995 can lead to the false analysis of gas pipeline system and useless or excessive usage of technologies such as gas heating, inhibitors dosage, gas dehydration (primary in the field of gas upstream and NG reservoirs), etc.

Despite the small exceptions, the standard PR EoS model is not satisfactory in comparison with the experimental data because in most cases the calculated maximal water content in methane-water system is much higher than the amount that can be kept by the gas in the reality.

In standard PR EoS and 'Chapoy' modification, water is handled by assuming binary interaction parameter k_{ij} of the order of 0.5. This assumption can underestimate the solubility of water in NG and give a completely incorrect picture about vapor-liquid equilibrium as we can see when we compare different PR EoS and its modifications.

Thank to the application of new energy term $\alpha(T_r)$ with new three adjustable parameters correlated as a functions of the acentric factor, 'Chapoy' modification of PR EoS gives much more better results than the standard PR EoS model. In comparison with the experimental data the calculated maximal water content is higher in most cases. As Fig. 1 show, major deviations from experimental values are in the scale of temperatures 250.55 ≤ T ≤ 279.15 K (pressure 6.89 MPa), which are not characteristics for the area of liquid-vapour but for the zone of hydrate formation for which the equation is not proposed.

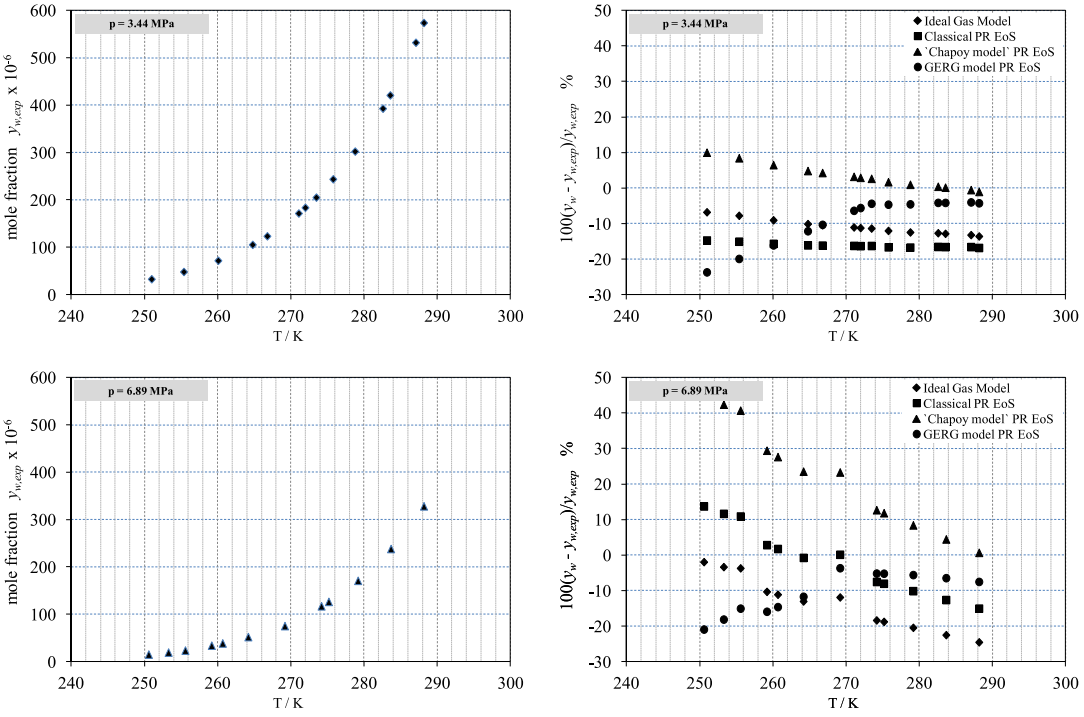

Fig. 1 Experimental water content in the vapor phase of the methane-water and comparison of selected methods with experimental data [12] at pressures 3.44 MPa and 6.89 MPa

The presented modification of PR EoS (GERG model) gives in the comparison with the experimental data the best results from all mentioned models. As Figures show, the exception is in the presented scale of low temperatures $250.95 \leq T \leq 264.75$ K (at pressure 3.44 MPa) and $250.55 \leq T \leq 264.15$ K (at pressure 6.89 MPa), where the better results can be obtained from the ideal gas model with equation used for the calculation of the saturated water vapour pressure according to ANSI S1.26-1995. The highest deviations by using modified PR EoS (GERG model) are in case of zone of hydrate formation, that means the temperature ranges $250.95 \leq \leq T \leq 279.15$ K (pressure 3.44 MPa) and $250.55 \leq T \leq 279.15$ K (pressure 6.89 MPa), see Fig. 1. E.g. at temperature 250.95 K (pressure 3.44 MPa) the deviation from the experimental data is – 23.75 %, on the contrary at temperature 283.15 K the deviation is 0.25 %.

Very high deviations from experimental values are in selected range of temperatures and pressures for all NG, see Fig. 1 and Table 2. The selected ranges of temperatures and pressures are showed due to the application of presented PR EoS (GERG model) for calculation especially for the critical parts of pressure reduction valve (valve seats) and pipelines where the temperatures go below 273.15 K. Deviations from experimental data increase with complesity of NG. Originally, GERG model was proposed for VLE applications but for (ice, hydrate)-vapor equilibria was extrapolated PR EoS by fitting binary interaction coefficient (temperature dependent) of PR EoS to experimental data and by using different function for the energy term $\alpha(T_r)$, [13]. However, as it is evident from Fig. 1 and Table 2, these actions for PR EoS are not sufficient and some improvement should be proposed for another modification of PR EoS or by using three different types of phase equilibria and models to cover the actual temperature and pressure ranges (vapor-liquid, vapor-ice, vapor-hydrate).

Water content calculations in the vapor phase using modified PR EoS (GERG model) for various NG (see Table 1), and pressure range $0.5 \leq p \leq 7.0$ MPa and temperature range $233.15 \leq T \leq 313.15$ K are presented in Fig. 2. The calculated data shows that the maximal water content decreases with the decreasing temperature and rising pressure. As it is clear from presented results, the ability of NG to keep certain amount of water depends on its component. E.g. a calculation shows that Russian NG (NG n°5) is able to keep less humidity than 100% methane. In contrary as Fig. 2 shows, Norwegian NG-type L can contain more water in gas phase by 2.11 %. The maximum water content for water dew point temperature −7 °C and pressure 3.92 MPa varied for analyzed NG, e.g. for 100 % methane is 101.372 ppm (mol), Russian NG have 100.960 ppm (mol), for Norwegian NG-type H and type L is 101.439 ppm (mol) and 102.091 ppm (mol) respectively. But in general, the calculations using modified PR EoS (GERG model) show that the ability to contain the water between analyzed NG varies from −1.62 % to 2.11 %, see Fig. 2.

To draw the final conclusions for future applications of the modified PR EoS (GERG model) in the Slovak gas distribution system, the results from Fig. 1, Table 2 and Fig. 2 should be checked with other experimental data in the future analyses together with

Experimental and calculated water content (mole fractions) of the various NG-water systems by using PR EoS (GERG-model) Table 2

Experimental data					Calculations Peng-Robinson EoS (GERG-model)	
NG n°	T	p	Data source	$y_{w,exp} \times 10^6$	$y_{w,calc} \times 10^6$	error
	K	MPa		mol	mol	%
1	250.95	3.440	[12]	32.300	24.628	−23.75
1	255.35	3.440	[12]	47.700	38.175	−19.97
1	260.05	3.440	[12]	71.400	59.866	−16.15
1	264.75	3.440	[12]	105.000	92.215	−12.18
1	266.75	3.440	[12]	123.000	110.247	−10.37
1	271.05	3.440	[12]	171.200	160.218	−6.41
1	271.95	3.440	[12]	183.300	172.960	−5.64
1	250.55	6.890	[12]	14.800	11.693	−20.99
1	253.25	6.890	[12]	19.000	15.546	−18.18
1	255.55	6.890	[12]	23.200	19.698	−15.10
1	259.15	6.890	[12]	33.600	28.233	−15.97
1	260.65	6.890	[12]	38.300	32.683	−14.67
1	264.15	6.890	[12]	51.700	45.621	−11.76
1	269.15	6.890	[12]	74.900	72.116	−3.72
2	268.15	1.020	[11]	4.514	4.053	−10.21
2	273.09	1.063	[11]	6.857	5.874	−14.34
2	278.15	1.007	[11]	8.884	8.875	−0.10
2	283.14	1.018	[11]	13.715	12.341	−10.02
2	288.15	1.012	[11]	17.925	17.234	−3.86
2	288.15	6.017	[11]	3.460	3.223	−6.86
3	250.92	0.491	[13]	120.000	169.918	41.60
3	256.64	1.000	[13]	120.000	144.383	20.32
3	260.07	1.490	[13]	120.000	132.973	10.81
3	264.15	2.011	[13]	120.000	141.863	18.22
3	266.87	2.509	[13]	120.000	143.945	19.95
3	269.04	2.994	[13]	120.000	144.981	20.82
3	255.37	0.477	[13]	210.000	268.432	27.82
3	261.80	0.998	[13]	210.000	232.088	10.52
3	266.92	1.557	[13]	210.000	233.279	11.09
3	269.42	2.025	[13]	210.000	221.855	5.65
3	256.53	0.498	[13]	310.000	286.769	−7.49
3	263.15	0.968	[13]	310.000	269.890	−12.94
3	268.11	1.536	[13]	310.000	261.834	−15.54
3	270.54	1.991	[13]	310.000	247.899	−20.03
4	263.15	1.500	[14]	159.700	175.413	9.84
4	263.15	6.000	[14]	50.600	43.347	−14.33
4	273.15	1.500	[14]	365.100	410.979	12.57
4	273.15	4.000	[14]	129.700	154.799	19.35
4	273.15	6.000	[14]	102.100	102.539	0.43
4	283.15	6.000	[14]	226.300	207.474	−8.32

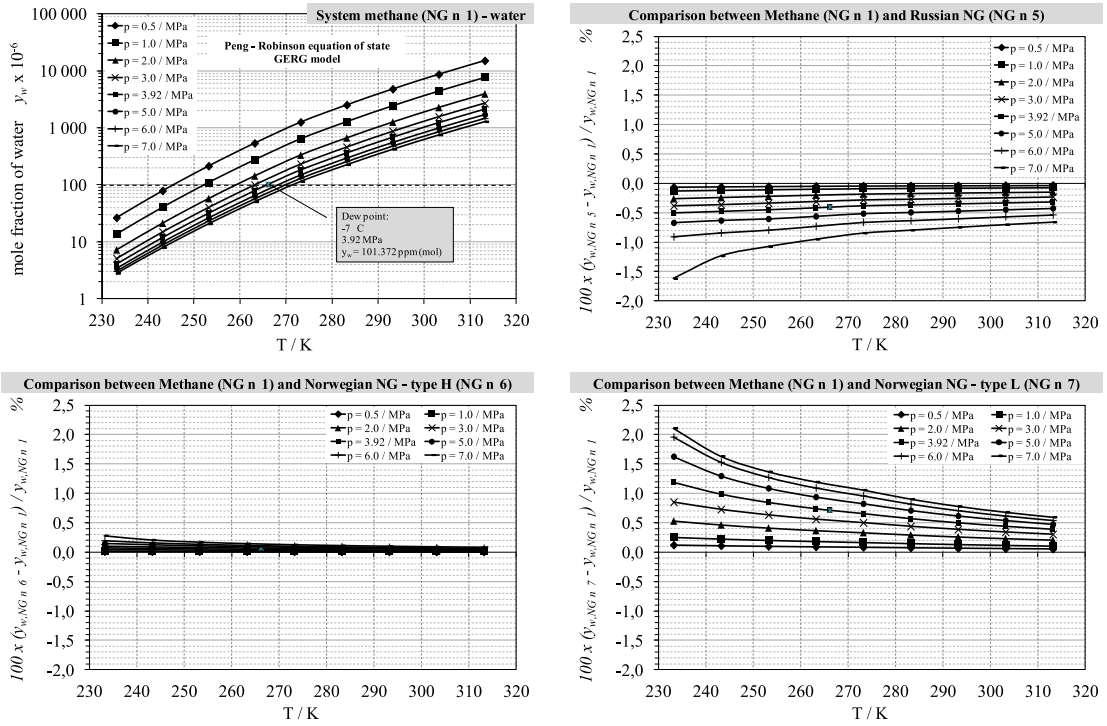

Fig. 2 *Water content calculations of the methane (NG n°1) - water and NG n° 5, 6, 7 - water systems and comparison between them from maximum water content point of view by using modified PR EoS (GERG model)*

the model in order to make the necessary improvements and to achieve the scope to have an accurate computational tool for the calculations of the gas maximum water content in the critical parts of the gas distribution system.

As it is clear from the experimental data and results of various PR EoS with modifications and for selected NG, binary interaction parameter k_{ij} (between various components of the NG) and energy temperature dependent term $\alpha(T_r)$ for various components of NG highly influence the results of the water content calculation in the system gas-water. Acceptable agreement was achieved between the experimental and calculated results by using modified PR EoS (GERG model), but various areas of improvements should be applied. The classical approach can be in more precisious correlations of binary interaction parameter k_{ij} and energy term $\alpha(T_r)$ based on experimental data for various temperature ranges. Today trends are based on using CPA (Cubic Plus Association) method, for futher readings see [10]. CPA combines the classical simple PR EoS with an advances association term. Associating systems are those which contain compounds capable of hydrogen bonding (e.g. water or some inhibitors for gas hydrate prevention, etc.). The scope is to describe better the dense phases (i.e. the gas phase or the liquid water phase) coupled a solid phase model, which can be an ice or hydrate model.

4. Conclusion

The presented PR EoS (GERG-model) will be in the next work after necessary modifications applied in the Slovak gas distribution dispatching system implemented into the SCADA (Supervisory Control and Data System). The goal is to optimize energy requirement for NG heating before its throttling into gas pressure reduction stations. So, it's necessary to identify crucial stations for dew point (or maximum water content) measurement and recalculate these data for other groups of stations where such measurement is not performed. In case of the Slovak Republic we are speaking about 1700 crucial selected pressure reduction stations with basic splitting by nominal pressures PN 65, PN 40 and PN 25.

Acknowledgement

I would like to thank to non-investment fund EkoFond, n. f. (www.ekofond.sk) for the financial support of project 563/PG04/2011: Reduction of energy consumption at gas pipeline system by application of new hydrate models.

References

[1] KNIZAT, B., TOTH, P., RAJZINGER, J., GOLHA, M., SALAJ, M.: *Numericke riesenie a citlivostna analyza vonkajsich faktorov na parametre plynarenskych sieti [Numerical Solution and Sensitivity Analysis of External Factors on Parameters of Natural Gas Pipeline Network].* Vyskumna sprava ulohy 40/98, STU, Strojnicka fakulta, Bratislava, 2001

[2] SLOAN, E. D., KOH, C. A.: *Clathrate Hydrates of Natural Gases.* 3rd edition. New York : CRC Press, 2008, ISBN-10: 0471661740

[3] JANDACKA, J., MALCHO, M.: *Unasanie pevnych castic prudiacim plynom v plynovodoch [Adrifting of Solid Particles by Flowing Gas in Natural Gas Pipelines].* Slovgas. 2007, XXII, No. 6, pp. 22–24

[4] MICUCCI, L.: Technology of Choice. Discusses a New Method of Natural Conditioning for Long Pipeline Transportation. *Hydrocarbon Eng.,* vol. 15, No. 10, 2010, pp. 67–70

[5] MASARYK, M.: *Vypoctove a experimentalne overenie zmesi chladiv R12/R134a v malych chladiacich zariadeniach [Numerical and Experimental Verification of R12/R134a Cooling Fluids in Small Refrigeration Devices].* PhD Thesis, Slovak University of Technology in Bratislava, Bratislava, 1994

[6] SANDLER, S. I.: *Chemical, Biochemical, and Engineering Thermodynamics - 4th edition,* New York : John Wiley & Sons, 2006, ISBN-10: 0471661740

[7] ZUCKERWAR, A. J.: *Handook of the Speed of Sound in Real Gases,* vol. III, Speed of Sound in Air. New York : Academic Press, 2002, ISBN: 0-12-782513-4

[8] EDMISTER, W. C., LEE, B. I.: *Applied Hydrocarbon Thermodynamics,* vol. 1 – 2nd edition. Houston : Gulf Professional Publishing, 1984, ISBN: 0-87201-855-5

[9] ISO 18453:2004: *Natural Gas - Correlation between Water Content and Water Dew Point:* The International Organization for Standardization, July 2004

[10] KONTOGEORGIS, G. M., FOLAS, G. K.: *Thermodynamic Models for Industrial Applications. From Classical and Advanced Mixing Rules to Association Theories,* John Wiley & Sons, 2010, ISBN: 978-0-470-69726-9

[11] CHAPOY, A.: *Etude des Equilibres des Systems: Eau-Hydrocarburez-Gaz Acides dans le cadre de la production de Gaz.* PhD. Thesis, Paris : Ecole des Mines de Paris, 2010

[12] CHAPOY, A., HAIGHIGHI, H., BURGASS, R., TOHIDI, B.: Gas Hydrates in Low Water Content Gases. Experimental Measurement and Modeling Using the CPA Equation of State. *Fluid Phase Equilibria 296,* 2010, pp. 9–14, ISSN: 0378-3812

[13] BLANCO. S. T., AVILA. S., VELASCO. I., RAUZY. E., OTIN. S.: Dew Points of Ternary Methane + Eethane + Butane and Quaternary Methane + Ethane + Butane + Water Mixtures: Measurement and Correlation. *Fluid Phase Equilibria 171,* 2000, pp. 233–242. ISSN: 0378-3812

[14] FOLAS. G. K., FROYNA. E. W., LOVLAND. J., KONTOGEORGIS. G. M., SOLBRAA. E.: Data and Prediction of Water Content of High Pressure Nitrogen, Methane and Natural Gas. *Fluid Phase Equilibria 252,* 2007, pp. 162–174. ISSN: 0378-3812.

Andrej Kapjor – Milan Malcho – Jozef Jandacka – Jozef Huzvar – Tomas Gressak *

OPTIMIZATION OF CONSTRUCTION PARAMETERS OF A FLOOR CONVECTOR

The paper deals with optimization of construction parameters of a floor convector with natural convection. Intensification of heat transfer from the floor convector with an objective to achieve the highest possible thermal performance of the floor convector was performed by CFD method and criterion equations at boundary conditions, like ambient temperature 20°C and the temperature of the heating medium 75/65°C in thermostatic chamber.

Keywords: *Floor convector with natural convection, rib, spacing.*

1. Introduction

Floor convectors are heating bodies used in the places where it is necessary to install heaters with a low construction height or where these heaters are to be mounted into the construction of the floor. To achieve the highest possible thermal performances of floor convectors with natural convection with the maximum construction height up to 100 mm some experimental measurements to optimize construction parameters of the floor convector were made in a thermostatic chamber.

2. Construction of a floor convector

The floor convector consists of the following elements: grille (wooden or metal), trim frame and housing. The most important part is the exchanger placed in the housing. The exchanger is composed of a copper tube with molded aluminum fins to achieve a higher thermal performance. Exchangers usually have matrices with an internal diameter G 1/2“ on the one side, and welded air vent on the other side. All this parts we can see at Fig. 1.

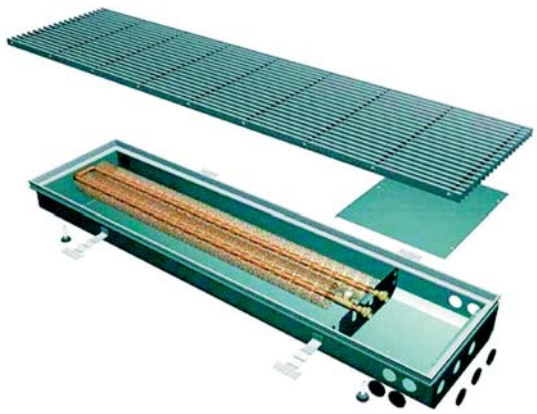

Fig. 1 Part of a floor convector

3. Heat transfer and floor convectors

The process of heat transfer by the floor convector with natural convection from the heat transfer medium into the ambient air can be divided into (Fig. 2):

1. heat transfer from hot water to the tube wall,
2. heat transfer through the tube wall and heat transfer in the rib (conduction), and
3. heat transfer from the outer tube wall and heat transfer from the rib wall to the air by free convection.

The problem of heat transfer from the floor convector with natural convection can be solved analyzing the basic equations of conservation of (mater, energy, and impulse) and equations of state describing a thermodynamic situation of flowing gas, on the basis of loss calculations for flow, equations of heat transfer and relations for properties of substances. The quantification of thermal flows in real equipment is, owing to the complicated flow fields, most frequently carried out by means of criterion equations.

To simplify and speed up optimization processes, the model of heat transfer from the floor convector with natural convection was constructed on the basis of criterion equations. First of all, the optimal rib spacing at different ribbing heights was looked for to optimize floor convectors with a construction height up to 100 mm. Consequently, the rib thickness enabling the highest performance

* **Andrej Kapjor, Milan Malcho, Jozef Jandacka, Jozef Huzvar, Tomas Gressak**
Department of Energy Technology, Faculty of Mechanical Engineering, University of Zilina, Slovakia, E-mail: andrej.kapjor@fstroj.uniza.sk

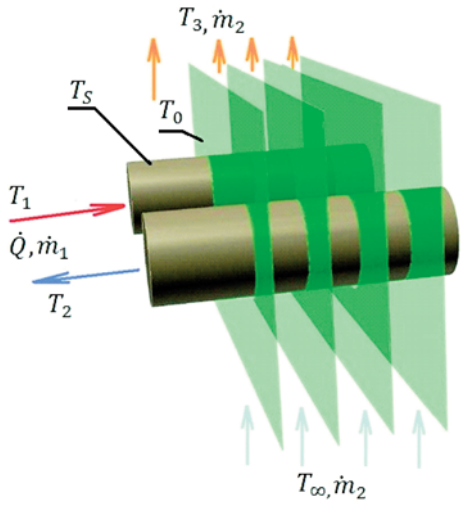

Fig. 2 Heat transfer by a floor convector from the heat transfer medium to the ambient air

of the floor convector at various rib heights was looked for. As the above mentioned process of heat transfer from the floor convector to the ambient air takes place in the housing of the convector, we also investigated the influence of the housing itself on the floor convector performance.

The optimization itself was performed on a sample of the floor convector having a length of the ribbed surface 740 mm because experimental measurements were also made on floor convectors having the same length, which enabled us to compare and verify the calculation model with real measurements of floor convectors in a thermostatic chamber. The calculation model of the floor convector was set up on the basis of criterion equations of probability theory. This calculation model consists of heat transfer from the heat transfer medium to a tube, of heat transfer through a tube, of heat transfer through a rib and thermal decomposition on a rib by means of Bessel functions, of the calculation of the ribbed surface efficiency, of heat transfer from parallel plates and of heat transfer from a horizontal tube. As the floor convector performance depends on all the above mentioned heat transfers, a mathematical model of the convector was set up from individual sub-processes in Excel. The individual models were interconnected so that the whole calculation could iterate on condition that the heat transferred by forced convection from the heat transfer medium to a tube had to be delivered by the floor convector on the air side by means of natural convection and radiation.

The calculation has to contain boundary conditions such as temperature of the heat transfer medium, ambient temperature, and a diameter of a tube with molded ribs. The convector thermal performance changes with the change in the input parameters. Their influence on the thermal performance can be seen from the following dependences. Criterion equations for individual processes of heat transfer are to be found in [1], [2] and [3].

4. Optimization of construction parameters of a passive floor convector

As the performance of a floor convector depends on more construction parameters of the convector it is good to optimize them simultaneously. From these optimizations a 3-D Graph1 was set up. It illustrates the dependence on the spacing and height of a rib at the ambient temperature 20 °C, at the temperature of the heat transfer medium 75/65 °C, pipe diameter 18 mm and at the rib thickness 0.25 mm. This model served for finding the optimal rib spacing at various rib heights to achieve the highest possible thermal performance of the floor convector. From the graphs and calculations it can be seen that the optimal spacing of ribbing at the ambient temperature 20 °C and temperature of heat transfer medium 75/65 °C is 5.5 mm at the rib height 60-100 mm, although according to the analyses of boundary layers a greater spacing is ideal. The use of

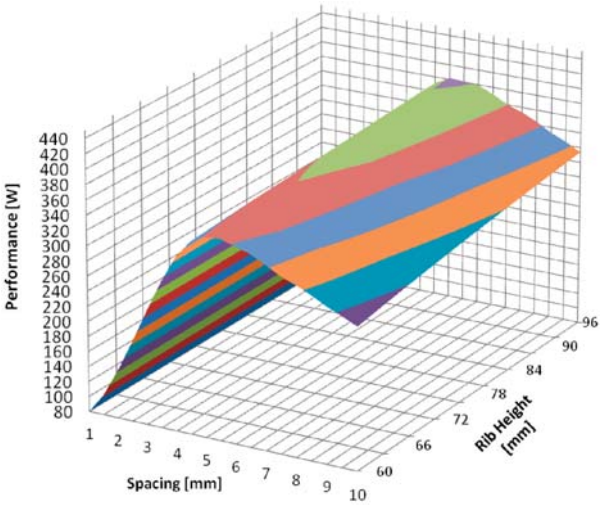

Graph 1 Performance of floor convector in dependence on rib spacing and height at the ambient temperature 20 °C, temperature of heat transfer medium 75/65 °C, pipe diameter 18 mm and rib thickness 0.25 mm

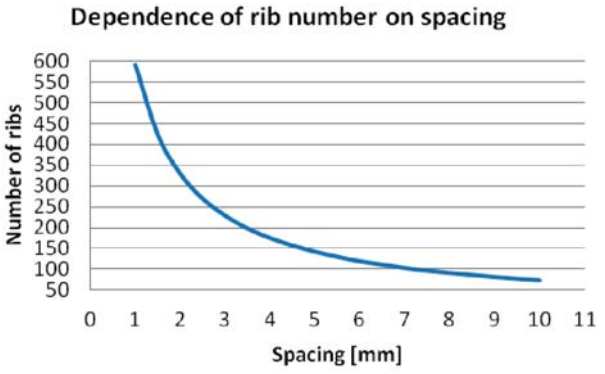

Graph 2 Dependence of rib number on spacing of ribbed surface at a ribbing length 740 mm

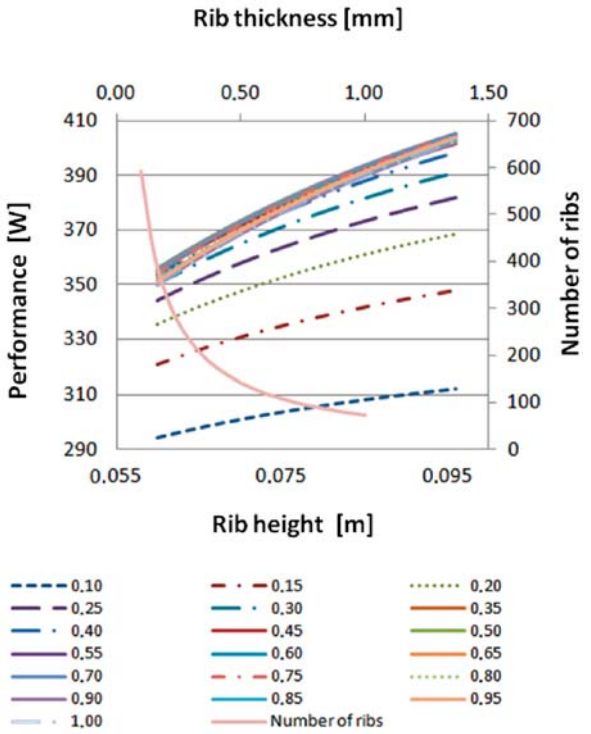

Graph 3 Performance of floor convector in dependence on rib thickness and height at the ambient temperature 20 °C, temperature of heat transfer medium 75/65 °C, pipe diameter 18 mm and at a rib spacing 5.5 mm

greater spacing would result in reduction of heat transfer surface, thus leading to the reduction of the total thermal performance of the floor convector. On the Graph-2 we can see dependence of rib number on spacing of ribbed surface at ribbing length of floor convector 740 mm.

For further increase in the thermal performance of the model floor convector with natural convection, another model was created. The knowledge gathered from previous optimization was used, namely the rib spacing 5.5 mm, which showed to be the most suitable. In this model the dependence of thermal performance on the rib height (60-100 mm) and thickness (Graph3) was modeled. The influence of the rib height and thickness on the total performance of the floor convector can be seen in the graph. The floor convector performance grows with the increasing height of the rib, which is natural as the heat transfer surface also extends. An important finding though is a considerable influence of the rib thickness on the total thermal performance dissipated to the air by means of natural convection, which can be best observed in Graph4. In this graph it is possible to observe a considerable influence of the floor convector rib thickness on the total performance at individual heights of the rib (for better illustration only some performance curves of the model floor convector were chosen), where, for example, at the rib height 60 mm the ideal rib thickness is 0.55 mm (thermal performance 355.9 W); at the rib height 80 mm the ideal thickness is 0.6 mm (387.52 W) and at the rib height 96 mm it is as many as 0.65 (405.4 W). It is also obvious that further increase in the rib thickness does not result in the increase of performance due to following two reasons: when increasing the rib thickness within the same total length of the ribbed surface, the number of ribs decreases (reduction of heat transfer surface); even if the amount of heat supplied to the rib increases, which results in equalization of the rib temperature, we are unable to dissipate it into the surroundings by means of natural convection.

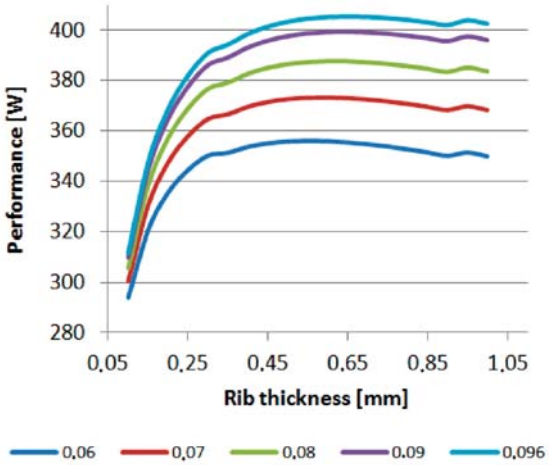

Graph 4 Floor convector performance in dependence on the rib thickness and height at ambient temperature 20 °C, heat transfer medium temperature 75/65 °C, pipe diameter 22 mm and at a rib spacing 5.5 mm

5. Optimization of geometry of the floor convector housing

Experimental measurement for optimization of the floor convector housing and its influence on the performance was made on a sample of the floor convector with the following construction parameters: length of ribbed surface 740 mm, rib height 60 mm, rib length 123 mm, rib thickness 0.25 mm, rib spacing 4 mm and pipe diameter 18 mm. The temperature of heat transfer medium (temperature gradient) was 75/65 °C and temperature of ambient air was 20 °C.

The floor convector was placed in the back part of the thermostatic chamber. An objective of this measurement was to find the most convenient slope of both the front and back sides of the floor convector housing on the performance itself.

First, we were changing the slope of the front side of the housing starting from 0°, when the front side of the housing was completely open, up to 90°, when it was completely closed. Gradually, the measurements were made for 0°, 15°, 30°, 45°, 60°, 75° and 90° slope of the front side of the housing. From these optimizations

Graph5 illustrating the dependence of the floor convector performance on the slope of the front side of the housing was set up. It can be seen from the graph that at a slope of 0° (when the front side of the convector housing was completely open), the floor convector achieved the highest performance. The convector performance was the lowest at a slope of 90° (the front side of the housing was completely closed).

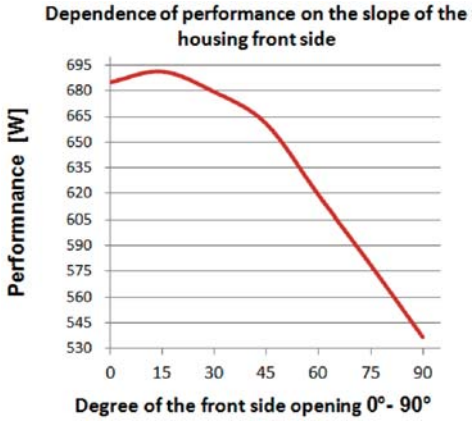

Graph 5 Dependence of the floor convector performance on the slope of the housing front side

Having completed the changes in the slope of the housing front side, we changed, in a similar way, the slope of the housing back side. It can be seen from Graph6 that similarly as in the case of the slope of the housing front side, the performance of the floor convector is the greatest at the complete opening (0° slope of the housing) and the lowest at the complete closing (90° slope of the housing). Graph7 illustrates the performance differences at the slope of the front and back sides of the floor convertor housing. The difference is due to the fact that at the opening of the back side of the housing the heat transferred to the space washes the back wall of the thermostatic chamber which is cold. Thus the warm air from the convector is mixed with the cold wall and swirls occur, which results in reduction of the thermal performance. The occurrence of whirls can be seen in Fig. 3, in which the floor convector model was created by means of CFD simulation in the program Ansys 12.0. Fig. 3 presents air flow trajectory with velocity contours where the occurrence of swirls can be seen in the wall area of the thermostatic chamber.

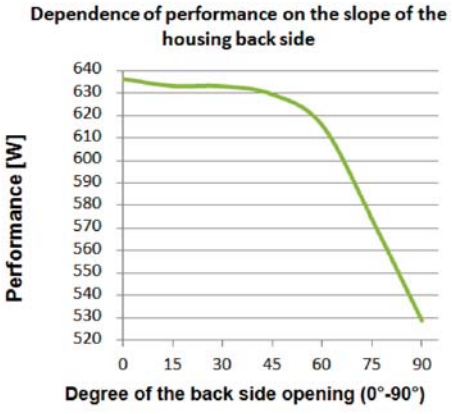

Graph 6 Dependence of the floor convector performance on the slope of the housing back side

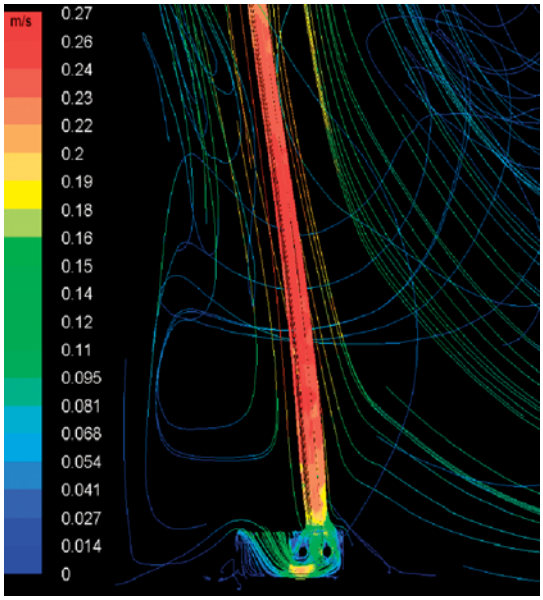

Fig. 3 Air flow trajectory with velocity contours

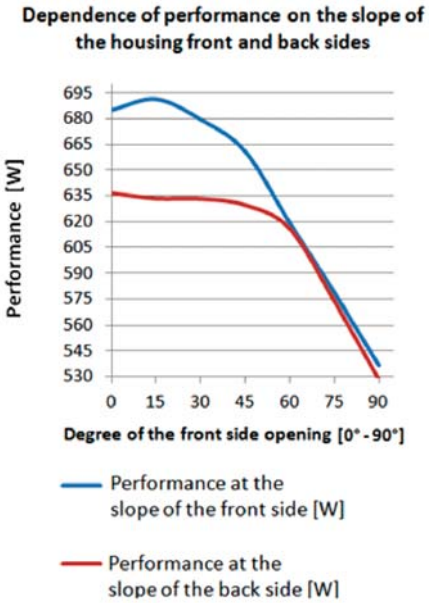

Graph 7 Comparison of the floor convector performance in dependence on the slope of front and back sides of the housing

The last measurement we made dealt with the influence of the slope of both sides of the housing on the floor convector performance. The slope of the housing sides was changed simultaneously, again in the range from 0° up to 90°. Graph 8 illustrates the dependence of the floor convector performance on the slope of both sides of the housing. From the graph it follows that similarly as in the previous cases, the floor convector performance is the highest at the complete opening of the housing and the lowest at the complete closing of the housing. The influence of the housing on the heat spreading from the floor convector can be compared in Figs. 4 and 5 which present visualizations of thermal fields from the sample of the floor convector made by means of CFD simulations in program Ansys. Comparing the figures we can see a considerable influence of the housing on the flow of air to the surrounding areas [4], [5].

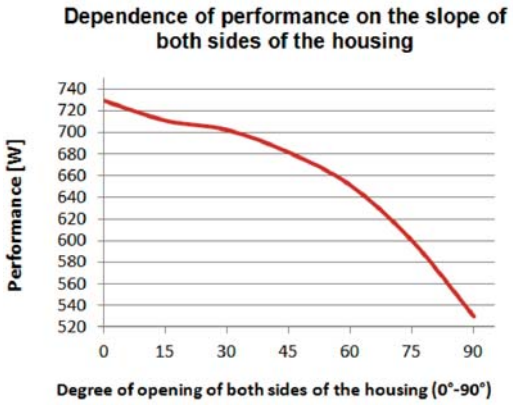

Graph 8 Floor convector performance in dependence of the slope of the housing both sides

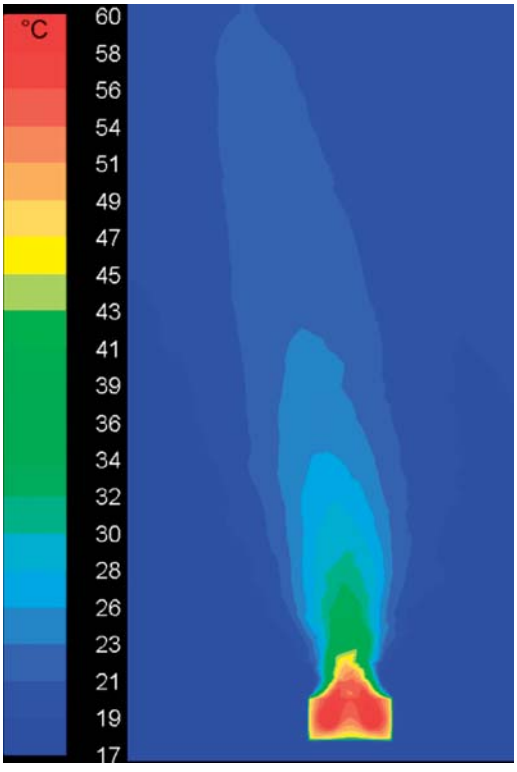

Fig 4 Visualization of thermal field from a sample of a floor convector without housing

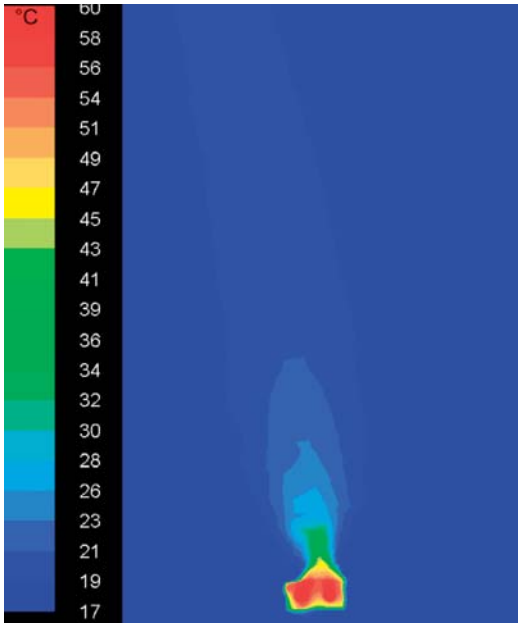

Fig. 5 Visualization of thermal field from a sample of a floor convector with housing

6. Conclusion

From the analysis of individual simulation calculations it can be seen that for the floor convector with natural convection having the ribbed surface length of 740 mm, at temperature gradient 75/65 °C and ambient temperature of 20°C with the tube diameter 18 mm, with the rib length of 123 mm at the rib thickness 0.25 mm (the rib thickness used by a majority of floor convector manufacturers) is the optimal rib spacing 5.5 mm, where at the rib height 60 mm it features the thermal performance 344.395 W, at the height 80 mm it features the performance 368 W and at the rib height 96 mm its thermal performance is 382 W. At further analyses and model creation in dependence of the rib height (60–100 mm) and rib thickness a considerable influence of the rib thickness on the floor convector performance was observed. The performance of modeled floor convector at identical boundary conditions increases with the increasing rib thickness which caused the increase of thermal performance at the rib height of 60 mm up to 355.94 W, at the height 80 mm up to 387.52 W and at the height 96 mm up to 405.44 W at the same lengths of ribbed surface as at the rib

thickness of 0.25 mm. It is also obvious that the performance of a floor convector is, to a certain degree, influenced by the housing geometry. At the complete opening of the front side of the housing the thermal performance achieved 648.88 W, and at the complete closing the thermal performance value was 536.75 W. The thermal performance at the complete opening of the back side of the housing achieved the value 636.38 W and at the complete closing of the back side it achieved the value 528.56 W. At the change of slope of both sides of the housing the thermal performances achieved at the complete opening the value 729 W and at the complete closing it achieved the value 529.38 W.

It deals with the optimization of geometric shapes of floor convectors at the lowest material and production costs with an objective to achieve their maximal performance parameters.

This paper was written within the project VEGA-1/1127/11

References

[1] KAPJOR, A.: *Optimization of Construction Parameters of Passive Floor Convectors.* Dissertation thesis. Zilina 2009
[2] REMSBURG, R.: *Thermal Design of Electronic Equipment.* Boca Raton : CRC Press LLC, 2001
[3] FRANK, P, INCOPERA, D., DEWIT, P. et al.: *Fundamentals of Heat and Mass Transfer,* John Wiley & Sons
[4] DOBAKOVA, R., BRESTOVIC, T.: Calculation of Thermal Loss of Above-Ground and Underground Trenchless Pipe Laying by Means of Program VTSP. *Strojarstvo,* June 2008, pp. 18-19th Meeting of departments of fluid mechanics and thermomechanics, 2009. Demanovska dolina. ISSN 1335-2938.
[5] VITAZEK, I.: *Thermal Technology and Waterworks – second unchanged edition.* Nitra : SPU publishers, 2008, 104 p.

Frantisek Urban – Lubor Kucak – Jozef Bereznai – Marian Pulmann – Jozef Tihanyi *

INFLUENCE OF THE MIXING GRID POSITION ON THE COOLANT FLOW AT THE OUTFLOW PART OF THE NUCLEAR REACTOR FUEL ASSEMBLY PHYSICAL MODEL AND VALIDATION OF CFD MODEL

In the year 2007 an experimental device with a physical model of the VVER 440 nuclear reactor fuel assembly was installed in the laboratory of The Institute of Power Engineering of the Faculty of Mechanical Engineering of the Slovak University of Technology in Bratislava. Within the framework of the reconstruction a third measuring plane was added to the original two, new combined probes were designed with temperature resistant sensors instead of the thermocouples, and piezoelectric pressure sensors for each probe were used. In this article we investigate the influence the mixing grid positioning has on smoothing the temperature profile in the fuel assembly outlet. The preliminary results of the ongoing validation of CFD simulations by means of experimental data are presented.

Keywords: *Nuclear reactor, fuel assembly, physical model, mixing grid position, measurements, CFD, validation*

1. Introduction

Coolant flows along a 126 fuel rod bundle in the VVER 440 nuclear reactor fuel assembly. During the nuclear reactor operation, the temperature fluctuation is irregular in each single fuel rod, depending on the fuel properties and the position of the fuel assembly in the reactor. In the fuel assembly outlet the coolant temperature profile is irregular. In the fuel assembly, at the point where the flow cross section changes from hexagonal to circular, a mixing grid, which flattens the coolant temperature profile, is located. Subsequently, the coolant flows through the fuel assembly outlet where the cross section shape and area change. The next step in smoothing the coolant temperature profile is performed by a catcher. Coolant temperature in the fuel assembly outlet is measured by a thermocouple located in the fuel assembly axis, and is positioned 300 mm from the end of the fuel rods (Fig. 1, plane 3). Measurements are provided at only one point. Safe and effective loading of nuclear reactor fuel assemblies demands qualitative and quantitative analysis of the relationship between the coolant temperature in the fuel assembly outlet, measured by the thermocouple, and the mean coolant temperature profile in the thermocouple plane position. It is not possible to perform the analysis directly in the reactor, so it is carried out using measurements on the physical model, and the CFD fuel assembly coolant flow models. The CFD models have to be verified and validated in line with the temperature and velocity profile obtained from the measurements of the cooling water flowing in the physical model of the fuel assembly.

2. Experimental device with physical model of nuclear reactor fuel assembly

In the laboratory of The Insitute of Thermal Power Engineering of the Slovak University of Technology in Bratislava, a physical experimental copy of the fuel assembly model of a VVER 440 nuclear power plant was installed. The model was created to a scale of 1:1.125. The measurements on the model were made with different water mass flow at four different positions of the mixing grid. The temperature and velocity profiles were measured with 2 combined probes located in 3 planes at the outlet of the fuel assembly in the physical model (Fig. 1):

- plane 1 is situated between the end of fuel rod boundle and mixing grid,
- plane 2 is situated behind the mixing grid and the end of central the tube at the begining of the cylindrical head of the fuel assembly outlet,
- plane 3 is positioned at the nuclear reactor fuel assembly thermocouple.

Knowing the relationship between experimentaly measured and CFD calculated coolant temperature at the fuel assembly outlet, and mean coolant temperature in the plane of thermocouple position is a necessary condition for safe and efective loading of nuclear reactor fuel assemblies.

Due to the fuel assembly model design, the water pressure, and the temperature during experiments, the velocity and temperature

* **Frantisek Urban, Lubor Kucak, Jozef Bereznai, Marian Pulmann, Jozef Tihanyi**
Institute of Power Engineering, Faculty of Mechanical Engineering of the Slovak University of Technology, Bratislava, Slovakia,
E-mail: frantisek.urban@stuba.sk

profiles mesurements are taken near the automodelling flow region. The coefficient of friction λ is constant, independent of the Reynolds number. The compliance between the size and physical dimensions of the fuel assembly model and the actual reactor fuel assembly is achieved by ensuring the results of measurements on the model correspond with the coolant flow in the real fuel assembly outlet [1].

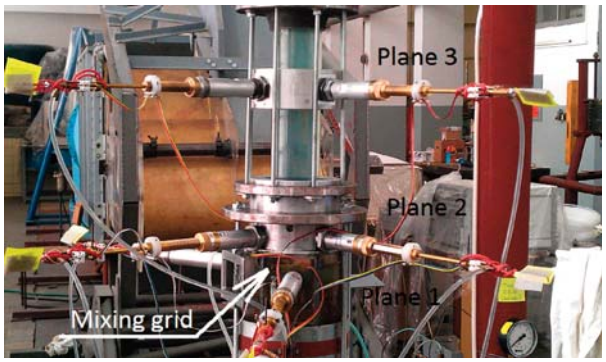

Fig. 1 Physical model of fuel assembly outlet with combined traverse probes devices located in planes 1, 2 and 3

In the plane of the fuel rod bundle ending, temperature discontinuity is modeled by mixing the heated (primary) water that is flowing along fuel rods bundle with cool (secondary) water flowing from one of the tube triplets α, β, γ with an outer diameter of 8 mm and an inner diameter of 5.6 mm (Figs. 2 and 3) and/or a central tube with outer and inner diameters of 10 mm and 8.5 mm respectively (Figs. 2 and 3). Temperature and velocity profiles are measured with the combined probes A1 a B1 located in plane 1 in the zone between the rod bundle end and the mixing grid. Plane 2 is located between the end of the central tube and the catcher, with combined probes A2 and B2. In plane 3, where the thermocouple for measuring outlet water temperature is located in the real fuel assembly, the traverse devices for combined probes A3 and B3 for temperature and velocity profile measurements are installed. At the outlet of the fuel assembly model, water flow mean temperature is measured with a Pt 100 thermometer.

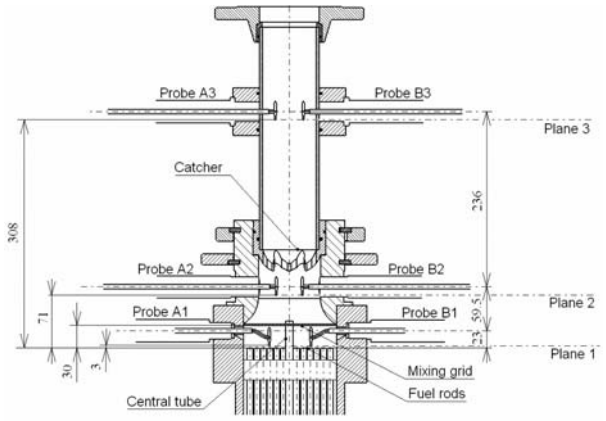

Fig. 2 Outlet of fuel assembly physical model with combined probes in the planes 1, 2 and 3

It is possible to observe the mixing of the water flow through plexiglass walls, using coloured cool water mixed into the fuel assembly outlet through triplet tubes or a central tube.

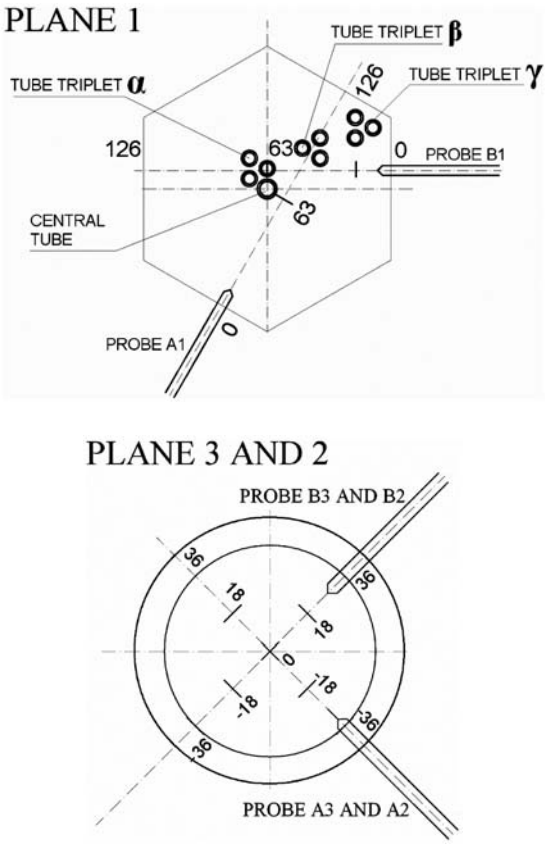

Fig. 3 Location of combined probes A1, B1 in plane 1 and probes A2, B2 behind probes A3, B3 in plane 3

3. Reconstruction of fuel assembly physical model

To reduce uncertainties in temperature and velocity profile measurement of the water flow in the physical model fuel assembly outlet the reconstruction of the physical model of the fuel assembly was made to include new combined probes, and the measurement procedure was modified.

Water flowing through the reactor fuel assembly mixing grid perforation is mixed with cooler water flowing from the central tube. The physical model of the fuel assembly was modified in such a way that 2 new combined probes were placed after the mixing grid. In plane 2 (Fig. 2) temperature and velocity profile of water flowing

between the mixing grid and the catcher is measured. This measurement adds information about the intensity of coolant mixing in the outlet of the fuel assembly model [2].

3.1 Reconstruction of combined probes

In original traversing combined probes for temperature and dynamic pressure measurement were above arc of Pitot probe neck placed tip of thermocouple (Fig. 5, up). In planes 1 and 3 of the fuel assembly physical model outlet, the dynamic pressures and temperatures were measured at an appropriate point.

In order to minimize uncertainties in the measurement of water temperature the thermocouples used in the original 4 probes were calibrated [3]. For the digital thermometer with thermoelectric temperature sensors of type K, with a diameter of 1 mm, the expanded uncertainty of temperature measurement was specified during the calibration. This expanded uncertainty of measurement of 1.10 °C was specified according to TPM 0051-93 and is defined as the standard uncertainty multiplied by coverage factor $k = 2$ (with 95% level of confidence). In view of the measured temperature values of flowing water in the fuel assembly physical model, the expanded uncertainty of 1.10 °C of temperature measurement is too high. This was the reason for the reconstruction of the combined probes, whilst the thermocouples were replaced by miniature resistance thermometers Pt 100 which have a measured temperature deviation of ±0.15 °C [4].

Within the framework of the reconstruction, modification of the original probes and the production of 2 new combined probes with a miniature platinum thermometer was considered. The temperature sensor Pt 100 has a cylindrical shape with a diameter of 2 mm and a 7.6 mm length, with 4 wires. Installing the probe required changes to the combined probes design (Figs. 4 and 5 down).

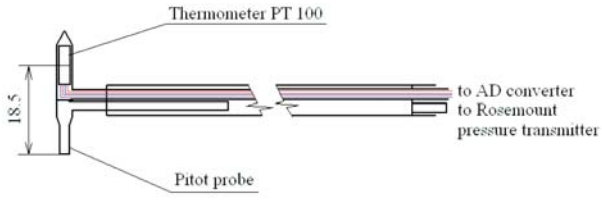

Fig. 4 Schematic sketch of new combined probe for temperature and velocity measurement

The Pitot probe is located in a bush, together with the Pt 100 thermometer (Fig. 5 to the left of probe 1B), but are separated within the bush. The miniature platinum thermometer cannot operate in water, thus it is placed in a brass bush. The new probe requires more space in the measurement zone as can be seen in Fig 5.

For dynamic and static pressure measurement, the piezoelectric pressure sensors are used in Rosemount 2051 transmitters with

Fig. 5 Original combined probe with thermocouple (top) and new combined probe with bush for platinum thermometer (bottom)

a reference accuracy of ±0.075% of voltage. In the last phase of reconstruction each of the 6 combined probes will be installed with an electromotor with appropriate gears to enable fully automized control of the traverse from a personal computer.

4. Measurements by different configurations of mixing grid

The mixing grid has significant influence on coolant mixing in the fuel assembly. It is situated 30 mm behind the plane of the fuel rod endings. The producer supplies the fuel assemblies with the mixing grid installed in two different positions and two more positions are possible by different placing of the assembly in the reactor active zone (Fig. 6). The influence of mixing grid position on water flow in the fuel assembly outlet is analysed in following section.

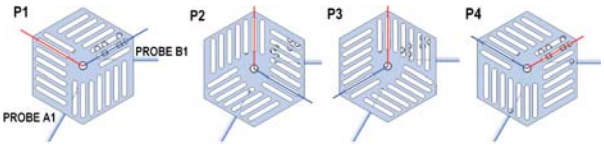

Fig. 6 Positions P1, P2, P3 a P4 of mixing grid in nuclear reactor fuel assembly

The results of measurements made using an isokinetic cold water supply delivered through the α triplet of tubes and a central tube are presented. The modelled water flow was measured using a Venturi meter in the mixing grid positions P1, P2, P3 and P4, within the range from $m_{clona} = 11.12$ kg.s^{-1} (P1) to $m_{clona} = 11.14$ kg.s^{-1} (P4). It was not possible in compared measurements, to keep the temperature of the water in a storage tank at the same level.

In Fig. 7, temperature profiles in plane 1 are illustrated for mixing grid positions P1, P2, P3 and P4. During traversing probe A1 was out of the flow of cool water, therefore the temperature decrease of the t 1A_Px in the middle of the assembly is not significant. Probe B1 is measuring the temperature t 1B_Px in the middle of the assembly influenced by cold water flow through triplet tubes α (Fig. 7, $x = 72$ mm). Differences between water temperatures $t_{max} - t_{min}$ in plane 1 are from 4.50 °C (position of mixing grid P2) to 5.60 °C (P1).

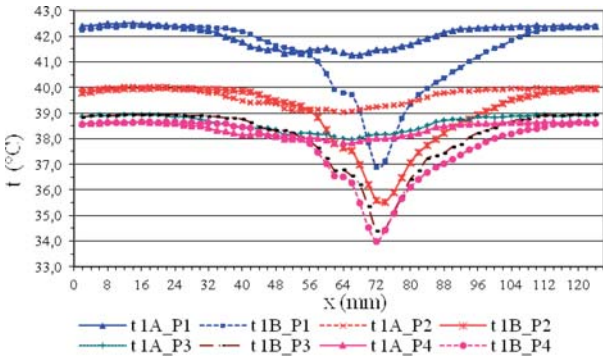

Fig. 7 Temperature profiles in plane 1 for mixing grid position P1, P2, P3 a P4

In plane 2 the temperature profile is smoothed in the periphery of the cross section as a result of the influence of the mixing grid (Fig. 8). The temperature profile is significantly influenced by cool water input from the central tube. Differences of water temperature t_{max} – t_{min} in plane 2 are from 3.20 °C (P3) to 3.92 °C (P1).

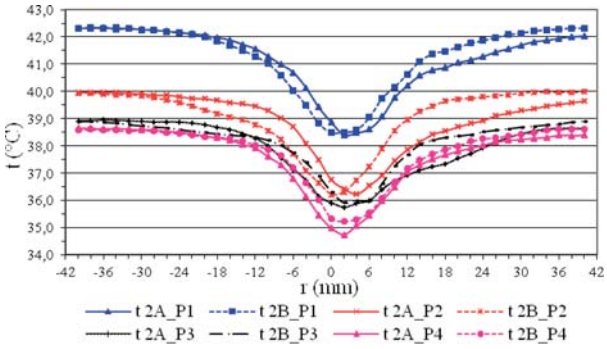

Fig. 8 Temperature profiles in plane 2 for mixing grid position P1, P2, P3 a P4

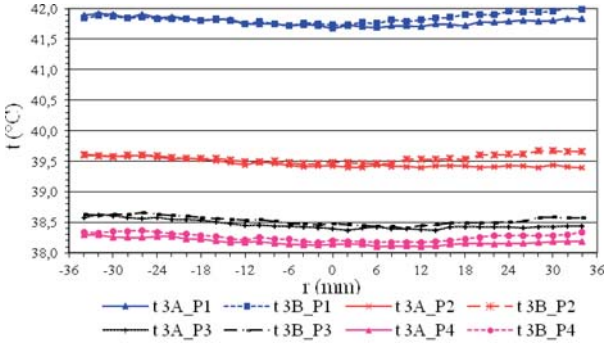

Fig. 9 Temperature profiles in plane 3 for mixing grid position P1, P2, P3 a P4

During water flow between planes 2 and 3 turbulence around the catcher causes another smoothing of the temperature profile in plane 3 – the plane where the thermocouple in the real fuel assembly is positioned (Fig. 9). Differences in water temperatures t_{max} – t_{min} in plane 3 are from 0.15 °C (P4) to 0.33 °C (P1).

5. Validation of CFD fuel assembly model

The CFD simulations of the fuel assembly model have to be validated and verified for the purpose of further computational analysis. The objective is to achieve the maximum accuracy of the CFD simulations compared to real-time experiments. Hence suitable computational mathematical models were sought which would represent the physical phenomena of the experiment with minimal deviations.

With CFD model (Fig. 10) an analysis of three different, unstructured meshes was made: a coarse mesh grid with approximately 200 000 elements; a medium grid with 750 000 elements; and a fine grid with 2 000 000 elements (Fig. 11). An adiabatic wall, with velocity inlet boundary condition and with pressure outlet boundary condition was used for the simulations.

For better correspondence of CFD simulations with the experiment, 4 mathematical turbulence models were tested – standard k-

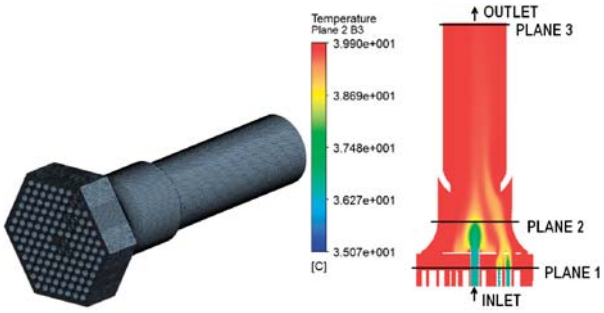

Fig. 10 Computational grid and temperature profile along cut of fuel assembly outlet

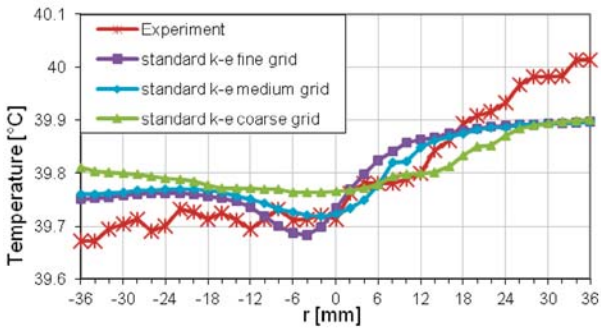

Fig. 11 Meshing grid comparison with calculated temperature profiles in plane 3 of fuel assembly outlet

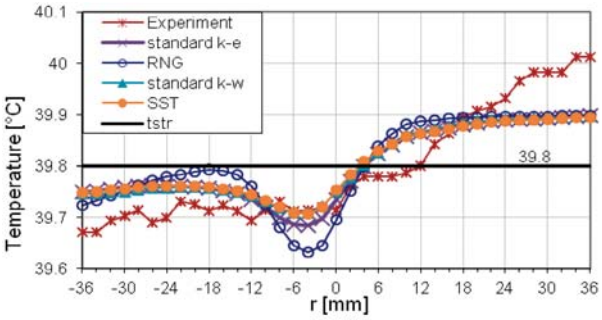

Fig. 12 Turbulence model comparison with calculated temperature profiles in plane 3 of fuel assembly

ε, RNG k-ε, standard k-ω and SST k-ω using the fine mesh (Fig. 12).

The results show large variations at the center of the cross section, with the standard k-ω and SST k-ω models matching the measured data more closely than the RNG model which showed a higher temperature drop at the center of the cross section. The greatest difference between the measured values is 0.34 °C, and the difference between the calculated temperature values of the SST model is 0.20 °C. The turbulence models were unable to match the temperature increase in the last phase of probe traversation where the difference between the measured and calculated values is 0.11 °C. Temperature difference between SST and RNG turbulence models and the calculated mean temperature t_{str} at the position where the thermocouple is positioned in the reactor fuel assembly (Fig. 12, $r = -4$ mm), is 0.08 °C.

An analysis of the influence of the inlet boundary turbulence intensity shows no effect on the temperature profile in the fuel assembly outlet.

6. Conclusion

The third measurement plane that was added in the reconstruction of the VVER 440 nuclear reactor fuel assembly physical model gives us better information about the influence of the central tube coolant flow on the temperature profile in the plane of thermocouple postion in the real fuel assembly (plane 3 on fuel assembly model). Reducing the uncertainties of the measured temperature values was achieved by replacing the thermocouples in the combined probes with a miniature platinum thermometer, and dynamic pressures are measured with pressure transmitters separately for each probe.

The presented results of measurements carried out with isokinetic cold water input through α triplet tube and central tube and water flow for mixing grid positions P1, P2, P3 and P4 within the range from $m_{clona} = 11.12$ kg.s^{-1} (P1) to $m_{clona} = 11.14$ kg.s^{-1} (P4). In the plane of the real fuel assembly thermocouple position – plane 3 of the physical model fuel assembly – the differences between water temperature $t_{3A}(r = 0)$, $t_{3B}(r = 0)$ measured with resistor thermometers at the position of the combined probes A3 and B3 at point r = 0 mm and calculated temperature t_{str3} is between 0.05 °C for mixing grid position P3 and P4, and 0.17 °C for mixing grid position P1. Differences of temperature values are within the range of temperature measurement uncertainty measured with the resistor thermometer. The mixing grid position influences the temperature profile in plane 3 only insignificantly.

So far, from the acquired data of the CFD simulations validation we can conclude that turbulence intensity change at the inlet boundary condition has minimal influence on the outlet temperature profile. Furthermore, on the evidence of the turbulence models tested, the k-ω models match the experimental data more closely than the k-ω models. The next step will be to focus more on investigating the size of the time steps, type and quality of mesh, inlet boundary conditions, and other turbulence models.

Acknowledgements

Preparation of this paper was supported by the Research and Development Operational Programme of the European Union's ERDF through the Centre of Competence in New Materials, Advanced Technologies and energy project, ITMS 26240220073.

References

[1] MUSKAT, P., URBAN, F., PULMANN, M.: Merania na fyzikalnom modeli palivoveho clanku jadroveho reaktora [Measurements on the Physical Model of Nuclear Reactor Fuel Assembly]. *Strojnicky casopis = Journal of Mechanical Eng.,* 2008, vol. 5-6, No. 59, pp. 305-315 ISSN 0039-2472.

[2] BEREZNAI, J.: *Termokineticka a hydraulicka analyza prudenia chladiva v jadrovom reaktore VVER 440 [Thermokinetic and Hydraulic Analysis of the Coolant Flow in the Nuclear Reactor VVER 440]. Dissertation thesis.* Bratislava, 2010, 58 p.

[3] SLANINA, M., REPA, M., CAPUSKA , J.: *Odovzdavaci protokol. Certifikat o kalibracii c. 42/2009 az c. 45/2009 [Handover Protocol. Certificate of the Calibration no. 42/2009 to no. 45/2009].* VUJE, a.s. Trnava. Akreditovane kalibracne laboratorium teploty. Trnava, 29.12.2009.

[4] CHUDY, V., PALENCAR, R., KUREKOVA, E., HALAJ, M.: *Meranie technickych velicin [Measurement of Technical Quantities].* STU, 1999, ISBN 80-227-1275-2.

Ondrej Hladik – Pavel Jonas – Oton Mazur – Vaclav Uruba *

COMPLEX EFFECTS OF FREE STREAM TURBULENCE AND SURFACE ROUGHNESS ON THE TRANSITIONAL INTERMITTENCY

The comparison of transitional intermittency distributions in boundary layers on smooth and rough surface is presented. The conditional analysis of the instantaneous wall friction is applied on time records made in transitional boundary layers originating on smooth surface or surface covered by sand paper. Special procedures of measurement and evaluation are applied that allowed evaluations of turbulent and non-turbulent zone averages.

Keywords: *By-pass transition, rough wall boundary layer, CTA anemometry, instantaneous wall friction, intermittency analysis*

1. Introduction

The problem of joint action of wall roughness (WR) and free stream turbulence (FST) on the boundary layer development is very broad. The laminar turbulent transition plays a major role in boundary layer development so it deserves a special attention. Its relevance is in changes of skin friction, heat transfer and of tendency to flow separation that are caused by increased momentum and scalar diffusion after the transition. The mechanism of how an originally laminar boundary layer on a smooth surface is forced by disturbances penetrating into the layer from environment and of the corresponding routes to turbulent layer were described elsewhere, e.g. [1]. The opinion generally accepted is that the final phase of boundary layer laminar/turbulent transition starts with the occurrence of first turbulent spots regardless of the initial conditions.

The location of the laminar-turbulent transition region can be estimated from the distributions of characteristics derived from the mean flow measurements, especially if their course is known in laminar and turbulent states. This is the case of the flat plate boundary layer. The skin friction coefficient distribution seems most suitable for this purpose.

This paper is a follow up to the investigations of mean flow field in the zero pressure gradient boundary layers on plates with smooth surface and plates with surfaces covered by sandpapers (grits 60, 80 and 100) in turbulent free stream e.g. [2]. The skin friction coefficient value was derived from the mean velocity profile. Then the location of transitional region was carefully estimated by the diversion of the skin friction coefficient distribution from the Blasius solution [3] and by the attachment of the distribution to the Ludwieg and Tillmann empirical curve [4]. The accuracy of this procedure is generally weak, namely in rough wall boundary layers, because of the measurement scatter, of a sparse net of measurement, of a slow change of C_f in the streamwise direction, etc. Fig. 1 illustrates this problem. Intensity Iu, length parameter Le and surface property are described successively in square brackets in caption Fig. 1. Hence it was decided to perform the transitional intermittency measurements in the investigated boundary layers.

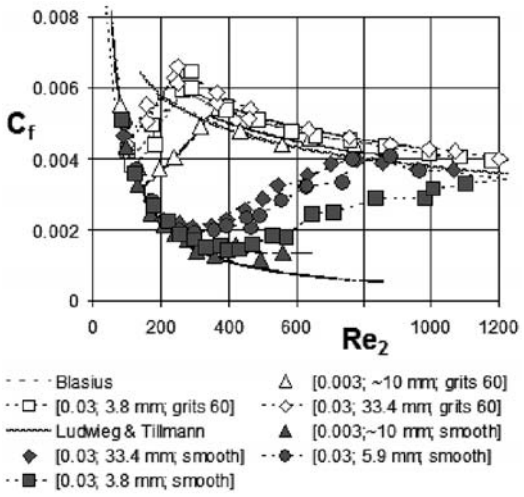

Fig. 1 Skin friction coefficient distributions on smooth and rough flat plates

* **Ondrej Hladik, Pavel Jonas, Oton Mazur, Vaclav Uruba**
Institute of Thermomechanics AS CR, v.v.i., Praha, Czech Republic, E-mail: hladik@it.cas.cz

2. Experimental facility and methods

Investigations of boundary layers developing on smooth or rough plates were performed in the close circuit wind tunnel (0.5 × 0.9 × 2.7 m^3) of the IT AS CR, Prague, Fig. 2.

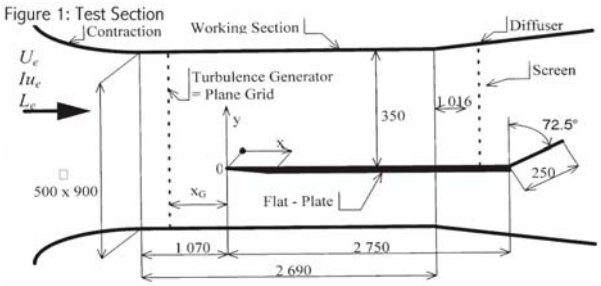

Fig. 2 Scheme of the working section of the wind-tunnel IT AS CR, Prague

The mean velocity of external stream was constant (±0.5%), about 5.0 m/s, during every measurement in the individual profiles of boundary layer in the given configuration.

Boundary layers were developing either on the original smooth plate with the special shape of the leading edge (L.E.), [5], or on the plate covered with sand paper grits 60 with the elliptic shape of the L.E., [2]. The maximum size of grains on sandpaper was chosen as the representative length of the sand paper roughness $s = (0.435 \pm 0.014)$ mm.

Free stream turbulence (FST) was either low – natural with the level 0.3 % and the length scale of order 10^{-1} m or it was amplified by means of square mesh plain grids/screens. Three types of turbulence generators were used, each producing the intensity $Iu = 0.03$ and individually producing the dissipation length parameters $Le =$ = 3.8 mm, 5.9 mm or 33.4 mm at the plane of the L.E. ($x = 0$).

The mean flow boundary layer characteristics were evaluated from the mean velocity profiles measured in the investigated sections x (const). Two single wire probes working in the CTA mode were used in the smooth wall configuration. The first reference probe, placed in a fixed position in the outer stream, serves as the indicator of the reference velocity. The second probe, the profile probe, was put into position by a traversing system in the streamwise direction x and in the direction y normal to the surface. The distance y was measured with an accurate cathetometer. Digital records of the output signals were acquired simultaneously and then records of the relevant instantaneous velocities were evaluated using data from the calibration measurements performed prior to the experiment. Next, the correction [6] of the wall proximity effect on hot-wire cooling was applied. The instantaneous wall friction time series $\tau_w(t)$ are the by-product of wall corrections.

Measurements in the rough wall configuration require more resistant probes than HW-probes for the essential measurements. The couple of the flattened Pitot tube (probe tip: 0.18 mm × 2.95 mm) and the round nosed static pressure probe (diameter = 1.8 mm) serves as the profile probe and the Pitot-static probe (diameter = 6 mm) is the indicator of the reference velocity. The instantaneous wall friction measurement is carried out by means of a wall hot wire probe step-wise moving in the streamwise direction in the distance from the rough surface $y_0 \sim 0.3$ mm. The probe (calibrated in advance) is attached to the three wheels truck connected to the traversing system. The probe is working in the CTA mode and the output voltage is recorded. Next, these records are digitally transformed using calibration parameters into the records of the local nominal instantaneous velocity. The CTA output signals processing follows assuming the adjusted y0 like that in the smooth wall case with one important difference. Irregular variations of the true distance y_w from the adjusted one y_0 are of the order hundreds millimetre and vary with the location x. Thus an auxiliary local correction of y_w must be made. The correction equals the time averaged skin friction coefficient determined from the mean velocity profile with the mean value of skin friction coefficient calculated from the CTA measurement in the given location x_j. The instantaneous wall friction $\tau_w(t)$ is evaluated using the corrected distance yw in the vicinity of x_j.

The instantaneous wall friction records (25 kHz, 750000 samples, 16 bit) were utilized in a statistical analysis of the wall friction in the rough wall boundary layer like in the smooth one.

The applied method of the transitional intermittency analysis is Turbulent Energy Recognition Algorithm-Method, e.g. [7] and the procedure of is very similar to that described in [8] and [9]. The method consists of several consecutive steps. At the first, the obtained records of the instantaneous values of wall friction fluctuations τ'_w are filtered by Butterworth filter with low pass frequency 1 kHz to eliminate noise from the signal. At the second step, the detector function $D(t)$ is derived as to emphasize the differences of the signal time behaviour during turbulent and non-turbulent periods. The detector function is computed after the formula:

$$D(t) = \left|\tau'_w \cdot \partial^2\tau'_w/\partial t^2\right| \tag{1}$$

then the detector function is smoothed to eliminate scales much smaller than those to be recognized, thus the criterion function $K(t)$ is created. The criterion function, the threshold Th and the indicator function $I(t)$ are evaluated successively.

$$I(t_i) = 0 \text{ if } K(t_i) \le Th;\ I(t_i) = 1 \text{ if } K(t_i) > Th \tag{2}$$

The indicator function allows to assort the whole record in the time intervals with turbulent structure ($I = 1$) and those with laminar/non-turbulent structure ($I = 0$). Finally the transitional intermittency factor is calculated (details are presented in [10]).

$$\gamma = \frac{1}{m}\sum_{i=1}^{i=m} I(t_i);\quad m = 750000 \tag{3}$$

This procedure was verified [11] comparing the dimensionless turbulent spot production rates $n^*\sigma$ evaluated by using both the intermittency analysis and the wavelet one [9]. At first the authors

applied the method within the investigation of the smooth flat plate boundary layer developing in the FST with turbulence intensity $Iu = 0.03$ and different values of the FST length parameter [11].

3. Results

3.1 Transition region limits and turbulent spot production

Distributions of the transitional intermittency factor γ against the displacement thickness Reynolds number Re_1 are shown in Fig. 3. They are in the conformity with Fig. 1 and clearly illustrate the significant effect of FST, surface property and their joint action. Results related to smooth wall layers are marked with grey marks, results related to rough wall layers are plotted with empty marks. The shape of marks differentiates after the type of FST (intensity Iu and the length parameter *Le*) as demonstrated in the caption of Fig. 1.

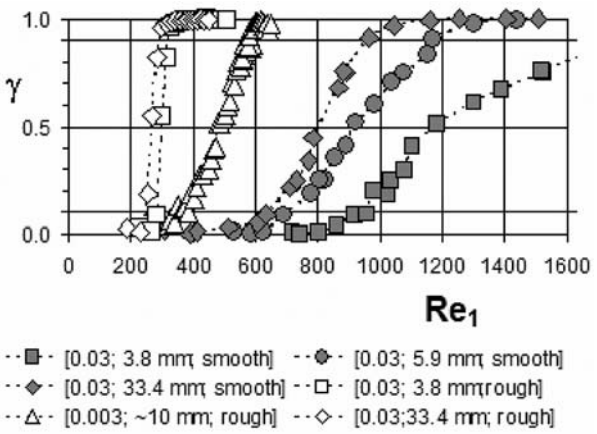

Fig. 3 Intermittency factor versus displacement thickness Reynolds number

The transitional intermittency factor gamma can be expressed after Narasimha [12] in the form involving the spot production rate n (the number of spots occurring per unit time and space distance) and the Emmons [13] dimensionless propagation parameter σ (including both the streamwise and lateral spot growth –, effect of drift)

$$\gamma(x) = 0,\ x \le x_t;\ \ \gamma(x) = 1 - \exp\left[-(x - x_t)^2 n\sigma/U_e\right] \qquad (4)$$

Introducing the local Reynolds number into (4) we can define the dimensionless spot production parameter

$$n^*\sigma(Re_x) = 1 - \exp\left[-(Re_x - Re_t)^2 n^*\sigma\right],$$

$$Re_x = xU_e/\nu,\ \ n^*\sigma = n\sigma\nu^2/U_e^3 \qquad (5)$$

Thence the function F(γ) suitable for the statistical estimates of the transition start and the value of parameter $n^*\sigma$ can be derived

$$F(\gamma) = \sqrt{-\ln(1-\gamma)} = \sqrt{n^*\sigma}\left(Re_x - Re_{xs}\right) = \\ = a_0 + a_1 Re_x \qquad (6)$$

The distributions of intermittency factor can be expressed in the universal form [12] by introducing the new variable ζ

$$\zeta = (Re_x - Re_{ir})/\Delta Re_{ir};$$

$$\Delta Re_{ir} = Re_x(\gamma = 0.9) - Re_x(\gamma = 0.1);$$

$$Re_{ir} = Re_x(\gamma = 0.5) \qquad (7)$$

Then the formula is valid at the configuration smooth surface and low FST level

$$\gamma(\zeta) = 1 - \exp[-\alpha(\zeta + \beta)^2] \qquad (8)$$

The empirical parameters α and β take the values $\alpha = 1.42$ and $\beta = 0.72$ after model proposed by Narasimha [12] or the values $\alpha = 0.6$ and $\beta = 1.05$ according to the model proposed by Johnson and Fashifar [14]. Formerly [11], the agreement of results obtained in smooth wall boundary layer at increased FST level with (8) was confirmed. The data received in rough wall layer under different FST, plotted in Fig. 4 demonstrate also their compatibility with the universal form (8).

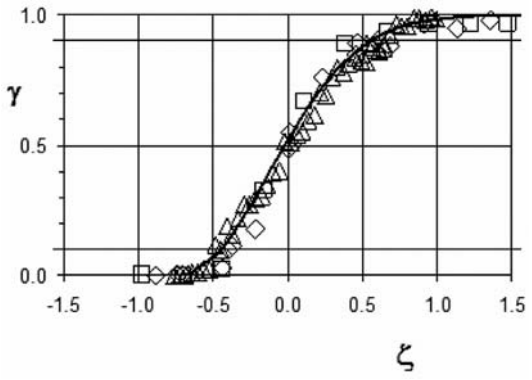

Fig. 4 Universal intermittency function

Starting from the equation (6) the relation can be derived between the dimensionless spot production rate and the Reynolds number defined with the length of transition region. Let the start of transition relates to $\gamma = \gamma_s$ and $Re_x = Re_s$ and similarly the end relates to $\gamma = \gamma_c$ and $Re_x = Re_c$. Substituting into (6) after some formal adaptations the relation is derived

$$n^*\sigma = \left(\sqrt{-\ln\gamma_c} - \sqrt{-\ln\gamma_s}\right)^2 / \Delta Re_{ir}^2;$$

$$\Delta Re_{ir} = (Re_S - Re_C) \qquad (9)$$

the insertion of values $\gamma_s = 0.1$ and $\gamma_c = 0.9$ into (9) results in the formula

$$n^*\sigma = 1.42/\Delta Re_{tr}^2 \qquad (10)$$

The formula (10) and interpolation of Fransson et al [15] are plotted in Fig. 5 together with the authors' results. The received results agree well with the relation (10) regardless the boundary layer is developing on the smooth surface or on a rough one. Apparently turbulent spot production grows and the width of transition region shortens with increasing roughness and with growing FST.

3.2 Conditional analysis of wall friction during laminar-turbulent transition

Having determined the time behaviour of the indicator function $I(t)$, the record of the instantaneous wall friction $(\tau_w(t_i))$ is possible to resolve in individual non-turbulent/laminar events and turbulent events. Every uninterrupted segment of record with $I(t_i)$ = constant (0 or 1) is named event.

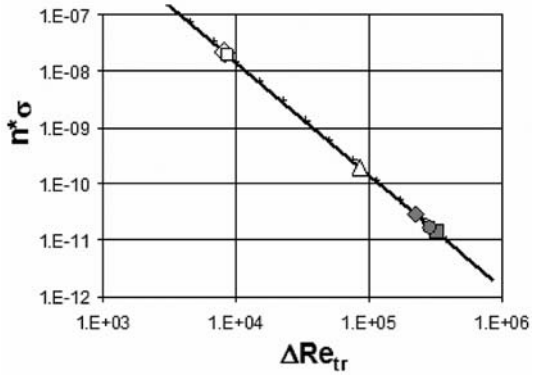

Fig. 5 Dimensionless spot production rate as function of transition length Reynolds number (symbols as in Fig.1; Eq. (11) - straight line; interpolation of results [15] - crosses)

Thus it is possible to divide the total record $(\tau_w(t_i))$ between the non-turbulent/laminar part (subscript L) and the turbulent one (subscript T)

$$(\tau_w(t_i)),\ i = 1, 2, \ldots n = 750000$$

$$(\tau_w(t_i))_L = (1 - I(t_i))\tau_w(t_i);\ (\tau_w(t_i))_L = I(t_i)\tau_w(t_i) \qquad (11)$$

Apparently, any kind of the statistical analysis of every record could be done as customary at every experimental set up and in each cross section x. The analyzed wall friction records (750 thousands samples) were made at the same boundary conditions as the measurements plotted in Fig. 1. Here the attention will be concerned with the effect of boundary conditions on the mean time of the laminar $(\Delta t)_L$ and turbulent $(\Delta t)_T$ events duration and on the distributions of the wall friction conditional means $(\tau_w)_L$ and $(\tau_w)_T$. The mean durations of the wall friction stay in non-turbulent condition $(\Delta t)_L$ and in turbulent condition $(\Delta t)_T$ are plotted in Fig. 6; right the results referring to the rough wall boundary layers and left the results referring to the smooth wall boundary layers. Laminar periods $(\Delta t)_L$ are of about two orders longer than the turbulent periods $(\Delta t)_T$ at the start of transition x_s. The opposite relations are at the transition completing. The courses are similar in smooth wall layers as in rough wall layers. Locations of maximum $(\Delta t)_L$ and minimum $(\Delta t)_T$ relate to the location of $\gamma = 0$. The course of growing and decreasing of the discussed durations proceed in the streamwise similarly. An apparent difference between the smooth wall layers and the rough ones is ascertained in the events durations that are roughly of order longer in the smooth wall configuration. This can be attributed to the effect of numerous flow disturbances generated by wakes of individual sand grains on rough surface however a definite physical explanation of this phenomenon is not available yet. The distributions of the conditional mean wall friction in the investigated boundary layers versus the displacement thickness Re-number are shown in Fig. 7 in the same way as in the preceding Fig. 6. Presented are the results of measurements in boundary layers under boundary conditions that differ only in sur-face property – smooth or rough. Distributions after Blasius solution (full line) and after Ludwieg and Tillmann formulae (dashed line; necessary substitute actual values of the shape factor and the momentum thickness Re-number) are also plotted in Fig. 7.

The non-turbulent/laminar means $(\Delta\tau_w)_L$ follow the Blasius distribution up to the location where the intermittency factor becomes zero value. Afterwards the values $(\Delta\tau_w)_L$ continue at about constant level in smooth wall layers or start to grow in rough wall layers. The increase continues little beyond the end of transition region $\gamma = 1$ and then the increase is possibly succeeded by the decrease (unfortunately measurements were closed too early – already just after reaching locations $\gamma \sim 1$). The mean wall friction $(\Delta\tau_w)_T$ during turbulent events diverges from the Blasius distribution sooner than $(\Delta\tau_w)_L$. It diverges about in the section where the displacement Re-number reaches value 200. Afterwards the values $(\Delta\tau_w)_T$ continue at about constant level in smooth wall layers or start to grow in rough wall layers up to the end of transition region. This development is finished at reaching the level relevant to the distribution after Ludwieg and Tillmann empirical formula [4] evaluated with the valid values of the shape factor and momentum thickness Re-number.

4. Conclusion

The spot occurrence is more numerous in rough wall transitional boundary layer (RWL) than in the smooth wall layer (SWL) at otherwise equal boundary conditions. Owing to this transition starts sooner and the area of transition region is shorter in RWL than in SWL.

The increase of the free stream turbulence (FST) level Iu, in the plane of boundary layer origin $x = 0$, amplifies the above-mentioned phenomena. The effect of FST length parameter *Le* on by-

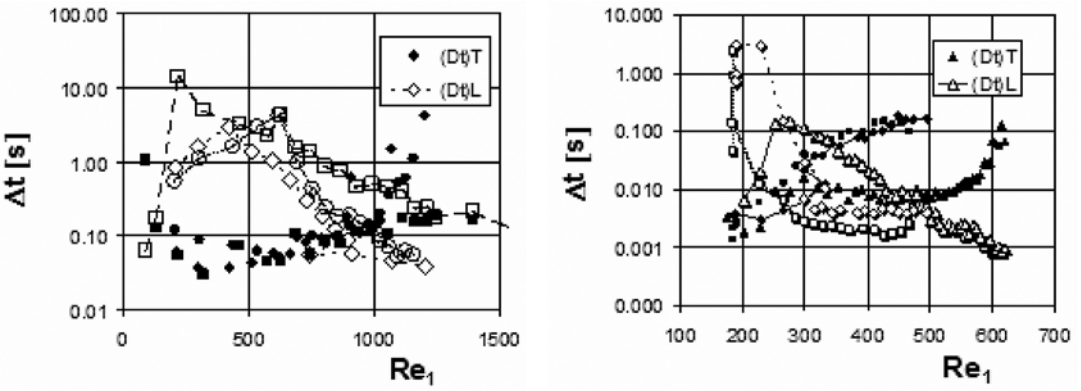

Fig. 6 The mean durations of the wall friction stay in non-turbulent condition $(\Delta t)_L$ and in turbulent condition $(\Delta t)_T$ (left smooth surface; right rough surface; symbols as in Fig.1)

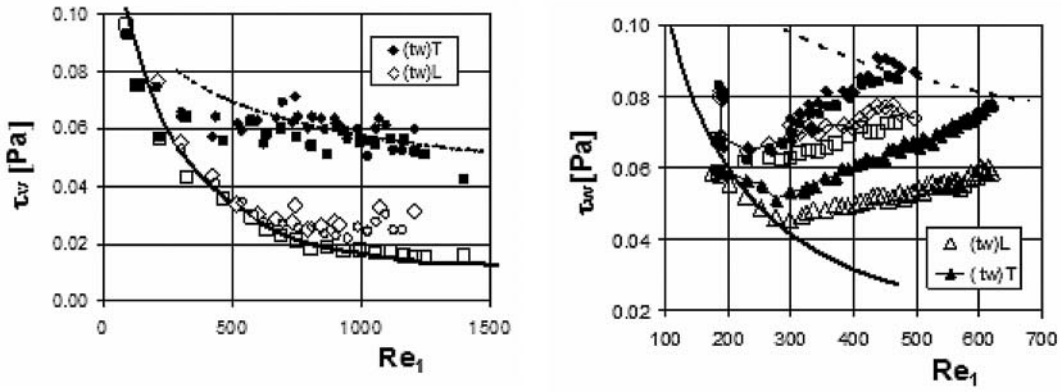

Fig. 7 Conditional mean wall frictions in smooth wall layer (left) and in rough wall layer (right) (Blasius solution – full line; Ludwieg and Tillmann distribution – dotted line)

pass transition is similar in both SWL and RWL. The smaller FST length parameter the faster turbulence decay occurs. Owing to this, intensity Iu in flow with larger *Le* exceeds the local intensity in flow with smaller *Le* in a given distance *x*, despite intensities are the same at $x = 0$. Methods and procedures of measurement, processing and analysis developed for investigations of smooth wall layers are usable also in rough wall layers however transformation of the initial CTA signal record into the record of the instantaneous wall friction is much more laborious.

Acknowledgement

The authors gratefully acknowledge financial support of the Grant Agency of the Czech Republic, project GAP101/12/1271 and as well as the project AVOZ20760514.

References

[1] JONAS, P.: On the Role of the Length Scale in the by-pass Transition. ZAMM – Z. angew. *Math. Mech.* 77 (1997) S1, S145-S146.

[2] HLADIK, O., JONAS, P., MAZUR, O., URUBA, V.: *Boundary Layer by-pass Transition by Joint Action of Surface Roughness and External Turbulence.* Proc. Experimental Fluid Mechanics Conf. (Eds. Vit, T. and Dancova, P.), TU of Liberec (2010), 192–208.

[3] SCHLICHTING, H., GERSTEN, K.: *Boundary-Layer Theory*. Springer, Berlin, 2000.

[4] LUDWIEG, H., TILLMANN, W.: Untersuchungen uber die Wandschubspannung in turbulenten Reibungsschichten. *Ing.-Archiv,* Gd. 17 (1949), 288-299, borrowed from [3].

[5] JONAS, P., MAZUR, O., Uruba, V.: On the Receptivity of the by-pass Transition to the Length Scale of the Outer Stream Turbulence. *Eur. J. Mech.* B 19 (2000), 707–722.

[6] JONA, P., MAZUR, O. and URUBA, V.: Statistical Characteristics of the Wall Friction in a Flat Plate Boundary Layer through by-pass Transition. ZAMM Z. Angew. *Math. Mech.* 79 (1999), S691–S692.
[7] ZHANG, D. H., CHEW, Y. T., WINOTO, S. H.: Investigation of Intermittency Measurement Methods for Transitional Boundary. *Exp. Thermal and Fluid Sci.,* 12 (1996), 433–443.
[8] HENDLEY, T. B., KEFFER, J. F.: Turbulent/non-turbulent Decision in an Intermittent Flow. *J. Fluid Mech.* 64 (1974), 625–644.
[9] ELSNER, W., WYSOCKI, M., DROBNIAK, S.: Determination of Production Rate of Turbulent Spots Using Wavelet Analysis. *Chemical and Process Engineering,* 27 (2006), 935–950.
[10] HLADIK, O., URUBA, V.: Analysis of Intermittent Signal, *Mechanical Engineering J.*, June 2009, ISSN 1335-2938, 69–70.
[11] JONAS, P., ELSNER, W., MAZUR, O., URUBA, V., WYSOCKI, M.: Turbulent Spots Detection During Boundary Layer by-pass Transition. *ERCOFTAC Bulletin* 80 (2009), 16–19.
[12] NARASIMHA, R., The Laminar-turbulent Transition Zone in the Boundary Layer. *Prog. Aerospace Sci.* 22 (1985), 29–80.
[13] EMMONS, H.: The Laminar-turbulent Transition in a Voundary Layer – Part 1, *J. Aeronaut. Sci.* 18, (1951), 490–498.
[14] JOHNSON, M. W., FASHIFAR, A.: Statistical Properties of Turbulent Bursts in Transitional Boundary Layers. Int. *J. Heat Fluid Flow* 15 (1994), 283–290.
[15] FRANSSON, J. H. M., MATSUBARA, M., ALFREDSSON, P.H., Transition Induced by Free-stream Turbulence. *J. Fluid Mech.* 527 (2005), 1–25.

Patrik Nemec – Milan Malcho – Martin Smitka – Jozef Matusov *

PERFORMANCE PARAMETERS OF A CLOSED LOOP THERMOSYPHON

Devices composed of output electronic components produce waste heat that has to be dissipated to the environment. Heat removal by means of forced convection air cooling is quite often insufficient and new alternatives for cooling of output electronic components are being looked for. One option is the use of a closed loop thermosyphon. Theclosed loop thermosyphonis a simple and reliabledevice providing heat transfer. The paper deals with the cooling of an output electronic component by means of this device. It describes a design and construction of the device to provide heat removal from the electronic component, measurement of dependences of performance parameters on waste performance of the electronic component and their verification by means of a mathematic calculation based on physical phenomena of boiling, condensation and heat transfer.

Keywords: *Closed loop thermosyphon, heat transfer, Fluorinert FC-72, mathematical model*

1. Introduction

Permanent development of electrotechnical devices aims to increase their performance, to efficiently use the space, to reduce their mass, to achieve higher efficiency and reliability as well as a higher technological level. Another trend in the development of electrotechnical components is miniaturization of dimensions which leads to the increase in local heat loading due to heat waste of electronic components. More intense heat production and its insufficient removal often cause deterioration of electronic system parameters and electronic components failures. To maintain suitable working conditions it is necessary to dissipate waste heat. From various cooling methods used in electronics the heat pipe seems to be one of highly efficient and reliable way of heat removal[1]. The closed loop thermosyphon works on the same principle as the standard gravitational heat pipe in which heat transfer occurs due to the flow of vapor and liquid phase of the working fluid between the evaporation and condensation sections of the heat pipe. The difference between them is in the way of the working fluid circulation. While in the standard gravitational heat pipe theworkingfluid flows between the evaporation and condensation sections in the same space, in the closed loop thermosyphon the working fluid flows in a closed loop between the evaporation and condensation sections. Due to the absence of interaction and reverse flow of vapor and liquid phase the closed loop thermosyphon features better ability to heat transfer between its evaporation and condensation sections than the standard gravitational heat pipe.

2. Construction of the closed loop thermosyphon

Main parts of the closed loop thermosyphon are:
- evaporator,
- condenser,
- pipe system to transport the working fluid and
- inlet and closing valves.

The evaporator (Fig. 1) enables on the base of a phase change (boiling) of the working fluid an intensive heat removal from its surface. It has to be constructed so that it will prevent the leakage of the working fluid, maintain pressure differences in all the walls and enable heat transfer from the electronic component into the working fluid as well as a suitable distribution of liquid and vapor phases of the working fluid. When choosing the material suitable for the construction of evaporator, it is necessary to pay attention to its thermokinetic characteristics. To provide a minimal temperature drop between a heat source and evaporator, the evaporator material must feature high thermal conductivity. To prevent escape of vapor, it should not be porous. The material should have high strength but, at the same time, it should be easily machineable and compatible with the working fluid [2]. Fig. 1 shows the closed loop thermosyphon from aluminum alloy designed with respect to the above requirements. The evaporator body is a plate with dimensions $116 \times 80 \times 30$ mm. To provide the working fluid circulation there are two12 mmopeningsdrilled horizontally on the plate and connected with nine 6 mm vertical connecting channels. They provide the transport of heated fluid vapor from the bottom to the top section of the evaporator. On the outer contact surface of the evaporator and electronic component there is a groove with a mounted temperature sensor.

The closed loop thermosyphon condenser (Fig. 2) is a soldering plate heat exchanger Alfa Laval. This choice was determined by the effort to achieve a compact construction of the cooler providing the working fluid cooling in the heat pipe at defined temperatures of the cooling water and being able to withstand high

* **Patrik Nemec, Milan Malcho, Martin Smitka, Jozef Matusov**
Department of Power Engineering, Faculty of Mechanical Engineering, University of Zilina, Slovakia, E-mail: patrik.nemec@fstroj.uniza.sk,

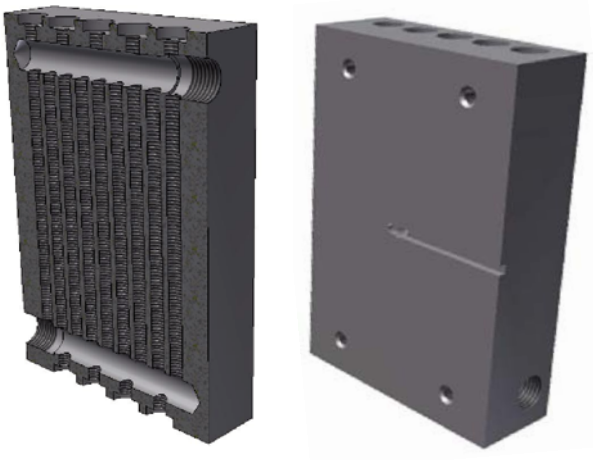

Fig. 1 Loop thermosyphon evaporator

pressures. Soldering plate heat exchangers comprise a stack of shaped plates pressed of stainless steel. Corrugation of plates ensures more intense heat transfer and at the same time increases their rigidity.

Fig. 2 Loop thermosyphon condenser

Heat exchanger plates are arranged so that there are optimal channels among them into which heat carrying fluid is introduced through openings in the corners of the plates. Each plate is flown by the primary fluid from one side and by the secondary fluid from another side with simultaneous presence of heat transfer. A copper connector connects the plates not only along their circumference but also in all connecting places of neighboring plates. Brazed heat exchangers are therefore able to withstand high temperatures (up to 225 °C) and pressures (up to 49 bars) and have high efficiency of heat transfer even at low logarithmic mean temperature difference. The transport section of the closed loop thermosyphon provides the circulation of vapor and liquid phases between the evaporator and condenser of the heat pipe. The whole transport section consists of 10 mm copper connecting tubes. Transient glass tubes were mounted on the evaporation and condensation sides of the transport section of the heat pipe to visualize and check the working fluid flow. All connecting transient points of the whole heat pipe system are vacuum-tight. The intake and closing valves are located on the top of the evaporation transport section.

3. Working fluid

The first criterion for a design of suitable working fluid is the range or operating temperature. As there can be more working fluids within the range of suitable operating temperatures, it is, therefore, necessary to observe and compare their further thermophysical characteristics when determining the most suitable one. The main requirements for working fluid characteristics are compatibility with the heat pipe material, good temperature stability, suitable vapor pressure, large latent heat of evaporation, high thermal conductivity, low viscosity of fluid and vapor, acceptable point of freezing and solidification from the point of cooling operation.

The choice of working fluid has also to be done on the basis of thermodynamic considerations concerning various limitations of heat transfer in heat pipes (viscose, sonic, capillary limits and limits of bubble boiling). Vapor pressure within the range of operating temperatures has to be sufficiently large to avoid high velocity of vapor which may cause instability of heat flows. The working fluid must feature high latent heat of evaporation which will enable to transfer the highest possible amount of heat with the least fluid flow provided the low pressure difference in the heat pipe is maintained. Thermal conductivity of the working fluid should be, if possible, high to minimize radial temperature gradient and decrease possibilities of film boiling on the surface walls. The resistance to the fluid flow is minimized through the choice of fluid with low values of viscosity of fluid and vapor phases [3]. In compliance with

Physical characteristics of working fluid FC 72 at temperature 20 °C [4]. Table 1

FC 72 CHARACTERISTICS		
Relative molecular mass	-	338
Estimatedcritical temperature	K	449
Estimatedcritical pressure	MPa	1.83
Vapor pressure	kPa	30.9
Latent heat of evaporation(at nor. boiling point)	$kJ.kg^{-1}$	88
Density of fluid	$kg.m^{-3}$	1680
Kinematic viscosity	$m2.s^{-1}$	$0.38.10^{-6}$
Specific heat of fluid	$Jkg^{-1}K^{-1}$	1100J
Thermal conductivity of fluid	$Wm^{-1}K^{-1}$	0.057
Coefficient of expansion	K^{-1}	0.00156
Surface tension	$N.m^{-1}$	10^{-2}
Dielectric strength	kV	38
Dielectric constant	-	1.75

the above mentioned conditions Fluorinert FC 72 was chosen as the working fluid for experimental research of the heat pipe, due to its compatibility with most metals, low boiling temperature (56 °C) and solidification (-90 °C) and, first of all, due to its excellent dielectric characteristics. Physical characteristics of Fluorinert FC 72 are presented in Table 1.

4. Measurement of loop thermosyphon performance parameters

To determine the heat pipe performance parameters a measuring device was designed – its scheme can be seen in Fig. 3. Due to possible applications of the heat pipe system serving,for example, also heat transfer in a region with the temperature of 50 °C, measurements with the maximum input temperature of the cooling fluid up to 50 °C were made. The measurement was performed at the increasing waste heat performance of the electronic element from 20 to 370 W. The electronic element fixed in a standard way to the evaporation section of the heat pipe was connected to the unidirectional current source HEWLET PACKARD 6575A, DC POWER SUPLY 0–120 V/ 0–18.5 A. The maximum admissible electric current that can pass through the electronic component was 20 A at the maximum voltage 20 V and the highest admissible temperature on the contact surface was 100 °C. Supplying the required heat to the evaporation section of the heat pipe, the working fluid is heated to the boiling point and starts to evaporate. Vapors of the working fluid flow along the tubes of the evaporation section of the heat pipe to its condensation section which is formed by a plate heat exchanger. Vapors of the working fluid condense on the cooling surface of the heat exchanger plates connected to the cooling circulation with a thermostat. Due to gravity the liquid phase of the working fluid flows back to the evaporator of the heat pipe.

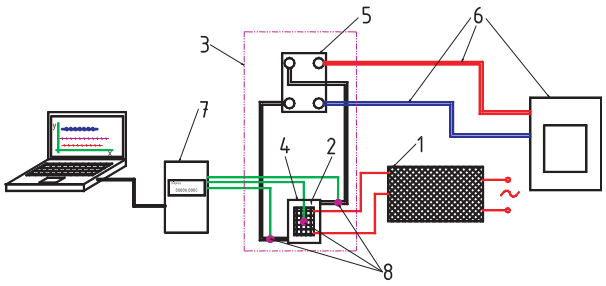

Fig. 3 Scheme of measurement device connection
1- source of electric voltage and power, 2 – testing electronic component, 3 –closed loop thermosyphon, 4 –evaporator, 5 - condenser, 6 –cooling circuit with thermostat, 7 – measurement centre, 8 – temperature sensors (thermocouples)

Ni-CrNi thermocouples reading surface temperatures are connected to the evaporation and condensation sections of the closed loop thermosyphon and to the connecting surface of the electronic component and evaporator. The temperatures are recorded into a PC by means of software AMR32in the measurement centre. Figure4 shows the closed loop thermosyphon connected to the measurement devices.

Fig. 4 Closed loop thermosyphon

Performance of the electronic component was gradually increased in five minute intervals by 40 W. To measure the heat performance more than 40 W,the time interval was extended to 31 minutes due to the recorded instability. Time intervals were not chosen randomly; they were determined from previous experiments and observation of the time interval of the stabilization of the measured closed loop thermosyphon. Results gathered from the measurement are shown in Fig. 5.

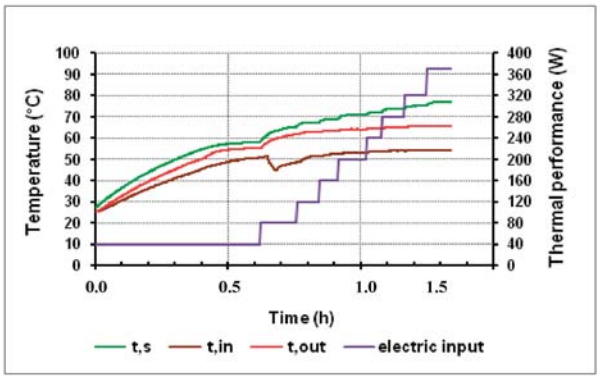

Fig. 5 Temperature dependence in the loop thermosyphon with cooling circulation 50 °C on performance of the electronic component

Fig. 5 shows the course of wet vapor temperature of the working fluid leaving the evaporator tout, of temperatures of the condensed working fluid entering the evaporator tin and temperatures on the

contact surface of the evaporator with the electronic component tsdependent mainly on the heat performance of the electronic component. At 0.64 hoursthe temperature of condensed working fluid entering the evaporator drops from 50.6 °C to 45.4 °C. This drop was caused by more intense bubble formation in boiling and pushing colder working fluid from the plate exchanger into the evaporator. As there was no further drop of the working fluid input temperature during the measurement, the operation of the closed loop thermosyphon was stabilized. Results gathered from the measurement can be used for the creation and comparison of a mathematical model for the calculation of performance parameters of the closed loop thermosyphon with an appropriate working fluid charge.

5. Mathematical model for determination of performance parameters of the closed loop thermosyphon

The closed loop thermosyphon has an evaporation section separated from the condensation section, i.e., it has a separate section for a vapor and liquid phase of the working fluid. In the evaporation section of the closed loop thermosyphon the condensate is heated up to the boiling temperature of the working fluid. Boiling temperature is given by instantaneous absolute pressure in the circuit of the closed loop thermosyphon. It can be seen from the experiments that at the temperatures up to approx. 80 °C the evaporation or bubble boiling of the working fluid FC 72 takes place. The mathematical model of performance parameters of the closed loop thermosyphon was created on the basis of criterion equations (1a) and (1b) just for the bubble boiling [5].

$$Nu_B = 0.0625 \,.\, Re_B^{0.5} \,.\, Pr_K^{0.333} \quad \text{pre } 10^{-5} \leq Re \leq 10^{-2} \quad (1a)$$

$$Nu_B = 0.125 \,.\, Re_B^{0.65} \,.\, Pr_K^{0.333} \quad \text{pre } 10^{-2} \leq Re \leq 10^{4} \quad (1b)$$

The Prandtl number is determined from relation (2)

$$Pr = \frac{v_l}{a} \quad (2),$$

where a is thermal conductivity

$$a = \frac{\lambda_l}{(\rho_l \cdot c_p)} \quad (3).$$

Reynolds number for boiling is

$$Re = \frac{q \cdot B}{l_v \cdot \rho_v \cdot v_l} \quad (4),$$

where B is the critical average of vapor bubble and q is the density of thermal fluid flow,

$$B = \frac{c_p \cdot \rho_l \cdot \sigma \cdot T_v}{(l_v \cdot \rho_v)^2} \quad (5),$$

$$q = \frac{p_{el}}{S} \quad (6)$$

From relation (1a) or (1b) the Nusselt criterion Nu_B is determined and substituting relation (7), theheat transfer coefficient a is expressed

$$Nu_B = \frac{\alpha \cdot B}{\lambda_l} \quad (7)$$

The temperature on the contact area of the fluid and inner area of the evaporator chambers Ts_v is calculated according to relation (8)

$$T_{sv} = \frac{(q + \alpha \cdot T_v)}{\alpha} \quad (8)$$

The temperature on the contact area of the electronic component and the outer area of the evaporator of the closed loop thermosyph Ts is calculated from relation (9) that was derived from relations for heat conduction and transfer (10) and (11)

$$T_s = \left(\frac{q \cdot \delta}{\lambda_D}\right) + T_{sv} \quad (9)$$

$$q = \lambda D \cdot \frac{T_s - T_{sv}}{\delta} \quad (10)$$

$$q = \alpha \cdot (T_{sv} - T_v) \quad (11) \text{ [6]}$$

Basic physical characteristics of FC 72 in dependence on temperature are given by the manufacturer in tables or analytical form from which it is possible to determine the required variables in dependence on temperature

$$c_p = 1014 + 1.554 \,.\, (t, °C) \quad (12)$$

$$\lambda_l = 0.06 - 0.00011 \,.\, (t, °C) \quad (13)$$

$$\rho_t = 1740 - 2.61 \,.\, (t, °C) \quad (14)$$

$$p_v = 10^{\left(9.729 - \frac{1562}{(T, °K)}\right)} \quad (15) \text{ [4].}$$

According to the above mentioned relations the mathematical model was created and for the purpose of comparison the values of temperature tsfor the closed loop thermosyphon with the temperature of the cooling circulation in the condenser 50 °C were

Comparison of calculated and measured temperature t_s of the closed loop thermosyphon in dependence on temperature t_{out} — Table 2

P_{el} [W]	t_{out} (measured) [°C]	t_s (measured) [°C]	t_s (calculated) [°C]
40	30	33.71	37.66
40	40	44.39	47.23
40	50	54.63	56.85
80	60	63.5	68.46
320	65	74.37	80.5

calculated. The calculation started from the condition $t_v = t_{out}$ (evaporation temperature of the evaporating working fluid FC 72). Table 2 and Fig. 6 show comparison of calculated and measured values of temperature tsof the closed loop thermosyphon in dependence on the measured evaporation temperature of the working fluid FC 72 tout in a range from30 °C to 65 °C.

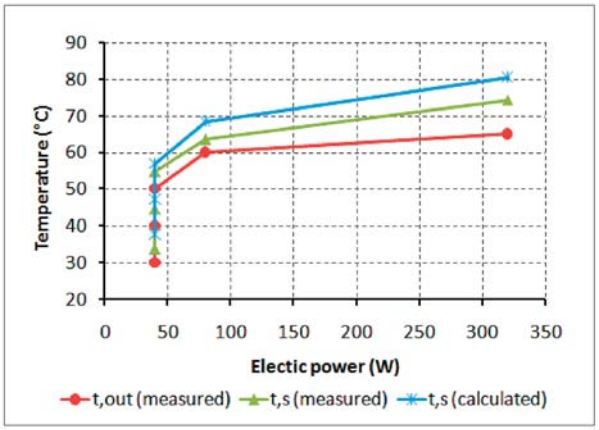

Fig. 6 Comparison of calculated and measured temperature loop thermosyphon evaporator t_s in dependence on temperature t_{out}

Fig. 6 shows calculated and measured temperatures tsof the heat pipe in dependence on temperature tout. It is obvious from the courses of temperatures that the measured values differ from the calculated ones only by approx. 3 to 6 °C. This closeness of the results approves the correct functionality and technological procedure of the heat pipe prototype as well as the option to use the simplified mathematical model for dimensioning of cooler with heat pipes for similar electronic components or systems.

6. Conclusion

The objective of experiment was to design and construct a prototype of the closed loop thermosyphone and verify its functionality at the cooling of electronic component used in real applications at the highest admissible temperature on the contact area with the cooler 100 °C and maximum admissible voltage and current 20 V and 20 A. Another objective of activities also was to show on a simple mathematical model the potential for the cooling of the heat pipe system and compare the resultant values of calculated and measured temperatures on the contact area of the cooled electronic component. According to the experimental measurements and calculations the closed loop thermosyphon cooling proved its high efficiency, which can be also seen at the full performance of the electronic component and also as the highest temperature of the cooling water 50 °C used to cool the evaporating working fluid in the condenser. The temperature on the contact area of the electronic component with the heat pipe evaporator was always below 80 °C. This experiment approves the cooling quality of the closed loop thermosyphon and justification of its use for the cooling of high efficiency electronic components and systems generating huge thermal flows of waste heat. The use of heat pipes for the cooling of output electronics, mainly electronic semiconductor elements, offers, together with reduced requirements for quantity of constructional material and saved space, also better cooling performance and improved cooling in the area of higher waste heat output above 100 W.

Acknowledgement

This paper was written within the framework of the project APVV 0577-10.

References

[1] HARTENSTINE, J., BONNER III, R., MONTGOMERY, J., SEMENIC, T.: *Loop ThermosyphonDesign for Cooling of Large Area, High Heat Flux Sources.* Proc. of IPACK 2007, Vancouver, CANADA

[2] RUPPERSBERG, J. C., DOBSON, R. T.:Flow and Heat Transfer in Closed Loop Thermosyphon – Part II: Experimental Simulation. *J. of Energy in Southern Africa,* vol. 18, No. 3, 2007

[3] ANDREWS. J., AKBARZADEH. A., SAUCIUC. I.: *Heat Pipe Technology: Theory, Applications and Prospects*. Melbourne: PERGAMON, 1996. ISBN 0 08 042842 8

[4] 3M Fluorinert™ Electronic Liquid FC-72 product information, Accessible at: http://multimedia.3m.com/mws/mediawebserver?mwsId=66666UF6EVsSyXTtnxTE5XF6EVtQEVs6EVs6EVs6E666666–&fn=prodinfo_FC72.pdf

[5] REAY, D., KEW, P.: *Heat Pipes-Theory, Design and Applications.* Burlington: Elsevier, 2006.ISBN–13: 978-0-7506-6754-8

[6] SAZIMA, M.: *Sdileni tepla[Heat Transfer],* Prague: SNTL, 1993. ISBN 80-03-00675-9.

Robert Olsiak – Branislav Knizat – Marek Mlkvik *

INVESTIGATION OF HIGH SPEED CAVITATION FLOWS

The paper presents an investigation of cavitating flow behind a micro-orifice. Experiments were performed with a device making visualization of a cavitation cloud possible. Two micro-orifices of the sizes 0.58 mm and 0.35 mm were tested at different cavitation numbers and at different flow rates. Parameters of the cavitation cloud collapse on a smooth surface were found. The experimental device, experiment methodology and some results are presented. Results of visualization are compared with CFD simulations.

Keywords: *Micro-orifice, cavitation cloud, visualization, Lichtarowicz cell*

1. Introduction

High speed cavitation flows when a cavitation cloud collapses due to the high flow speed far from a point of its origin occur in many hydraulic devices. Such devices usually contain sealing gaps or openings and work with high pressure gradients of liquid. The liquid flows through such gaps at relatively high velocities (tens or hundreds of m/s). The consequence of the increased flow speed is a local pressure drop causing a cavitation phenomenon. The cavitation cloud then collapses away in a high pressure region and if it is impinging on a solid wall a very intensive damage is possible. There are also some other applications where the erosive effect has a positive response and is intensified. We can mention cutting of materials, non-chemical etching of surfaces, peening of metal surfaces, etc. The aim of our investigation is the research of high-speed cavitation flows behind micro-orifices. Very important part of the research is a visualization of the cavitation cloud requiring special methods of illumination as well as data recording. Obtained results are compared with CFD simulations.

2. High speed cavitation flows in micro-orifices

Intensity of cavitation depends on the cavitation number. The cavitation number σ for an orifice is defined as follows:

$$\sigma = \frac{P_2 - p_v}{\frac{v_2^2}{2}\rho} \quad (-) \tag{1}$$

where p_2 – downstream pressure, p_v – vapor pressure, v_2 – the output velocity, ρ – density.

For the jet holds the Bernoulli's equation in a form (if a velocity v_1 is neglected with respect to the velocity v_2):

$$\frac{p_1 - p_2}{\rho} = C_v^2 \frac{v_2^2}{2} \quad (\text{J/kg}) \tag{2}$$

After combining equations (1) a (2) we obtain:

$$\frac{1}{\sigma} = \frac{1}{C_v^2}\frac{p_1 - p_2}{p_2 - p_v} \quad (-) \tag{3}$$

With respect to the fact that the velocity coefficient C_v is constant, we obtained a linear relation between the parameter σ^{-1} and the parameter $\frac{p_1 - p_2}{p_2 - p_v}$. This relation – formula (3) holds only in a cavitation regime of flow.

3. Test rig

A base part of the test rig is so called Lichtarowicz cell (modified in this case). The cell is designed for the research of flow of a cavitation cloud and for the research of its erosive effects. The cloud impinges on a sample placed in a fixed distance from the jet. The cell has a circular frame; the jet opening and the sample are lying in the same line. The basic schema of the experimental set up for cavitation flow visualization is presented in Fig. 1. Experimental configuration of visualization parts is integrated from the following major components and subsystems. Part No. 1 is a special hydraulic chamber. Cavitation cloud near a back side of a micro orifice is observed via visualization method. Most sensors for measurements of hydraulic parameters are installed in a cell across the construction walls. Part No. 2 is a high speed digital video camera. It is the monochromatic digital camera RedLake Y3 based on CMOS video chip with very low inter frame time (less than 100 ns in a double rate mode). The digital camera has an integrated 4 GB video memory and digital communication links USB 2.0 or Giga Ethernet. Part No. 3 is DAQ, a vision and control system. The system is integrated at the Windows XP Workstation platform. DAQ and a control I/O card used in this system for functionality expansion are from the National Instruments product range. The DAQ I/O card is used for measurements of hydraulic parameters: inlet pressure, pressure in a test chamber, test liquid temperature,

* **Robert Olsiak, Branislav Knizat, Marek Mlkvik**
Faculty of Mechanical Engineering, STU Bratislava, Slovakia, E-mail: robert.olsiak@stuba.sk

mass flow, etc. Software Motion Studio (Motion Studio Pro for selected analysis) is used for vision applications. Part No. 4 is the NANOLITE flash lamp with a very low flash duration, typically 8 ns. The lamp is a source of a cold white light with an extreme intensity. Part No. 5 is the MINISTROBOKIN flash driver which is used with the NANOLITE flash lamp. The lamp is a high repetition (up to 20 kHz) high voltage pulse generator, synchronized and triggered via analog TTL technology. The operation mode is controlled by the DAQ system. A subsystem No. 6 is a pressurized air circuit. This circuit is applied for blowing the plasma torch incipient at NANOLITE flash lamp electrodes. However, it is a standard pneumatic system, but the application is unconventional. The test rig is also described in [1].

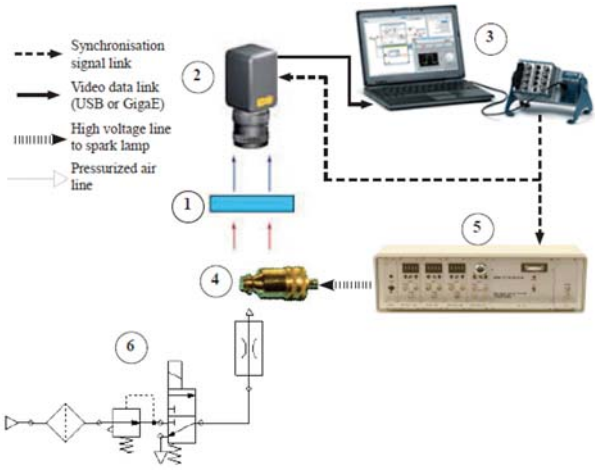

Fig. 1 Schema of the experimental test rig

3.1. Video recording and illumination

Acquired data from the described experimental system have two marginal characteristics: numerical data – acquired values from analog physical signals (e.g. pressure, temperature, mass flow) and calculated values (e. g. cavitation number) which are stored as a data file. Video data from the experiments are stored in the digital camera video memory 2 in a first step, in a second step the data are transmitted to the Vision software via communication link (USB 2.0 as standard) and stored as a digital video file (HDD of DAQ and Vision system) 3. The format of the video file is optional, but saving as *.RAW format is necessary for an advanced post-analysis. Via decoding the stored *.RAW video file the set of the digital pictures is available for a detailed analysis and advanced measurements, Fig. 2.

In Fig. 2 the region of interest (ROI) is defined – a space between the tested orifice back side and a face side of the specimen (see flow direction in Fig. 2, too). The intensity of light and shape contours of solid bodies in the defined region is strictly required for video data analysis, especially for a quantitative analysis algorithm. The shape of contours of the solid bodies in the ROI is dependent on the used optical component and the vision system settings. Lighting conditions are strictly dependent on the quality and stability of the illuminate apparatus (light source). The flash lamp is used as the illuminating equipment. The flash lamp is improved up to the optimum efficiency offering the shortest possible flash duration. Due to the extremely high luminous density of the point shaped spark the lamp has a sufficiently high flash energy. Some other applications areas of the nanosecond flash illumination for the photographic analysis of extremely fast events are, e.g., in shock wave tubes, hypersonic wind tunnels, droplet research (PIV), bubble formation, optical stress experiments, shadow and interferometer photography. The simple spark is produced by the instantaneous discharge of electric energy, stored in a capacitor, through a system of HVE and GE electrodes Fig. 3. The most important characteristics of the flash light source are the light energy, flash duration, form of the luminous spark plasma, and possibly its spectral composition. The latter is mainly determined by the atmosphere in which the discharge takes place. A simple air spark consists of almost white light. For the most applications of flow visualization it is desirable to have a spark volume as small as possible, e.g., a point-shaped light source. In the arrangement in Fig. 3, the luminous spot appears small to an observer in the direction of the object field, since the spark is forced to discharge through the ceramic capillary tube. The flash time is determined by the inductivity of the discharge circuit; this must be kept as low as possible. The illumination system is described in detail for example in [2].

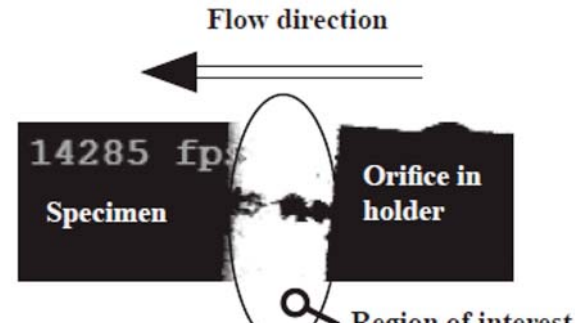

Fig. 2 Sample image isolated from experimental video sequence acquired @ 14285 frames per second

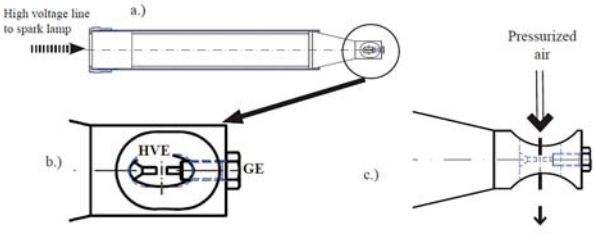

Fig. 3 a) Construction of high voltage spark lamp. b) The high voltage and ground electrodes. c) Stabilization of plasma properties by the pressurized air

3.2 Micro-orifices

The experiment was carried out with two different micro-orifices $d = 0.35$ a $d = 0.58$ mm.

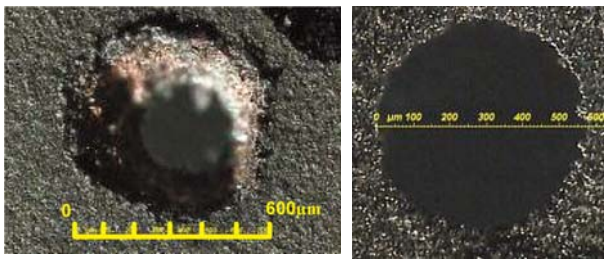

a *b*

Fig. 4 Micro-orifice 0.350 mm (left) and 0.580 mm (right)

In Fig. 4 is a photo of both 0.35 mm and 0.580 mm micro-orifices. Micro-orifices were fixed in the holder by sticking. The material of the micro-orifices is hard alloy and they were manufactured in UTM SjF STU in Bratislava.

4. Numerical simulation of cavitating flows

4.1 Computational grid

Computational domain for the simulation is created as 2-Dimensional and axissymetric. This simplification allows us to use square grid elements. This approach allows us strongly reduce the computation time. Also the quality the grid elements is much more better as in the 3-Dimensional version of the grid, which produces the elements, where the high skew of the elements is often a problem. The length of the element's corner is set to 1/10 of the orifice diameter. This size is set according to our previous experiences with the simulation of the cavitating flows.

The boundary conditions are set according to Fig. 5.

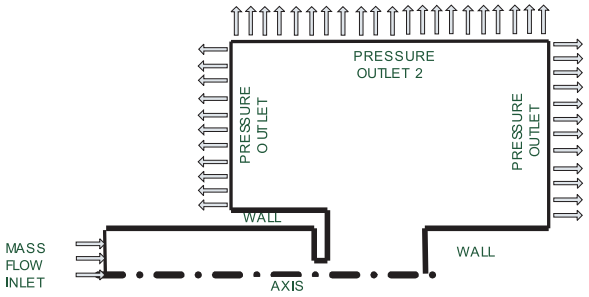

Fig. 5 Used 2-D axisymmetric computational domain with boundary types

4.2 Solution setup

The solution of the cavitation jet is set as a transient one. According to the very high characteristic speed of the cavitation jets, the time step of the solution is set 10^{-5} s. Very important for a CFD simulation is to set correct material properties. In this case, the properties of air and water vapor must be assumed as compressible. Other simulations parameters can be found in Tab. 1. As can be seen in [3], the well tuned numerical model can successfully solve a problem of the cavitating flow.

Solution Setup Tab. 1

Computational Domain and The Grid	2D, axisymetric, structural grid(quads), element length scale is 10% of the orifice radius
Solution Type	Transient solution (time step $\sim 10^{-5}$ s)
Model of Turbulence	$k - \varepsilon$
Solver type	SIMPLE
Multiphase model	Mixture, Eulerian
Model of the phase change (cavitation model)	Singhal Model, Model Zwart-Gerber
Liquid phase properties	incompressible, properties according to the normal conditions (20 °C, 1 bar)
Gases properties	Compressible- state equation of the ideal gas,

5. Results of investigation

5.1 Results of visualisation

The experiments were carried out with two micro-orifices in a wide range of flow rates, pressures and cavitation numbers. In Fig. 6 is a typical structure of a cavitating cloud impinging on a solid wall.

As it is depicted in Fig. 6, the cloud flows from the opening of a diameter d and impinges on a sample at a distance *x*. The cloud collapses on the sample and the region of collapse is denoted *D*. The structure of the cloud is not stable; it is periodically changing,

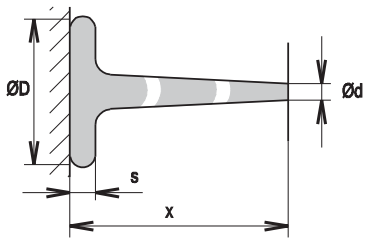

Fig. 6 Structure of a jet impinging on a solid wall

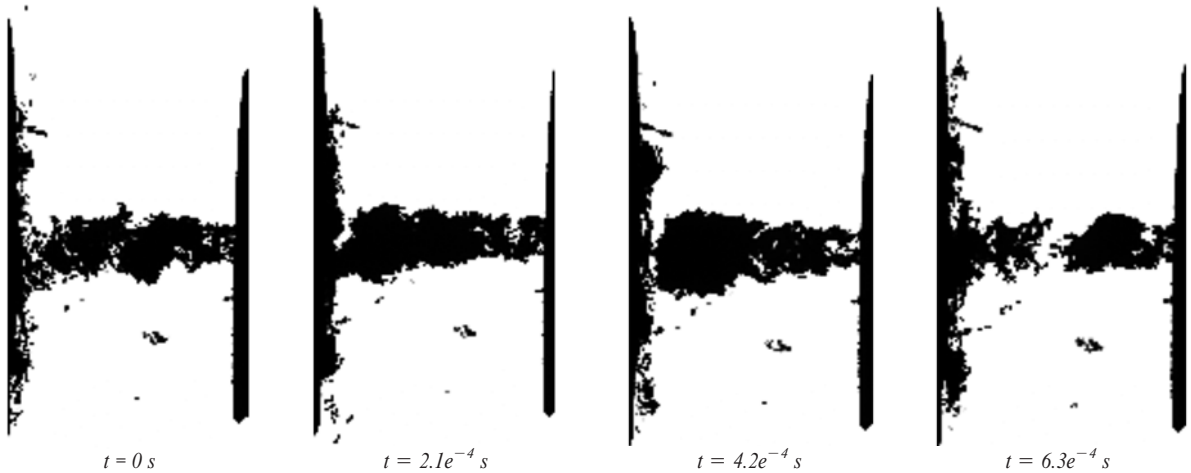

Fig. 7 Visualization of flow. Orifice diameter 0.58 mm, pressure $p_1 = 17$ bar

which is noticeable especially at higher values of a cavitation number. In Fig. 7 is depicted a sequence of shots of flow for the orifice with a diameter $d = 0.580$ mm.

From the figure it is clear that the stream is periodically changing. In Fig. 8 is depicted a typical shape and structure of the jet in dependence on the cavitation number. An opening with a diameter $d = 0.580$ mm and a distance $x = 5.0$ mm between the jet and the sample is selected. At high cavitation numbers the cloud collapses even before it reaches the sample. With the decreasing of σ the intensity of a cloud grows. At the same time the diameter D (Fig. 6) of the region on which the cloud collapses is increasing.

In Fig. 9 are depicted nondimensional geometrical parameters of a cavitating flow for both micro-orifices. It is a nondimensional cavitation cloud thickness s/d and a nondimensional diameter of a collapse D/d. The curves are presented in dependence on the cavitation number σ. With a decreased value of σ the intensity of cavitation grows and the thickness and diameter of a collapsing cloud also grow. The distance between the jet and sample has also an effect. For example, at a distance $x = 5.0$ mm at the greatest values of cavitation number ($\sigma = 0.28$) the cloud doesn't reach the sample. That is the reason why the cavitation effects (especially erosion) are strongly dependent on the cavitation number. The experiments show that the magnitude of this number influences the region of a cavitation cloud collapse.

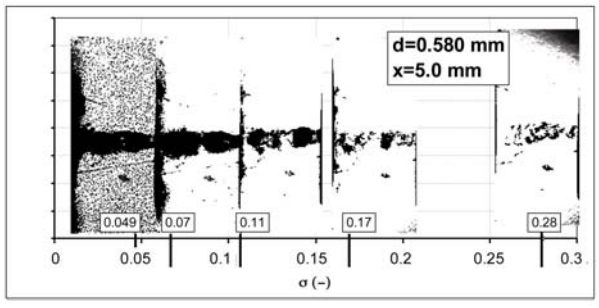

Fig. 8 Structure of a jet in dependence on the cavitation number

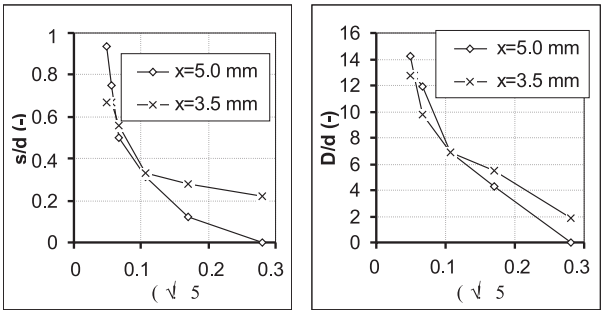

Fig. 9 Relative thickness (left) and relative diameter (right) of a cavitation cloud for the orifice 0.580 mm

5.2 Comparison of experiments and CFD calculations

As shown in Fig. 10, both of the used cavitation models are able to compute the pressure loss with a good accuracy. It can be observed that the computed inlet pressure is in both cases higher than the inlet pressure measured. The results obtained with the Singhal cavitation model are more accurate, especially in the case of higher cavitation numbers. The Singhal cavitation model is then more useful in the case of flow where the cavitation process is in its early stages (cavitation inception).

The visualized structure of the cavitation cloud can be compared with simulation results. Computed distribution of the vapor phase can be seen in Figs. 11 and 12. Both of the cavitation models give results which are comparable with the experimental data. Again, the Singhal cavitation model is more accurate even in higher cavitation numbers.

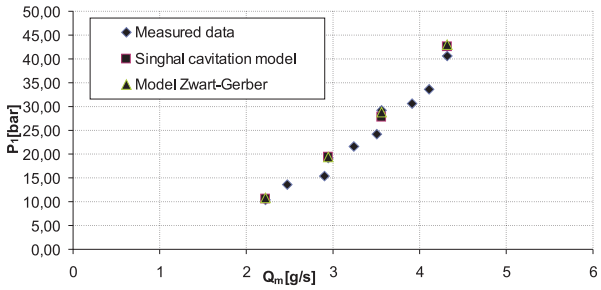

Fig. 10 Comparison of the pressure loss in the orifice (the simulation and the experiment)

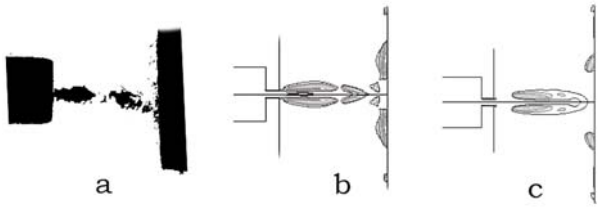

Fig. 11 Comparison of the spatial distribution of vapor for σ = 0.38 (a – experiment, b – Singhal cavitation model, c – Zwart-Gerber cavitation model)

The Zwart-Gerber cavitation model can be assumed as accurate enough only in lower cavitation numbers when cavitation is fully developed.

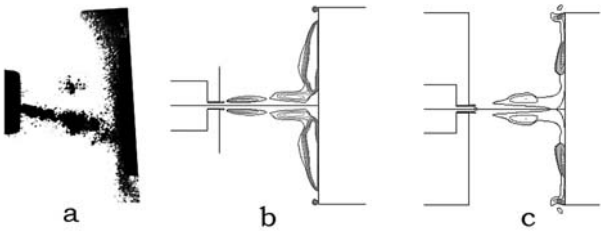

Fig. 12 Comparison of the spatial distribution of vapor for σ = 0.32 (a – experiment, b – Singhal cavitation model, c – Zwart-Gerber cavitation model)

6. Conclusion

In the paper the visualizations of flow of a cavitation cloud behind the micro-orifice are presented. The shots of a collapsing cloud on a sample for two micro-orifices of different sizes are also presented. Generally it may be stated that the intensity of the cloud which is in contact with the sample depends on a cavitation number, micro-orifice size, and distance. During the experiments speeds up to 100 m/s were reached behind the micro-orifice. This fact requests special approach to images acquisition and primarily to the illumination of the cavitating micro-jet. Obtained results of visualization are compared with the results of CFD simulations. A good agreement between simulations and visualizations can be seen from the comparisons. However, it is necessary to choose a suitable cavitation model in dependence on the magnitude of the cavitation number. Also the quality of the computational grid has strong effect on the simulation results. In presented case, the square elements were used to generate the 2-D axissymetric grid.

Acknowledgement

This work was supported by the Scientific Grant Agency VEGA under contract number 1/0215/11.

References

[1] OLSIAK, R., KNIZAT, B., MLKVIK, M.: *Visualization of Cavitating Micro Jets.* Experimental Fluid Mechanics 2011, Proc. of the Intern. Conference, Jicin, 2011.

[2] MLKVIK, M., OLSIAK, R., KNIZAT, B.: *Vizualization of the Cavitating Jet Using Flashlamp For Illumination.* Experimental Fluid Mechanics 2011, Proc. of the Intern. Conference, Jicin, 2011.

[3] KOZUBKOVA, M.: *Matematicke modely kavitace a hydraulickeho razu [Mathematical Models of Cavitation and Hydraulic Impact].* VSB- Technical University Ostrava, 2009, ISBN 978-80-248-2043.

Abeer Mukhtar – Humera Golandaz – Young Hwan Kim *

EFFECTS OF LEADING EDGE PROTUBERANCES ON THE AERODYNAMIC PERFORMANCE OF 2D CAMBERED AIRFOIL

The pressure and lift coefficients were measured for airfoils with leading edge protuberances in a subsonic wind tunnel and compared with the performance of a baseline NACA 4415 airfoil with a straight leading edge. These protuberances of 2D airfoil mimic the leading edge configuration of the flippers of a humpback whale. Wavelengths were varied from 25% to 50% of the chord length whilst amplitude was varied from 5% to 12% of the chord length of the baseline. Surface flow visualisation using kaolin was also performed to further analyze the flow patterns and surface swirls and vortices were observed. The presence of protuberances enhanced the stall characteristics of the baseline and low amplitude protuberances exhibited the maximum lift coefficient. However, at low angles of attack, the performance of the modified airfoils is similar to that of the baseline.

Nomenclature

c mean chord length, cm
s span, cm
Re Reynolds number
Cl lift coefficient
Cp pressure coefficient
α angle of attack, degrees

1. Introduction

Nature benefits us with its ecosystem services and natural systems. Thus one of the inspirations from nature is in the field of biomimetics or bio mimicry. Adaptations from the nature discussed are the tubercles found on the leading edge of humpback whale flippers. These tubercles help them to glide easily through the ocean. This form of adaptation for airfoils has resulted in an increase in their performance. According to Hansen and Kelso et al [1] an airfoil model with such leading edge tubercles achieved higher lift coefficient and large stall angle with minimum drag when compared to the conventional smooth leading edge model.

Experiments carried out by Johari et al [2] and Watts and Fish [3] also showed increase in the lift and a reduction in the drag on the wing with leading edge tubercles. However, all studies by [1], [2] and [3] concluded that there was no significant improvement in the performance in the airfoils at low angles of attack with leading edge tubercles. The previous studies carried out as mentioned above, were conducted for symmetric airfoils and in water. Thus, the primary objective of this study is to investigate the pressure distribution resulting from the leading edge tubercles on 2D NACA 4415 cambered airfoil models with varying amplitudes and wavelengths in air, along with the measurement of the lift force using a three component balance. Flow visualization using a mixture of kerosene and china clay was also performed to further analyze the flow patterns.

2. Experimental technique

For the purpose of the study, four 2D models were manufactured from MDF wood, which included the normal NACA4415 airfoil or the baseline airfoil having the conventional straight leading edge and three other modifications of the baseline airfoil having leading edge sinusoidal protuberances. These three models had the following varying amplitude and wavelength:

Model specifications Tab. 1

Wing configuration number	Wavelength	Amplitude
1	0.25c	0.12c
2	0.50c	0.05c
3	0.50c	0.12c with flat trough

All the experimental models, including the baseline, had an equivalent span of 30 cm and a chord length of 20 cm. Pressure taps were drilled perpendicular to the local chord position along the upper and lower surfaces of the models. The pressure was transferred to the measurement systems through the help of internally fixed copper and plastic tubes.

* **Abeer Mukhtar, Humera Golandaz, Young Hwan Kim**
Emirates Aviation College, Dubai, United Arab Emirates, E-mai: aby_51@hotmail.com

For measuring the lift force, the surface drilled holes, were filled and the surface was re-polished again for the measurement of lift force.

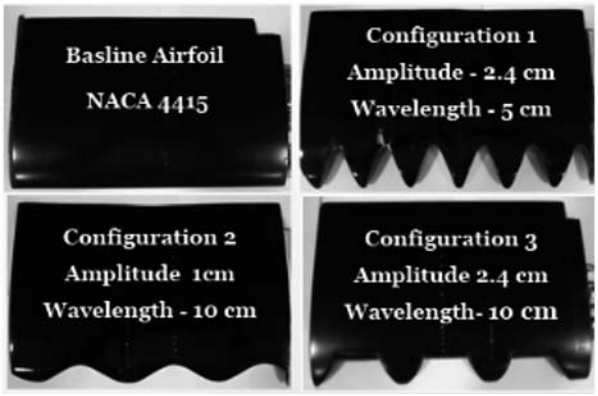

Fig. 1 Experimental models used for the research

For the measurement of the pressure distribution and the lift force, the experiments were carried out at Emirates Aviation College Aerodynamics Lab using an AF100 Subsonic Wind Tunnel. The lift force was measured using a three-component balance. The testing was carried out for $Re = 3.5 \times 10^5$ and the angle of attack was varied within the range $-3 \leq \alpha \leq 25$ degrees. Surface flow visualization was carried out to further analyze the flow. A mixture of china clay powder with kerosene of the ratio 1:10, i.e. 100 ml of china clay per 1 liter of kerosene , also known as kaolin, was prepared and spread over the surface of the models and the visualization was carried out for the post-stall region $\alpha = 18$ deg for $Re = 3.5 \times 10^5$.

3. Results and analysis

3.1 Chord-wise pressure coefficient distribution curves

From the pressure measurements obtained through the wind tunnel testing, a pattern was observed in the manner the pressure coefficient was distributed over the peaks and troughs of the configurations with leading edge protuberances in the post-stall region.

For the baseline model, the upper surface is covered with a negative pressure coefficient while, for the modified models, negative pressure coefficient is obtained near the leading edges of the peak. Adverse pressure gradient is however created as we move further away from the peak in the upper surface. On the other hand, the lower surface of the peaks is dominated by positive pressure coefficients along the entire chord length.

3.1.1 Baseline and configuration 1:

In the post-stall region, configuration 1 shows deterioration in the performance compared to the baseline. The baseline model shows a much higher negative pressure coefficient for the upper surface and positive pressure coefficient for the lower surface in Fig. 2

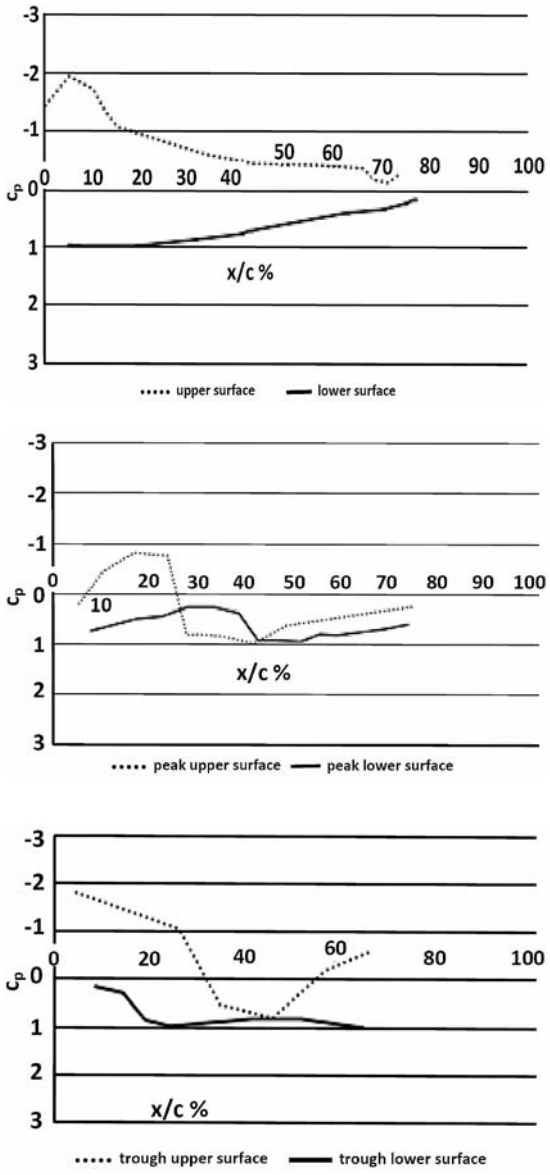

Fig. 2 Comparison between baseline (top centre) and Configuration 1: Peak (bottom left) and Trough (bottom right) at Re = 3.5 × 10^5

3.1.2 Baseline and configuration 2:

In the post-stall region, the peaks in the upper surface exhibit lower negative pressure coefficients, but the troughs a higher negative pressure coefficient distribution on the upper surface and higher positive pressure coefficient for the lower surface.

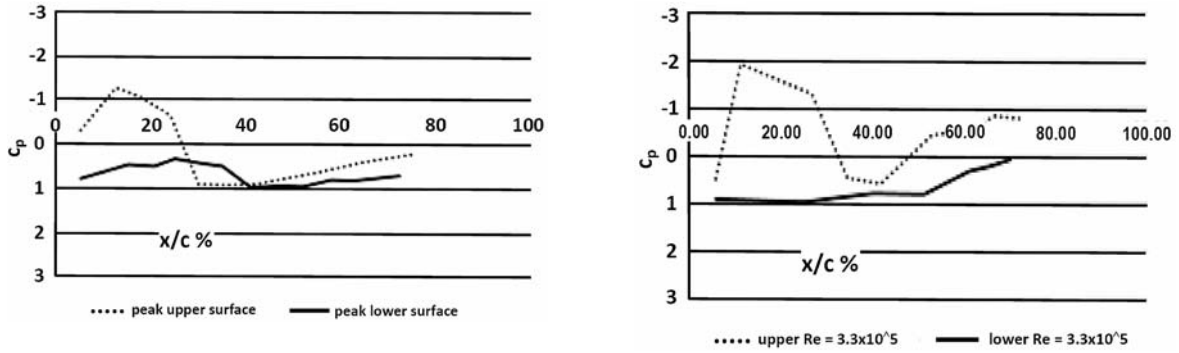

Fig. 3 Configuration 2: Peak (left) and Trough (right) at Re = 3.5 × 10^5

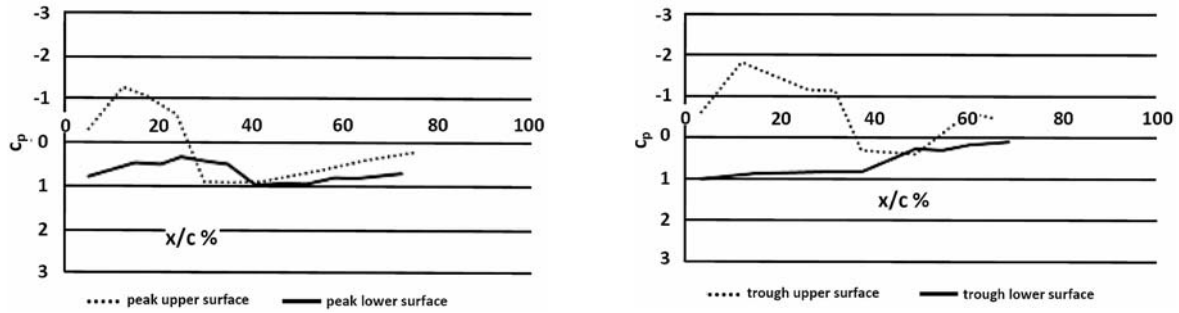

Fig. 4 Configuration 3: Peak (left) and Trough (right) at Re = 3.5 × 10^5

Thus, the troughs of the configuration 2 significantly improve the pressure distribution for better lift characteristics as compared to configuration 1 as exhibited in Fig. 3

3.1.3 Baseline and configuration 3:

As observed in Fig. 4, configuration 3 also shows deterioration in the performance in the post-stall region as the baseline possesses higher negative and positive pressure coefficients for the upper and lower surfaces respectively.

3.2 Lift coefficient

The lift force measured is presented below in Fig. 5 using the non-dimensional lift coefficient versus angle of attack for all the tested airfoils. The lift coefficient curve shows that the modified airfoils with leading edge protuberances improve the stall characteristics of the airfoil. The stall is delayed significantly for the modified leading edges compared to the baseline model.

Even though the presence of leading edge protuberances does not enhance the performance at low angles of attack, the maximum lift coefficient achieved is higher than that of the baseline. Configuration 2 obtained a maximum lift coefficient of 1.32 compared to 1.09 for the baseline, thereby increasing the maximum lift coefficient by 17.4% and increased the stall angle of attack by an increase of 28.5%.

While analyzing the three modified leading edges, it can be shown that protuberances with low amplitude perform better than those with high amplitude. Configuration 2, as such, exhibited the most enhancements in terms of lift coefficient amongst the modified airfoils.

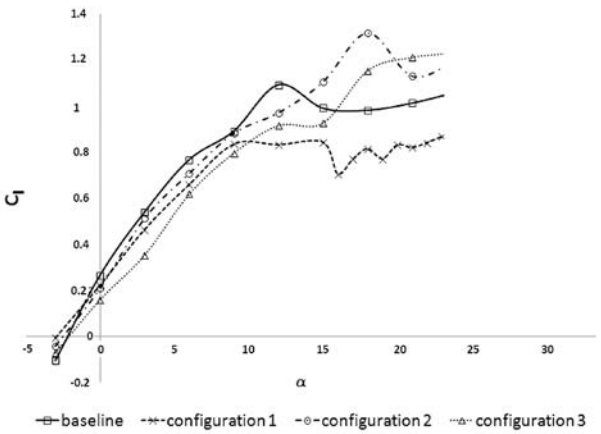

Fig. 5 Lift coefficient Vs Angle of attack (degrees) at Re = 3.5 × 10^5

Conclusion for $Re = 3.5 \times 10^5$ Tab. 2

Airfoil	Stall Angle (degrees) Range
Baseline NACA 4415	$12 \leq \alpha \leq 15$
Configuration 1	$16 \leq \alpha \leq 18$
Configuration 2	$19 \leq \alpha \leq 21$
Configuration 3	$27 \leq \alpha \leq 30$

3.3 Flow visualization

As seen below (Fig. 6), leading edge flow separation was observed for the baseline model in the post-stall angle of 18 degrees. Separation bubbles were also observed or the baseline model and the separation and re-attachment lines, due to the presence of the separation bubbles, can be clearly observed. For configuration 1, a very different flow pattern was obtained at the same post-stall angle. Streamline vortices were created at the tips of the peaks near the leading edge which delayed the flow separation behind the peaks. However, behind the troughs, reverse flow due to flow separation was observed. These vortices were created due to the sharp edges of the peak which resulted in the flow being unable to follow the airfoil pattern. Configuration 2 exhibited highly three dimensional flows, where, span wise flow was also created. Swirls can be observed arising from the peak of the upper surface. This could be attributed to the relatively higher pressure of flow over the peak compared to the flow pressure over the trough. Flow separation was observed for Configuration 3 at the edges of the leading edge of the trough. It can be concluded that the protuberances (peak) delays the flow separation.

Fig. 6 Flow visualization of the models at 18 degrees angle of attack and Re = 3.3 × 10^5. Baseline (top left) Configuration 1 (top right) Configuration 2 (bottom left) and Configuration 3 (bottom right)

4. Conclusion

A set of 2D NACA 4415 cambered airfoils having leading edge protuberances was tested in a subsonic wind tunnel. The effect of these leading edge protuberances, which mimic the protuberances on the flipper of the humpback whale, was analyzed for $-3 \leq \leq \alpha \leq 25$ degrees and $Re = 3.5 \times 10^5$ and compared with the performance of the baseline NACA 4415 model having the conventional straight leading edge. From the testing carried out, it was concluded that leading edge protuberances prominently improves the aerodynamic performance of 2D cambered airfoils in the post-stall region. The stall angles for all the modified leading edges were significantly delayed. The stall angle of attack was delayed by 28.5% and the maximum lift coefficient was increased by 17.4% for the protuberances with low amplitude as compared to the baseline model. On the other hand, the leading edge protuberances with high amplitude did not enhance the aerodynamic performance for any angle of attack. Although the models with the leading edge protuberances showed a decrease in the performance at low angles of attack, the presence of leading edge protuberances enhances the performance at high angles of attack.

Surface visualization illustrated that for the baseline model, the flow separated at the leading edge in the post-stall region with the formation of separation bubbles. However, for the models with the leading edge protuberances, the flow remained attached for a major portion of the chord length over the peaks with flow separation occurring in the troughs. Thus, the presence of leading edge protuberances improves the stall characteristics of 2D cambered airfoils by modifying the flow separation patterns and enhances the maximum lift coefficient for low amplitude protuberances at high angles of attack.

The results achieved are in accordance with previously carried out research for airfoils with leading edge protuberances which also proved that the presence of leading edge protuberances enhances the stall characteristics and improves the lift performance in the post- stall region. Based on the results achieved, the application of such leading edge protuberances can be utilized to enhance the performance of wind turbine blades and for low speed UAVs.

Acknowledgement

This research has been assisted by the works of Acrylic Extreme Production. L.L.C, Dubai, Arabian Wood Factory, Dubai and Dufco Interior works, Dubai in manufacturing the airfoils and delivering the materials for the accomplishment of the research project. The relentless support of our research supervisor, Dr. Young Hwan Kim, and the faculty members of the Aeronautical Engineering Department of Emirates Aviation College, is highly appreciated.

References

[1] HANSEN, K., KELSO, R., DALLY, B.: *Three Dimensional Effects on the Performance of the Tubercles at the Low Speed Reynolds Numbers. Adelaide,* Australia, 2010.
[2] JOHARI, H., HENOCH, C., CUSTODIO, D., LEVSHIN, A.: *Effects of Leading-edge Protuberances on Airfoil Performance.* AIAA, 2007.
[3] FISH, P. W.: *Influence of Leading Edge Tubercles on Wing Performance.*

Uncited references

[4] SELIG, M., DETERS, R., WILLIAMSON, A.: *Wind Tunnel Testing Airfoils at Low Reynolds Number.* Florida, 2011.
[5] HANSEN, K., KELSO, R., DALLY, B.: *Performance Variations of Leading-edge Tubercles for Distinct Airfoil Profiles.* AIAA, 2011.
[6] MIKLOSOVIC, D., MURRAY, M., HOWLE, L.: *Experimental Evaluation of Sinusoidal Leading Edges.* J. of Aircraft, 2007.
[7] WEBER, P., HOWLE, L., MURRAY, M., MIKLOSOVIC, D.: *Computational Evaluation of the Performance of Lifting Surfaces with Leading-edge Protuberances.* J. of Aircraft, 2011.
[8] PEDRO, H., KOBAYASHI, M.: *Numerical Study of Stall Delay on Humpback Whale Flippers.* AIAA, 2008.
[9] CUSTODIO, D., JOHARI, H.: *Aerodynamic Characteristics of Finite-span Wings with Leading Edge Protuberances.* AIAA, 2012.

Barbara Hlavnova – Milena Svitekova – Jana Simonidesova *

ANALYSIS OF THE ENERGY MIX OF SLOVAKIA IN THE CONTEXT OF IMPROVEMENT OF QUALITY OF THE ENVIRONMENT

The contribution is focused on the trends of energy balance of Slovakia that is the key indicator determining the consumption of fuel-based energy sources accepting the principles of sustainable development and improving the quality of the environment. It refers to the development of pollutants release from the energy industry in the production of electricity and thermal energy referring to the potential use of RES in the energy mix the composition of which is in direct interaction not only with the development of the environmental load of the components of the environment but also with energy security and energy independence of Slovakia.

Keywords: *Fuel-based energy resources, renewable energy sources, energy mix*

1. Introduction

The field of the energy mix and its prediction is a topical issue which is the subject of much debate not only in Slovakia but also worldwide mainly due to the increase of the environmental protection and the need to replace exhaustible energy sources by renewable resources.

The energy sector is one of segments significantly contaminating the environment. An integral part of the scientific projections of anthropogenic society is also the problem of ensuring sufficient energy while ensuring a quality environment. Total energy consumption and energy structure of the Slovak economy is one of the limiting factors of energy impact on the environment. It is therefore essential to ensure harmonious relationship of energy and the environment through an introduction of appropriate technologies that will in particular use renewable energy sources (hydro, wind, solar, geothermal, tidal energy, etc.) and the conventional energy technologies will be equipped with environmental protection devices with high efficiency. All energy sources must be used in a way that takes into account both human health and the environment and its quality.

2. Consumption of fuel-based energy sources and their influence on the quality of the environment in Slovakia

Energy sources that constitute the energy mix are crucial in ensuring the needs, living standard and overall development of human society. The current evolution of social energy consumption refers to the fact that the most used seems to be electric energy which is also the most common type of energy for present and future economic development of Slovakia. Dominant forms of power generation are thermal and nuclear power whose common feature is so called thermal environmental contamination resulting from the relatively low conversion efficiency of thermal energy into electricity [1]. The projected development and consumption of electricity after commissioning of the third and fourth blocks of Mochovce nuclear power plant and the planned construction of renewable energy sources (RES) energy balance should be invoked in the time span around 2013. The planned energy mix of Slovakia includes a larger share of nuclear energy in the future. The relatively low share of RES is the reason for this situation. Binding objective of Slovakia by 2030 is to achieve a minimum of 14% share of RES in final energy consumption [2].

Thermal power plants burn fossil fuels and in this process a wide range of airborne contaminants, for example, harmful compounds of sulphur, arsenic, selenium, tellurium, mercury, lead, cadmium and other toxic active substances (including organic compounds that are carcinogenic or teratogenic in certain cases) are produced. The adverse effects on the environment are most negatively manifested by gaseous contamination (the most serious is SO_2) and solid emissions (fly ash). Fly ash can be captured with high efficiency but SO_2 is a major problem especially in the atmosphere where it reacts with other components and secondarily contaminates the soil and water resources [3].

Nuclear power plants operate on a similar principle as thermal power plants, i.e., obtain energy by transforming thermal energy into electricity. Fission of uranium U^{235} to neutrons in a nuclear reactor creates a large amount of heat used for steam production which drives the steam turbine generators. In addition to the residual heat (cooling by water) no further emissions are created so

* **Barbara Hlavnova[1], Milena Svitekova[2], Jana Simonidesova[3]**
[1] Institute of Geoturism, Faculty of Mining, Ecology, Process control and Geotechnology, Technical University of Kosice, Slovakia, E-mail: barbara.hlavnova@tuke.sk
[2] Department of Communications, Faculty of Operation and Economics of Transport and Communications, University of Zilina, Slovakia
[3] Department of Finance and Accounting, Faculty of Business Economy, University of Economics in Bratislava, Slovakia

some experts prefer this method of electricity production to incineration if trouble-free plant operation is ensured. In some countries this method of electricity production is dominant (France, Japan). In terms of environmental contamination the spent fuel is dangerous because of radioactive waste and the activated parts of nuclear power after termination of the operation. By nuclear power plants more than 52% of electricity is currently produced in Slovakia. Nuclear fuel supply is ensured by long-term contracts from the Russian Federation. It is useful to support the transition to improved fuel with better use of nuclear material in nuclear fuel which results in a reduction of its consumption. In connection to the use of nuclear fuel for electricity generation resolution of the problem of storage of spent nuclear fuel as well as the question of decommissioned nuclear facilities is a key issue. In addressing the issues in this field Slovakia is in line with the EU [1].

The primary problem of the Slovak energy sector is the high up to about 90 % dependence on imported fuel-based energy sources (FES – including nuclear fuel) from abroad as due to the natural conditions and the current technological possibilities there are very low levels of these resources in Slovakia. Domestic sources of fossil fuels include only brown coal and lignite. A similar situation exists in liquid (2% of own resources) and gas (3% of own resources) energy sources. Hydropower and biomass are the most involved RES in primary production [1 and 4].

The structure of the FES in the SR is characterized by reduced consumption of solid and gaseous fuels and heat, whereas increased consumption of liquid fuels, electricity and renewable energy sources in the period from 2001 to 2010 (Fig. 1).

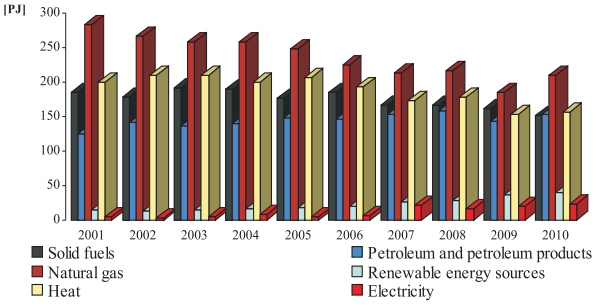

Fig. 1 Development of consumption of particular types of primary energy sources by fuel type Source: Prepared according to SAZP, 2000 - 2011

Consumption of solid fuels gradually declined during the monitored period by nearly 19%. Consumption of gaseous fuels declined by 26% with slight fluctuation in 2010 compared to 2001. The liquid fuel consumption increased by 18% for the same period. The consumption of RES increased by about 62% in 2010 compared to 2001. The most significantly increased the consumption of electricity by more than 80% in the last 10 years. An extremely important role in the structure of primary energy sources plays the use of nuclear fuel in Slovakia in recent years. Due to the replacement of petroleum products with biofuels only a slight increase in petroleum consumption is expected especially in transport.

Domestic *brown coal* currently accounts for approximately 79% of the consumption of brown coal needed to produce electricity and heat. It plays an important role in ensuring security of electricity supply. The rest of the necessary amount of brown coal and all the black coal are imported. A gradual decline is expected in the brown coal mining and in the long term brown coal mining can not be considered sufficient to meet the needs of electricity and heat production. Domestic coal, however, remains the only non-renewable resource needed to ensure the system reliability. Consumption of *natural gas* was about 5.7 billion m^3 in Slovakia in 2010 which represents an annual increase of about 6.5%. The domestic mining contributes by about 2% to this consumption. The rest of the natural gas is imported from Russia. The increase in natural gas consumption has caused economic recovery after the global financial crisis which started in January 2009. The share of the Slovak Gas Company, Inc. (SPP) on the gas supply on the total gas supply to industrial customers was 79%. The gas market in 2010 entered a new phase when other companies entered the market of gas suppliers to industrial consumers. Their share was 21.5% of all the gas supplied, thus it increased threefold compared to 2009. The share of natural gas in primary energy sources is expected to decline moderately by 2013 or more precisely 2030 but it still would be above the EU average [5]. Slovakia imports about 5.5 million t of petroleum annually. This volume is guaranteed by a long-term international agreement with the Russian Federation. 3.2 million t of the imported petroleum amount is used to meet the domestic consumption. Domestic extraction takes a share of less than 2% in oil consumption

Currently, about 4.7 TWh of electricity is produced by *RES* – including hydro power potential of large hydropower plants – representing approximately 17% of gross final energy consumption of electricity. Biomass is the most promising renewable source for heat generation with total annual potential of about 75.6 PJ suitable for energy production. Biomass is also a promising source of electricity generation [1 and 4].

The development of final energy consumption showed a declining trend in the monitored period till 2007 (drop by nearly 13.4% compared to 2001). In 2008, the final consumption increased by more than 2% compared to the previous year. In 2010, it increased by nearly 7.8% (418,853 TJ) compared to the previous year and almost reached the 2008 level of 418 291 TJ (Fig. 2). In 2010, the largest share of total consumption was represented by industry (32%), followed by three sectors: households (23%), transport (22.5%) and trade and services (21%). The lowest share of only 1.3% was represented by the agricultural sector. There is an upward trend in the transport sector in the monitored period with consumption increased by 35% over the last 10 years. Since 2001 the consumption in other sectors has been declining with the exception of trade and services sector in which the consumption was less than 1% higher in 2010 than in 2001.

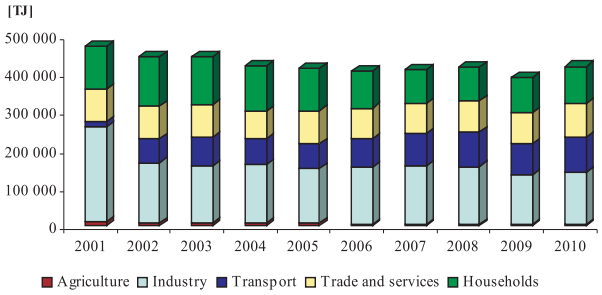

Fig. 2 Development of final energy consumption in different sectors of Slovak economy
Source: Prepared according to SAZP, 2000 – 2011

Industry showed the largest share of consumption of selected FES (Fig. 3) in Slovakia in 2010. From 2001 to 2010 the consumption of gaseous fuels and the consumption of fossil fuels declined by about 42% and 20% respectively in the industry. On the contrary the consumption of liquid fuels increased by about 20%. Since 2001 it is also possible to monitor the consumption of RES and wastes, the most used are wood and industrial waste (an increase of about 67%). Consumption of solid fuels in agriculture dropped significantly (about 81%). Brown coal and lignite show the highest consumption of solid fuels. Petroleum shows the highest consumption of liquid fuels (nearly 97% share) while in the period from 2000 to 2010 the overall consumption decreased by nearly 33%. The most consumed gaseous fuel – natural gas – decreased by about 29% during the whole monitored period. The final consumption of RES and waste are the most influenced by the consumption of wood, industrial waste and biogas. In the transport sector the consumption of gaseous fuels increased most notably (by almost 100%), the consumption of liquid fuels also increased (by 25%), and the final consumption of solid fuels decreased (by almost 90%) in the period of 2001 – 2010 [1].

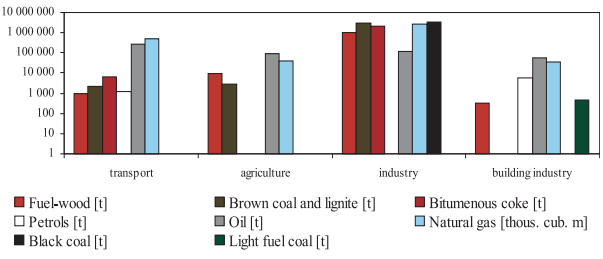

Fig. 3 Consumption of selected FES in certain sectors of Slovakia in 2010
Source: Prepared according to SU SR, 2000 – 2011
Note 1: Not all FES are used in particular sectors.
Note 2: Logarithmic axis is used.

The energy sector is one of the sectors most negatively affecting the environment and human health. The energy sector as the largest emitter of greenhouse gases mainly carbon dioxide, methane but also nitrous oxide, contributes in a large extent to climate change and intensification of the greenhouse effect. Total greenhouse gas emissions in 2009 were in the amount of 43 426.07 Gg of CO_2 equivalent which represented a reduction of 41.44% compared to the reference year 1990 (74 154.78 Gg of CO_2 equivalent). Production of electricity and heat based on fossil fuels is accompanied by production of sulphur dioxide, oxides of nitrogen, carbon monoxide and solid pollutants. Within the protection of air greening of the resource base is important in order to reduce the production of emissions released into the air. In the period 1990 – 2009 pollutant emissions from the energy sector fell sharply. The solid pollutants and sulphur dioxide emissions decreased most significantly by about 90% and 80% respectively. In 2009 compared to the reference year, the emissions of oxides of nitrogen and carbon monoxide decreased by approximately 49% and 48% respectively (Fig. 4) [1].

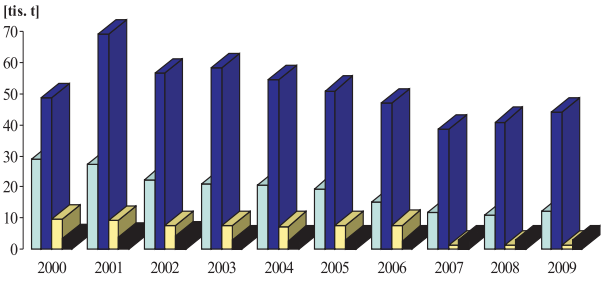

Fig. 4 Development of the emissions of major pollutants from stationary energy resources
Source: Prepared according to SAZP, 2000 – 2011

21 436 thous. m^3 of waste water was released to recipients from different technologies and cooling processes in 2010. Sewage contributed to a lesser extent in the released waste water. Waste water from the technologies is chemically contaminated, in case of nuclear power stations in the primary circuit also radio chemically. For the water that is used for cooling, thermal pollution is mostly significant. The contamination of sewage is mostly biologi-

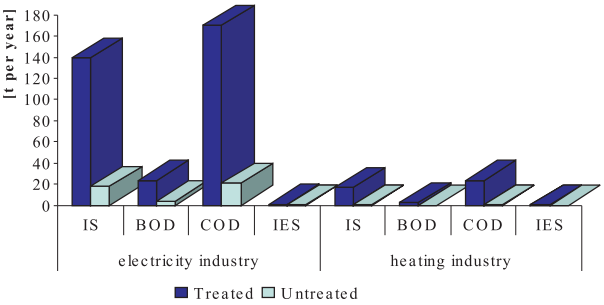

Fig. 5 Quantification of indicators of pollution in waste water from power generation in 2010
Source: Prepared according to SAZP, 2000 – 2011

cal. The indicators of insoluble substances (IS) and COD show the greatest burden, the indicator of insoluble extractable substances (IES) show the smallest one (Fig. 5).

3. Possibilities of the improvement of the quality of the environment

From the above information on the consumption of FES and the composition of the energy mix results that minimization of the negative environmental impacts can be achieved by increasing the share of renewable energy. In this way it is also possible to increase the energy independence of Slovakia which should also be strategically important for the economic success of the country. Even in the use of RES it is important to ensure the continuity of energy supplies to a consumer which requires a correct combination of renewable and non-renewable energy sources. One of the best combinations is the combination of solar energy and natural gas. It is not possible to clearly identify the most suitable FEZ for increase of the quality of the environment while maintaining the satisfaction of needs of human society. New technologies are constantly emerging on the market which contribute to greater environmental protection thus it can not be clearly stated which FES is the most advantageous in this respect. Nevertheless, particular FES can be compared taking into account their negative impacts on the environment (Table 1).

A comparison of the negative impacts of FES on the environment — Tab. 1

FES	Emissions	Solid waste	Reserves
Sun	–	–	unlimited
Wind	–	–	unlimited
Hydro	–	–	unlimited
Geothermal	–	–	unlimited
Biomass	–	–	unlimited
Nuclear	indirect emissions*	radioactive waste	
hot water	approx. 270 years		
Coal	CO_2, Hg, NO_X, SO_X	slag	approx. 2 cent. or more
Petroleum	SO_X, CH_4, CO_X, NO_X	waste oil	40 to 50 years
Natural gas	CH_4, CO_2, NO_X	–	approx. 2 cent.

* Indirect emissions – from the extraction, transport and processing of uranium, but also in the construction and decommissioning of a nuclear power plant

An increase of the share of RES in electricity and heat energy production would definitely contribute to reducing the environmental burden caused by the energy sector as the production of greenhouse gases, solid pollutants and, of course, the heat pollution would decrease. The use of RES in energy mix of Slovakia is determined by the so-called technically exploitable potential of RES the value of which has been estimated at 136 421 GWh per year while currently only 30% being used (Table 2). Biomass from agricultural production has the highest technically exploitable potential of all RES (6 300 GWh per year) and sludge from wastewater treatment plants has the lowest one (230 GWh per year). At present, about 19% of domestic electricity consumption is produced by RES. The total exploitable potential of particular RES allows increasing their share in total electricity generation to 24% in 2020 and 27% in 2030. The prognosis of RES use in electricity production expects this production reaching nearly 8 000 GWh per year in 2020 with predicted largest share of electricity being produced by hydropower (large hydropower stations of above 10 MW) and smallest share by photovoltaic power plants. The prognosis of RES use in heat production expects this production reaching nearly 35 PJ in 2020 with predicted largest share of the heat production by solid biomass and smallest by heat pumps [6 and 7].

Technically exploitable potential of RES in Slovakia — Tab. 2

RES	Technically exploitable potential	Present exploitation	Unused potential
	[GWh per year]		
Geothermal energy	**6 300**	**340**	**5 960**
Wind energy	**605**	**0**	**605**
Solar energy	**5 200**	**7**	**5 193**
Small hydropower plant	**1 034**	**202**	**832**
Biomass	**16 794**	**3 192**	**13 602**
Forest biomass till 2010 after 2010	2 828 5 623	494	2 334
Wood-processing industry	4 881	2 638	1 880
Agricultural biomass	6 586	60	6 526
Energy utilisation of waste	**3 535**	**1 251**	**2 284**
Wastewater sludge	230	13	217
Municipal solid waste	1 775	368	1 407
Other waste	1 530	870	660
Biological fuels	**2 500**	**330**	**2 170**
Hydropower plants	**6 607**	**5 093**	**1 514**
Sum:	**37 895**	**10 415**	**27 480**

Source: National Action Plan for Renewable Energy, 2010 [7]

As mentioned earlier, biomass has a relatively high potential for energy recovery in Slovakia. It can be treated by cogeneration that can continuously produce electricity and thermal energy which is considered to be CO_2 negative. Fermented biogas is characterized by a relatively high content of methane (50–60%) making its

calorific value in range around 22 MJ per cubic metre. Moreover, its energy use contributes to reducing emissions and the greenhouse effect. When using biomass in combination with some non-renewable types of energy, for example natural gas, the production of solid pollutants sulphur dioxide could be eliminated thereby it would also contribute to prevention of subsequent reduction of soil acidity or the pH values of water resources and other types of secondary pollution. This would also contribute to the use of domestic FES for electric and thermal energy production in an economically efficient principle otherwise the unused biomass presents waste mostly disposed to landfill in Slovakia. It would also provide an appropriate additional source of heat and electricity to meet the domestic consumption thereby it would also contribute to the energy independence of Slovakia and thus an increase of the energy independence of Slovakia.

4. Conclusion

The composition of the energy mix determines the pollution of the components of the environment hence its overall environmental quality. Production of energy from non-renewable FES contributes significantly to air pollution especially by greenhouse gases, burdens the water sources (both withdrawal and the pollution generated) and causes the acidification of the environment. And it is why the energy mix in an interaction with total energy consumption presents a limiting factor of negative impact of energy sector on the environment. A gradual increase of the share of RES in energy production would both ensure a way that takes human health, which is an integral part of the environment in the close interaction with its individual components into account and accept the rules and principles of sustainable development of the environment. It should also be noted, however, that an exclusive use of RES for energy needs is not possible because of a need for continuous provision of energy supplies. This, therefore, requires a combination of renewable and non-renewable resources making it possible to ensure a continuous supply of energy and at the same time it would contribute to protection of the environment by reducing greenhouse gases and solid pollutants.

References

[1] STROFFEKOVA, S.: Energetika a jej vplyv na zivotne prostredie v Slovenskej republike k roku 2009 [Energy and its Impact on the Environment in the Slovak Republic in 2009] . Indikátorova sektorova sprava. [online]. Banská Bystrica, SAZP, 2010. Available on-line: <http://www1.enviroportal.sk/pdf/sektor/Energetika_sektor_09.pdf>.

[2] Energeticka politika SR [Energy Policy of SR]. In: MH SR. [online]. 2011. [cit. 2012-03-15]. Available on-line: <http://www.economy.gov.sk/energeticka-politika-sr-5925/127610s>.

[3] PAVOLOVA, H., CSIKOSOVA, A., CULKOVA, K., ANTOSOVA, M.: Efficiency of Pollutants Removal in Kosice Area with Respect of Living Qquality Increasing. *Applied Mechanics and Materials,* vol. 152–154 (2012), pp. 489–494. ISSN 1660-9336

[4] PAVOLOVA, H., SENOVA, A., BAKALAR, T.: Increase of Alternative and Renewable Energy Sources Utilization in Slovakia by 2020 in Comparison to other Selected EU Countries. *Applied Mechanics and Materials*, vol. 152–154 (2012), pp. 495–500. ISSN 1660-9336.

[5] Spotreba zemneho plynu na Slovensku vlani rastla [The Consumption of Natural Gas was Growing in Slovakia Last Year] [online]. 2011. Available on-line: <http://www.energia.sk/clanok/zemny-plyn/spotreba-zemneho-plynu-na-slovensku-vlani-rastla/3188/>.

[6] Elektrina vyrobena z obnovitelnych zdrojov [Electricity Produced from Renewable ources] Information available on-line: <http://www.statistics.sk/pls/eutab/html.h?ptabkod=tsdcc330>

[7] Narodny akcny plan pre energiu z obnovitelnych zdrojov [National Action Plan for Renewable Energy], Ministerstvo hospodarstva a vystavby SR. [online]. 2010. Available on-line: <www.economy.gov.sk/narodny-akcny-plan-pre-energiu-z-obnovitelnych-zdrojov>.

Milan Zmindak – Pavol Novak *

SPECIAL APPROACH FOR THERMAL MODELLING FIBRE-REINFORCED COMPOSITES WITH LARGER ASPECT RATIO

Fundamental solutions and their derivatives located along fibre axes are presented to simulate the interactions of matrix and reinforcing elements in composite materials, when the primary field is a scalar function temperature in heat conduction. The inter-domain continuity is specified in discrete points on fibres boundaries. Intensities of the source functions are defined by 1D NURBS (Non-Uniform Rational Basis Spline) and computed in LS (Least Square) sense in the fibres. The inter-domain continuity equations have to be completed by balance equations (energy, equilibrium, etc.) in order to obtain temperature in centre of each fibre. Gradients of temperature are supposed to be constant in cross-sections of the fibres and are computed iteratively by considering them to be linear along fibres in the first step. Material properties of both matrix and fibres are assumed to be homogeneous and isotropic. Three numerical examples giving two fibres overlapping in some length in infinite matrix show the numerical behaviour of the problem for heat conduction.

Keywords: *MFS, composites, finite fibres, meshless method, source functions, NURBS*

1. Introduction

In past decades, fibre-reinforced composites have been widely used in engineering applications due to the superiority of their electro-thermo-mechanical properties over the single matrix. Particularly, composite materials reinforced by fibres, or with Carbon Nano-Tubes (CNT) are often defined as materials of future. Although composite materials are designed as fatigue insensitive, especially when compared to metallic ones, they suffer from fatigue loads as well [1 and 2].

Understanding the physical behaviour of these fibre-reinforced composites is essential for structural design. The aspect ratio of fibres (length to diameter) is often very large and all well-known numerical methods, including the Fast Multipole BEM (FMBEM) [3] are not effective to simulate such problems.

The fundamental solution is basis for both the Boundary Element Method (BEM) and the Method of Fundamental Solutions (MFS) [4 and 5]. As for the BEM, elements are used to satisfy boundary conditions and the fundamental solutions (FS) are considered to be continuously distributed along the domain boundaries on elements being one dimension lower than the domain, the MFS is a meshless method using discrete source functions, FS, located outside the domain. Both methods have some advantages and drawbacks, as it is well known [6].

Recently developed Method of Continuous Source Functions (MCSF) [7 and 8] uses 1D continuous source functions – fundamental solutions and their derivatives located along fibre axis to simulate effect of fibres in the matrix, i.e. the interaction of the matrix with fibres in composite material reinforced by the fibres. We present here the problems when the primary field is a scalar function (e.g. temperature in heat conduction) or, if it is a vector function (e.g. displacements in elasticity). The material properties are investigated on a Control Volume Element (CVE) starting with inter-domain conditions on the fibre boundaries corresponding to constant gradient field in corresponding homogeneous field of matrix material and changes in the field are computed due to reinforcing fibres by splitting the problem into two parts, the first one corresponding to the homogeneous material and the second one corresponding to the reinforcing effect.

The inter-domain boundary (compatibility) conditions and basic unknowns have to be specified so that good numerical stability is achieved. It is realized by specifying field quantities (temperatures, displacements, strains) by difference of the value in a collocation point and that in a related point (centre of the fibre, or another point on a corresponding fibre cross-section boundary).

The inter-domain continuity equations have to be completed by balance equations (energy, equilibrium, etc.) in order to obtain temperature, displacement, etc. in the centre of each fibre. The solution is obtained iteratively considering constant value temperature, displacement, etc. along each fibre in the first step. Gradients of the field values define gradients of a similar field in the fibres, both related by material properties of matrix and fibres and they define corrections for inter-domain compatibility in the next iteration step.

The resulting system of equations is evaluated by the LS method. This enables to satisfy the inter-domain boundary conditions in a cross-sectional direction with good numerical stability of the

* **Milan Zmindak, Pavol Novak**
Department of Applied Mechanics, Faculty of Mechanical Engineering, University of Zilina, Slovakia, E-mail: Milan.Zmindak@fstroj.uniza.sk

models. Variables inside the fibres are described by classical methods used in continuum mechanics.

Note that the model assumes that the fields in cross-sections are constant, e.g. only axial stiffness of fibres is considered. As the aspect ratio is large, the bending stiffness of fibres is negligible comparing to their axial stiffness and such assumption reduces the problem, too.

Note also that the cross-sectional dimensions of CNT are very small and methods of continuum mechanics are not applicable for such a problem. However, the axial dimensions are much larger and so the models are applicable also for the material reinforced by CNT.

2. Source functions in MCSF models

We assume all matrix materials and fibres are homogeneous and isotropic, the dimensions of the matrix are infinite and models are restricted to linear behaviour. Primary variables can be scalar like in temperature field in heat conduction, or vector like displacement field in deformation of elastic bodies by forces. All the fields are split into two parts, the homogeneous part corresponding to the homogeneous problem of the matrix without fibres and local part containing the influence of interactions of fibres with the matrix. We will deal especially with the local fields in the matrix of the composite material.

The MCSF is a meshless method which satisfies the inter-domain compatibility in collocation points (Fig. 1) on the fibre-matrix interface.

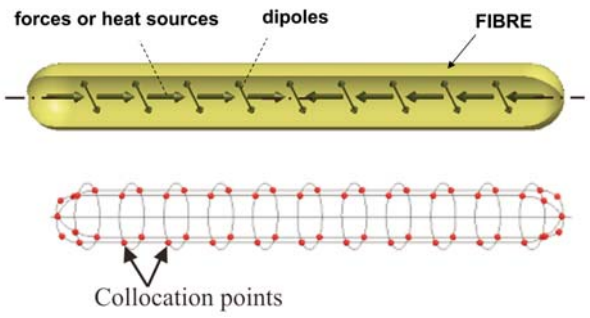

Fig. 1 Distribution of source functions and collocation points

Due to a large aspect ratio of fibres, the stiffening effect in elasticity and conductivity of fibres is realized especially by corresponding effect in the fibre axis direction. Because of this, the inter-domain compatibility between the fibre and matrix can be simplified and we assume that the temperature, displacement, strain, stress, etc. in all points of the cross-section are equal to each other.

The interaction of fibres with matrix is simulated in the MCSF by source functions which are 1D-continuously distributed along the fibre axis. The source functions are fundamental solution of the corresponding problem (heat sources in heat conduction and forces in elasticity) and their derivatives. The forces are directed in the fibre axis direction. These source functions, however, are not able to simulate correctly the interaction of fibres with the matrix. In addition the derivatives of the source functions, heat dipoles are included along the fibre axes.

The temperature field induced by a unit heat source acting in an arbitrary point of infinite domain is the fundamental solution for heat problems and it is given by:

$$T = \frac{1}{4\pi r} \tag{1}$$

where r is the distance of the field point t and source point s, where the heat source is acting at, i.e.

$$r = \sqrt{r_i r_i}, \quad r_i = x_i(t) - x_i(s) \tag{2}$$

with the summation convention over repeated indices.

Temperature field induced by a unit heat dipole in x_i direction is:

$$T = \frac{1}{4\pi}\left(\frac{1}{r}\right)_{,i} = -\frac{1}{4\pi}\frac{1}{r^2}r_{,i} = -\frac{1}{4\pi}\frac{r_i}{r^3} \tag{3}$$

and

$$r_{,i} = \frac{\partial r}{\partial x_i(t)} = \frac{r_i}{r}. \tag{4}$$

3. Computational simulation in the MCSF

In order to find the unknown intensities of the source functions, we have to solve the 1D quasi-singular equations in the form:

$$\int_\Gamma K(s,t) f(t) d\Gamma = g(s) \tag{5}$$

where $K(s,t)$ is the kernel function which is corresponding to the source function in our case, $f(t)$ is the unknown intensity of the source function, $g(s)$ is the function containing boundary conditions (BC) and Γ is the 1D integration curve along fibres' boundaries.

Note that in the present model the solution of the integral equation (5) is solved in the discrete points, s, of the fibre-matrix interface and the integration path and integration points, t, are outside of the domain, which is the matrix material. Because of it we can call this method a quasi-meshless method.

In the numerical evaluation of the integral equation (5) the intensity of source functions is approximated by 1D quadratic Non-Uniform Rational Basis Splines (NURBS) [9] which enable to define shape functions to have continuous first derivative over the

whole integration path and non-equal distribution of nodal points. Because of large gradients in the source functions close to the end parts of the fibres this is a good choice for numerical stability of the model [7 and 8].

Basic variables are temperature in heat and displacement in elasticity problems. Basic source functions are defined by unit heat source in heat and unit force in elasticity. Note that the corresponding source functions for these functions are weak singular for both problems (see equations (1) and (4)).

In the present formulation it is assumed that the fibres are superconductors in heat and rigid in elasticity problems. Moreover for simplicity we consider that the fibres are straight, parallel and constant gradient of temperature and displacement in fibres are considered in the fibre axes direction.

The temperature is not known in the composite, the BC for the local problem can be specified as follows:
- temperature difference between the corresponding collocation point and the centre of the fibre (it is opposite to the temperature difference in the homogeneous material),
- temperature difference between pairs of points on the opposite sides of the fibre cross-section for heat transfer.

The inter-domain continuity is satisfied using heat sources and heat dipoles with the vector direction perpendicular to each other and also to the fibre axis in heat transfer problems and by unit forces in fibre direction and two force dipoles perpendicular to each other and also to the fibre direction and two couples with torque effect perpendicular to the fibre axis. All these sources are 1D continuously distributed along the fibre axis.

However, temperature change of the centre of each fibre by the interaction is not known a priori in the heat problem. It is obtained by energy-balance/equilibrium condition in each fibre. This is realized by including further r.h.s. by prescribing temperature in corresponding fibre equal to one and zero for the other fibres. In this way we have as many additional r.h.s. as fibres in the problem.

For the finite conductivity of fibres the temperature change along fibre is computed by iteration process starting with superconducting fibre material. One can obtain temperatures and temperature gradients along fibres directly and from distributed source functions the heat flow in the fibre as a result in each iteration step. Because of dimensions the constant heat flow in the cross-section of fibre is a good approximation. From the heat flow and fibre material conductivity one can obtain temperature distribution in the fibre and correct the r.h.s. for the next iteration step.

The problem is very similar in the elasticity [7]. The iteration starts with assuming stiff fibres and prescribing displacement along a fibre without corresponding rigid body displacement in its centre. Displacements, strains and stresses are obtained directly in the matrix and total forces in cross-sections are computed from the source functions. Deformation of fibre is obtained assuming constant strains in the fibre direction and for finite stiffness of fibres and corrected r.h.s. is used for the next iteration step.

4. Computational results

Figure 2 shows a single straight fibre and patch of parallel fibres regularly distributed and overlapping in some length. To show some rules for modelling the composites with short fibres three examples with only two fibres are presented. The aspect ratio is 50:1, distance between axes of fibres is 4 (all quantities are dimensionless), diameter is 2, length is 100. The fibres overlap Δ in the length 4 for the first two examples and 40 for the third one. The conductivity of fibres is 20 000 times larger than that of the matrix in the first example and 1500 times larger in the second and third examples. Temperature gradient is equal to 1 in the fibre axis direction.

Intensities of source functions, heat flow and temperature along fibres are given in Figs. 3 to 5. Figures a) to c) correspond to examples 1 to 3.

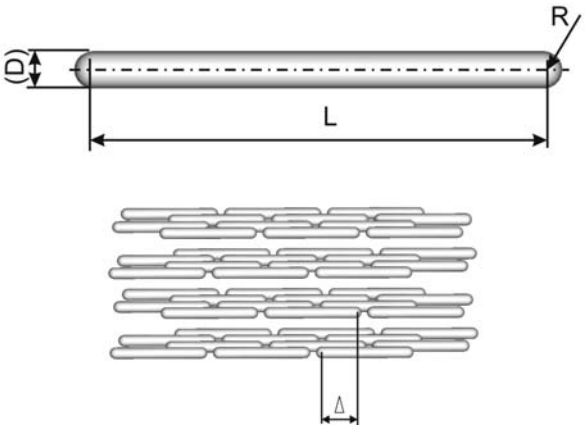

Fig. 2 Single straight fibre and patch of overlapping straight fibres

The red dotted line gives the computed results in the first iteration step, the blue full line is from the last iteration and the green dashed lines for the middle iteration steps. Note that the converged values are obtained in the second iteration for much larger conductivity in fibres to the matrix and in the fifth step for the smaller one with good accuracy.

Note in Fig. 3 the large gradient in source function intensity by the end of fibres but also in the closest points to the end of the neighbour fibre. In those parts it is necessary to choose nodal points defining the source function by NURBS dense. Appropriate density of the nodal points avoids numerical instability of the function. In documented examples the coordinates along fibre are given in Table 1 and are the same for all the examples.

Coordinates of nodal points along fibre Table 1

Distribution of nodal points along a half of fibre (symmetric to zero)
50 49.8 49.4 48 44 38 27 23 20 15 12 10 7 4 3 2

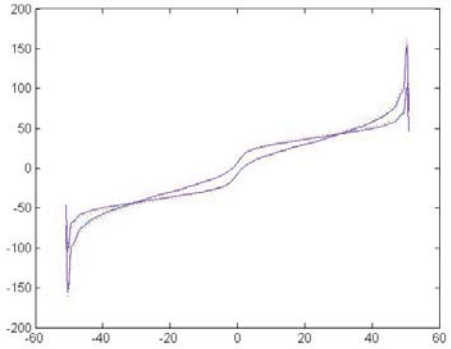

a)

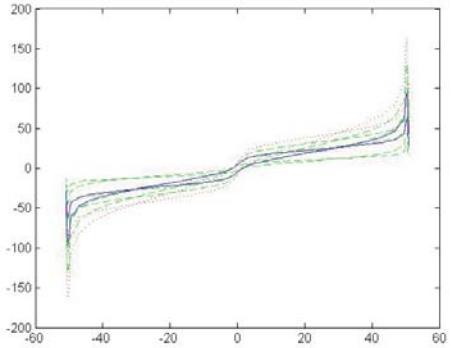

b)

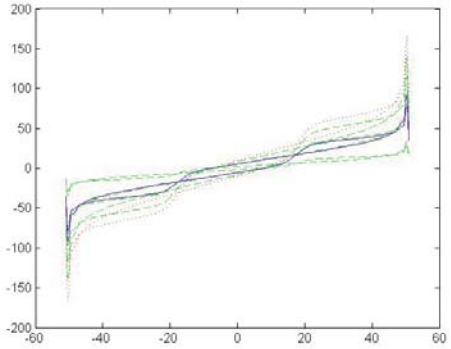

c)

Fig. 3 Heat source intensities along fibres ..... , the first iteration step - - - - - -, the middle iteration steps, ——— the last iteration

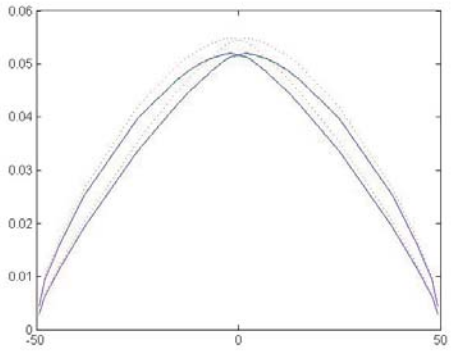

a)

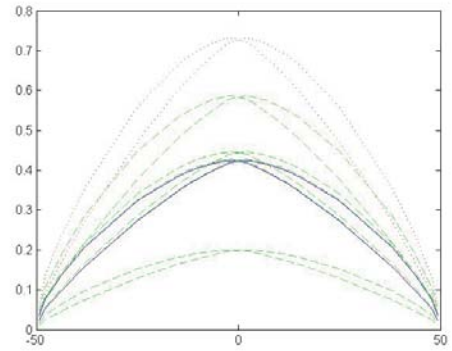

b)

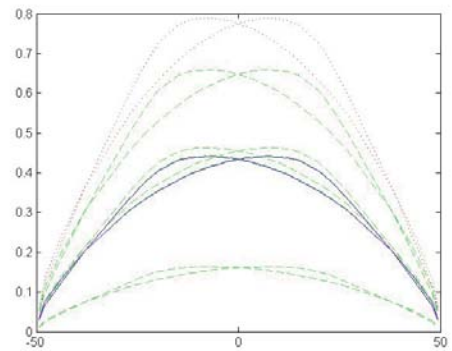

c)

Fig. 4 Heat flow in fibres

Temperature in the centres of fibres is 0 and −52 (the overlapped length is 48) for the first two examples and 0 and −70 (the overlapped length is 30) for the third example. Temperature increase in the lower temperature fibre as computed in the iteration steps is given in Table 2 and decrease in the higher temperature fibre is opposite.

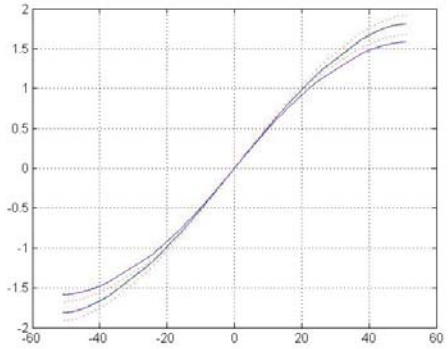

a)

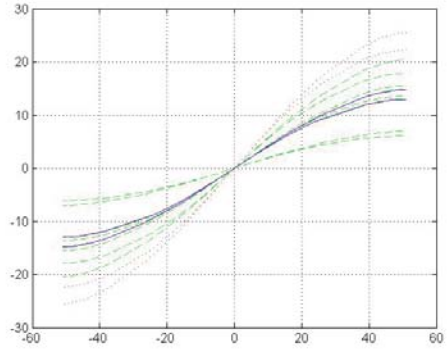

b)

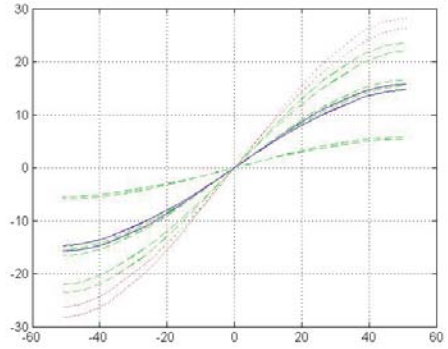

c)

Fig. 5 Temperature along fibres

Temperature change in the centre of fibre with lower temperature — Table 2

	Iter. 1	Iter. 2	Iter. 3	Iter. 4	Iter. 5	Iter. 6
Example 1	12.2131	11.5507	11.5870	11.5850	11.5851	11.5851
Example 2	12.2131	3.3497	9.7821	7.4480	7.1279	7.0840
Example 3	13.3508	2.7760	11.1520	7.8348	7.4899	7.4540

5. Conclusions

The MCSF is a kind of MFS which uses a fundamental solution and its derivatives to simulate the interaction of short fibres with matrix. Large aspect ratio does not enable to use both source functions in a discrete form and to satisfy the boundary conditions in collocation points. Using the 1D continuous source functions enables to reduce the solution considerably comparing to other known methods.

Source function in heat flow problem is a scalar, in elasticity it is a vector function, however the singularity is similar in both cases and so, the numerical behaviour is also similar [7 and 8]. Because of large gradients in the simulated fields by the interaction, the nodal points defining the continuous source along the fibre axis have to be denser in the parts, i.e. near the ends of the fibres and they have to be irregularly distributed. Numerical experiments have shown that the shape functions defined by NURBS are best suited for the numerical stability and accuracy.

Three numerical examples showing the numerical behaviour of the method on two parallel fibres in an infinite matrix overlapping in some part for a problem of heat transfer. The resulting system of equation is full but not square and is solved by the LS method. Similarly, as it is by BEM, the matrix is full also for the problem containing many fibres, but it can be torn into the interaction of each two fibres and interconnected iteratively, which enables further reduction of the problem [8].

Acknowledgement

This research was supported by the Slovak Grant Agency VEGA No. 1/1226/12)

References

[1] NICOLETO, G., BOKUVKA, O., COLLINI, L, KOPAS, P.: Fatigue Resistance in the very High-Cycle Regime. *Transaction of FAMENA*, vol. 29, No. 1, 2005, pp. 9–16.

[2] SAGA, M., KOPAS, P., VASKO, M.: Some Computational Aspects of Vehicle Shell Frames Optimization Subjected to Fatigue Life. *Communications - Scientific Letters of the Universtiy of Zilina*, vol. 12, No. 4, 2010, pp. 73–79.
[3] NISHIMURA, N.: Fast Multipole Accelerated Boundary Integral Equations. *Applied Mechanics Review,* 55, 2002, pp. 299–324.
[4] BREBBIA, C. A., TELLES, J. C. F., WROBEL, L. C.: *Boundary Element Techniques - Theory and Applications in Engineering,* Springer Verlag Berlin, New York, 1984.
[5] GOLBERG, M.A., CHEN, C.S.: The method of fundamental solutions for potential, Helmholtz and diffusion problems. *Boundary Integral Methods - Numerical and Mathematical Aspect,* Ed. M.A. Golberg: Computational Mechanics Publications, Southampton, 1998; pp. 103–176.
[6] KARAGEORGHIS, A., FAIRWEATHER, G.: The Method of Fundamental Solutions for the Solution of Nonlinear Plane Potential Problems, *IMA Journal of Numerical Analysis,* 9, 1989 pp. 231–242.
[7] KOMPIS, V., KOMPIS, M., KAUKIC, M.: Method of Continuous Dipoles for Modelling of Materials Reinforced by Short Micro Fibres, *Engineering Analysis with Boundary Elements* 31, 2007, pp. 416–424.
[8] KOMPIS, V., QIN, Q.H., FU, Z. J., CHEN, C.S., DROPPA, P., KELEMEN, M. CHEN, W.: Parallel Computational Models for Composites Reinforced by Short Fibres, *Engineering Analysis with Boundary Elements,* 36, 2012, pp. 47–52.
[9] PIEGL, L., TILLER, W.: *The NURBS Book, Springer-Verlag,* New York, 2nd edition, 1997.

Peter Kopas – Milan Saga – Milan Uhricik *

FATIGUE PERFORMANCE OF 6063-T66 ALUMINUM ALLOY UNDER COMBINED CYCLIC LOADING OF PARENT AND WELDED SPECIMENS

The article deals with the determining of fatigue lifetime of structural materials during multiaxial cyclic loading. The aim of this investigation is to evaluate the influence on fatigue behavior of the welded aluminum alloy EN AW 6063-T66. Experimental device was designed for combined bending – torque loading. The experimental part was focused on the modeling of combined biaxial loading and determining the number of cycles to fracture in the region of low-cycle fatigue. In-phase loading can be treated fairly well using the conventional hypotheses (von Mises or Tresca) on basis of nominal, structural or local strains or stresses. Based on the experimental results the fatigue design curves are compared to fatigue data from base metal and weldments.

Keywords: *Multiaxial fatigue, computational analysis, experimental analysis, torsion loading, bending loading, stress analysis, strain analysis, aluminum alloy, welding*

1. Introduction

Fatigue failure is an extremely complex physical process which is governed by a great number of parameters related to, for example, local geometry and material properties of the structural region surrounding the crack growth path. It is commonly recognized that it is impossible for a physical model to account for all fatigue influencing parameters, thus a lot of approximate models have been conceived for practical fatigue assessments. In every stadium of fatigue cumulative damage dominates a definite mechanism controlled by more or less known and verified rules [1]. There exists a stage of micro-plastic process in the total volume of material with a following stage of fatigue crack nucleation and stage of their growing with a more or less detailed zoning. Despite of this research no results have been achieved, which could be considered as successful ones. This applies mainly to the cases of random and combined stress, where today's procedures used in one axis stress analysis fail. Fatigue under combined loading is a complex problem. A rational approach might be considered again for fatigue crack nucleation at the material surface [2]. The state of stress at the surface is two-dimensional because the third principal stress perpendicular to the material surface is zero. Another relatively simple combination of different loads is offered by an axle loaded under combined bending and torsion. This loading combination was tested in our and also in many others experiments [3, 4]. In spite of this fact, fatigue mechanisms are still not fully understood. This is partly due to the complex geometrical shapes and also complex loadings of engineering components and structures which result in multiaxial cyclic stress-strain states rather than uniaxial.

The strength analysis of welded structures does not deviate much from that for other types of structures. Various failure mechanisms have to be avoided through appropriate design, choice of material, and structural dimensions. Design criteria such as yielding, buckling, creep, corrosion, and fatigue must be carefully checked for specific loading conditions and environments. It is, however, the fact that welded joints are particularly vulnerable to fatigue damage when subjected to repetitive loading. Fatigue cracks may initiate and grow in the vicinity of the welds during service life even if the dynamic stresses are modest and well below the yield limit. The problem becomes very pronounced if the structure is optimized by the choice of high strength steel. The very reason for this choice is to allow for higher stresses and reduced dimensions, taking benefits of the high strength material with respect to the yield criterion. However, the fatigue strength of a welded joint is not primarily governed by the strength of the base material of the joining members; the governing parameters are mainly the global and local geometry of the joint. Hence, the yield stress is increased, but the fatigue strength does not improve significantly. As already stated, the fatigue behavior of welded joints is random by nature. Very few load-bearing details exhibit such large scatter in fatigue life as welded joints. This is true even in controlled laboratory conditions. As a consequence, it becomes an important issue to take scatter into consideration, both for the fatigue process and for the final life. Furthermore, the in-services stresses may often be characterized as stochastic processes [5, 6].

The general issues described above are, of course, also important for welded joints. However, a welded joint has some peculiar

* **Peter Kopas, Milan Saga, Milan Uhricik**
Department of Applied Mechanics, Faculty of Mechanical Engineering, University of Zilina, Slovakia, E-mail: peter.kopas@fstroj.uniza.sk

features that make some of the subjects and parameters play a much more important role than others [7, 8]. Let us start with an S-N curve for a welded joint and compare it with other specimens. Figure 1 shows the S-N curves based on tests with one smooth plate, one plate with a bore hole, and one plate with a fillet welded transverse attachment. This type of fillet welded joint is often referred to as non-load-carrying due to the fact that the load is carried straight through the base plate. It is also noted that the applied force is transverse to the welding direction [9]. In the plate, the fatigue cracks can appear anywhere in the longitudinal edges of the plate, whereas they will appear at the inner edges of the bore hole transverse to the applied loading in the specimen with the hole. The latter phenomenon is due to the stress concentration at the edge of the hole. In the fillet welded joint the cracks will appear at the weld toe and grow through the base plate in a direction perpendicular to the applied principal stresses. The cracks are indicated on the specimens in Fig. 1. The cracks may emanate from several spots along the weld seam. Small semi-elliptical-shaped cracks are formed, grow, and coalesce to become larger cracks. In the final stage the remaining ligament of the plate section is too small to carry the peak load.

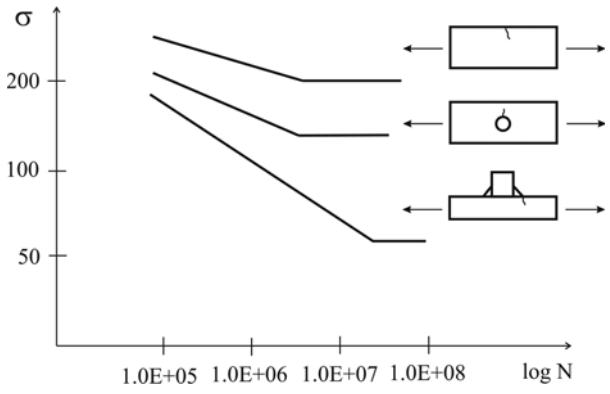

Fig. 1 Fatigue life curves for various details [8]

The difference between the S-N curve for the specimen with the hole and the S-N curve for the welded joint is rather surprising considering the fact that the bore hole creates a stress concentration factor close to 3 at the edge of the hole. The relatively short fatigue life of welded detail is explained, in the main, by three factors:

- severe notch effect due to the attachment and the weld filler metal,
- presence of non-metallic intrusions or micro-flaws along the fusion line,
- presence of large tensile residual stresses.

2. Test equipment design

The design of experimental equipment is based on a mechanical principle (Fig. 2). The constant rotation is generated by excenter and linkage mechanism. By changing of excentric magnitude it is possible to change a loading magnitude. Also if we change the length of connecting crank on the experimental equipment, there will be a change in the loading cycle character (proportional-non-proportional loading, bending/torsion loading, etc.) [10]. Power of the device is secured by two synchronic electromotors with frequency converters from 0.5 Hz to 100 Hz. Loading frequencies are identical with the frequency of rotation drive. Synchronization of the electromotors is secured by electronics and allows synchronization of the loading amplitude. The synchronization of electromotors also allows setting the phase shift for individual loading levels. There are also two force measurement systems included in the experimental equipment. These systems may be used for measurement of force values during the loading process. For evaluation of fatigue curves it is necessary to know stress and strain conditions on individual loading levels [11].

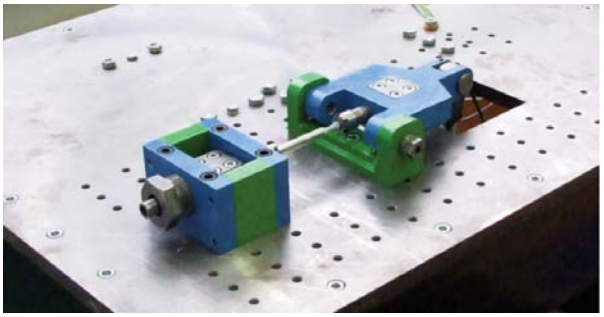

a) real equipment

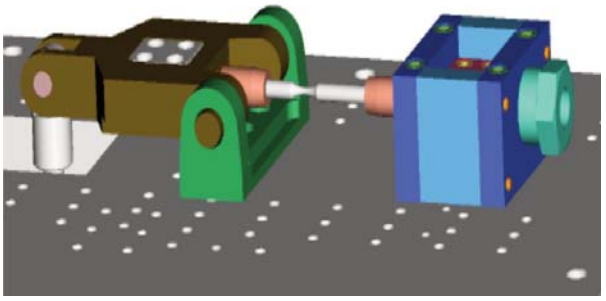

b) virtual equipment

Fig. 2 Mutiaxial fatigue loading system

3. Material characteristics

This research was conducted on an AlMgSi07.F25 aluminum alloy: the EN AW 6063-T66 aluminum alloy. The EN AW 6063-T66 is a medium strength alloy suitable for applications where no special strength properties are required. Complex shapes can be produced with very good surface quality characteristics, and suit-

Chemical composition of the EN AW 6063-T66 aluminum alloy (in weight %) according to EN 573-3 Table 1

Si	Fe	Cu	Mn	Mg	Cr	Zn	Ti	Other		Al
								Each	Total	
0.20 – 0.60	0.35	0.10	0.10	0.45 – 0.90	0.10	0.10	0.10	0.05	0.15	rest

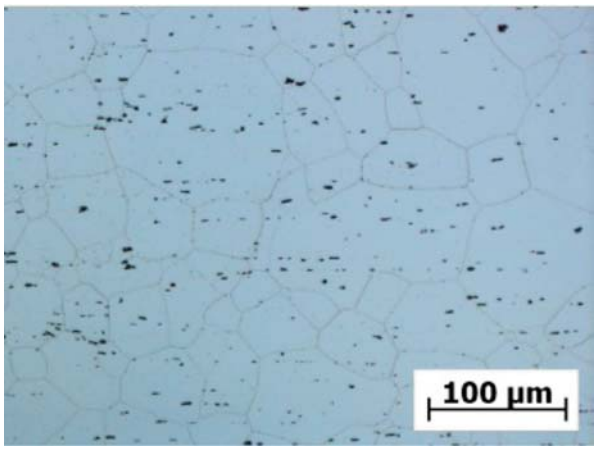

Fig. 3 Microstructure of the EN AW 6063-T66 aluminum alloy according to the rolling direction, etch. 0.5% HF

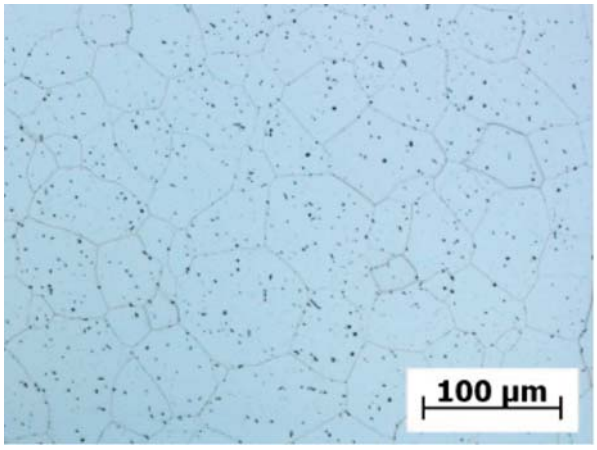

Fig. 4. Microstructure of the EN AW 6063-T66 aluminum alloy transversal rolling direction, etch. 0.5% HF

able for many coating operations such as anodizing and powder coating. The T66 treatment corresponds to solution heat-treated and then artificially aged (precipitation hardened) to a higher level of mechanical properties through special control of a manufacturing process. Such heat treatment conditions make mechanical property level higher than T6 heat treatment conditions. The typical chemical composition of the EN AW 6063-T66 aluminum alloy is shown in Table 1. The material used in this research was delivered in the form of a cylindrical shape with a diameter 10 mm. The length of cylindrical bars was 150 mm. The material was in a rolled state.

Figs. 3 and 4 illustrate a typical microstructure of the aluminum alloy evaluated in the longitudinal and transversal directions. Stretched grains are visible due to the rolling process. Also, a dispersed second phase typical of deformed and heat treated wrought aluminum alloys is observed.

Welding was conducted by the tungsten-inert gas (TIG) welding method using a Fronius Magic Wave 2200 welding machine. The used welding factors were: welding current I_z = 79 A; welding voltage U_z = 18.8 V; diameter of a wolfram electrode Ø = 2.4 mm; welding gas Ar 99.996 % with gas flow Q = 15 l.min^{-1}. Aluminum wire $AlSi_5$ with diameter Ø = 2 mm was used as welding wire material. The joint strength of TIG-welded joints was evaluated by tensile testing and fatigue testing, using the test specimens shown in Figs. 5 and 6. The hardness distribution of joints was measured along the axial center, at the weld interface and at the original material zone using a Brinell hardness tester (HBW).

The static tensile test with standard specimens performed before and after the welding process was also carried out. The results are summarized in Tab. 2. The stress-strain diagram contains engineering stresses and true stresses depending upon strain (Fig.7). For FEM analyses by ADINA true stresses were useful. Join geometry of the rod used for the welding process is shown in Fig. 8. Fig. 9 illustrates the final shape of a welded joint.

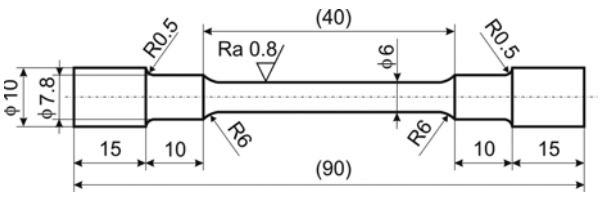

Fig. 5 Shape and dimension of tensile test specimen (dimension in mm)

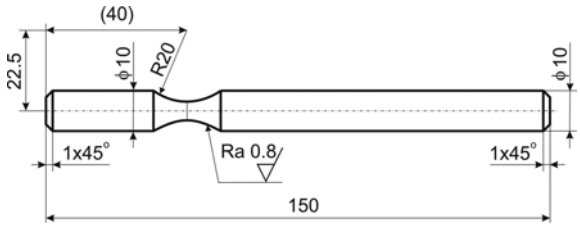

Fig. 6 Shape and dimension fatigue test specimen (dimension in mm)

Mechanical properties of the EN AW 6063-T66 aluminum alloy — Table 2.

Young modulus	62 500 MPa
Ultimate tensile strength	247 MPa
Tensile yield strength	212 MPa
Ultimate tensile strength of welded specimen	166 MPa
Tensile yield strength of welded specimen	79 MPa

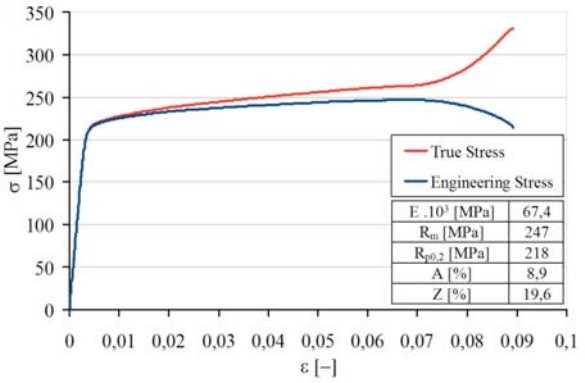

Fig. 7 Stress-strain graph for EN AW 6063

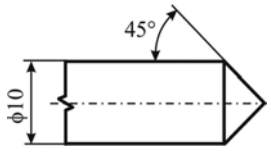

Fig. 8 Joint geometry (dimension in mm)

Fig. 9 Shape of welded joint

4. Experimental and numerical strain-life data results

Thirty smooth specimens were tested under strain controlled conditions in order to identify the strain-life behavior of the experimental material. After machining, the specimen surfaces were mechanically polished. The experiments were carried out in an electro mechanic fatigue test machine, developed at the University of Zilina. A sinusoidal waveform was used as command signal. The fatigue tests were conducted with constant strain amplitudes, at room temperature. The specimens were cyclically loaded under strain control with a symmetrical proportional bending-torsion loading, with a nominal strain ratio, $R = -1$. The computational fatigue tests were performed under in-phase cyclic loading with the zero mean value. All tests were performed under controlled bending and torsion moments. The frequency of each analysis was equal to 30 Hz.

The results, fatigue resistance (strain amplitude vs. number of cycles to failure) of tested structural material EN AW 6063-T66 before and also after the welding process (TIG) in the low cycle regime are presented in Figs. 10 and 11. In the low cycle regime of loading the strain amplitude decreases with the increasing number of cycles to failure for both series of aluminum alloy.

The first series of performed experiments (without a welding joint) were to verify fatigue behavior of low-cycle bending and low-cycle torsion loading to obtain relation between strain magnitudes versus number of cycles to failure. The second series of performed experiments (with a welding joint) were to also verify fatigue behavior of aluminum alloy EN AW 6063-T66 under low-cycle bending and torsion loading to obtain relation between strain magnitudes versus number of cycles to failure. Fig. 10 shows the results of fatigue tests with the symmetrical pure bending loading for the base material in comparison with welded joints. The specimen failure criterion during the testing was focused on the creation of fracture area more than 90% in the measured cross section of the testing rod for both series.

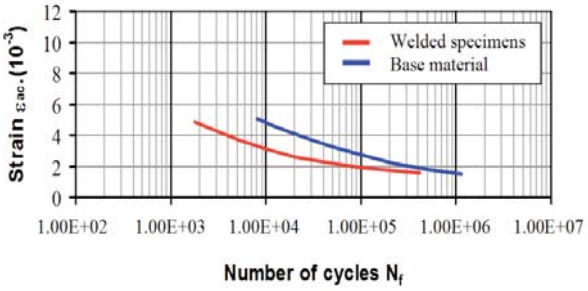

Fig. 10 Manson-Coffin curves for uniaxial low-cycle bending fatigue with phase shift 0°

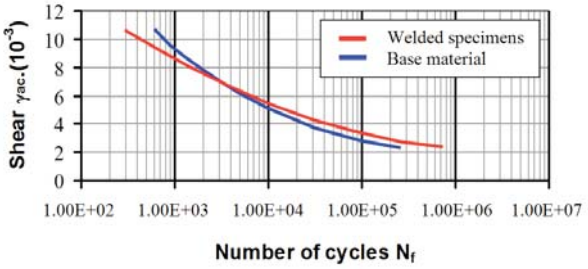

Fig. 11 Manson-Coffin curves for uniaxial low-cycle torsion fatigue with phase shift 0°

For fatigue test interpretation on each loading levels it is necessary to know the plastic strain amplitude (Manson-Coffin curve) or stress amplitude (Wohler curve) applied on each cycle loading level. For that it is necessary to analyze the stress and strain maximum values by FEM [12]. The specimen model was created by the finite-element program ADINA (see Fig. 12).

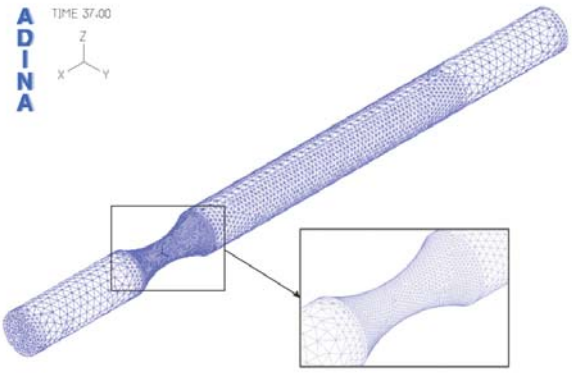

Fig. 12 Finite element model of modeled specimen

The material was assumed plastic-bilinear; the true stresses were obtained from a real stress-strain graph in Fig. 7. The tetrahedron linear element type was automatically generated. The "Load Plot" function was defined by excenter setting with excentricity 1 mm or 2 mm. At the fix point shell and beam elements were used for hammer simulating.

From the computational analysis can be seen that the area with the greatest concentration of stresses or the place with the higher deformation was localized in the middle of the rod radius (see Fig. 13).

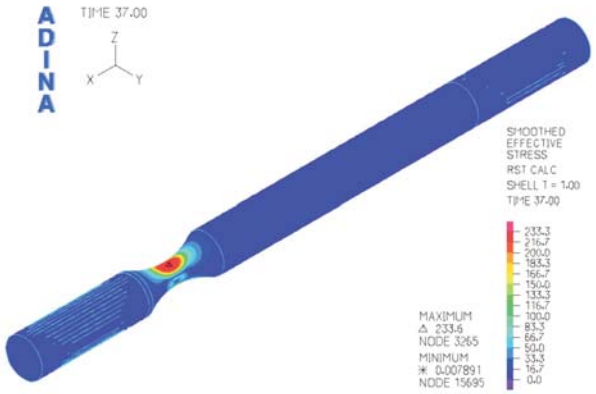

Fig. 13 Result of FEM analysis

The welding process can be simulated by numerical analyses and the obtained results (thermal field, material structure, hardness, plastic deformation, stress and strain of structure) can be used to perform effective numerical technology and manufacture process optimization. The welding simulation finite element software SysWeld will be used to solve that problem.

It belongs to the top world computational programs for full coverage to solve the welding joint problem. SysWeld was useful at the welding simulation process and also at the residual stress determination. Accurate and reliable residual stress prediction and measurements are essential for structural integrity and fatigue assessment of components containing residual stresses. Simulation of the manufacturing process using finite element technique is an accepted method for predicting the residual stresses. However, finite element simulation of residual stresses due to welding involves in general many phenomena, e.g. non-linear temperature dependent material behavior, 3D nature of the weld pool and the welding processes and microstructural phase transformation. Despite the simplification by excluding various effects, welding simulations is still CPU time demanding and complex. Hence, simplified 2D welding simulation procedures are required in order to reduce the complexity and thus maintain the accuracy of the residual stress predictions. However, the residual stress distribution for a complex welded structure is usually not known and conservative assumptions are made of the residual stress distribution when linear elastic fracture mechanics (LEFM) fatigue life predictions are carried out. The results of the residual stress and strain characterization are shown in Figs. 14 and 15.

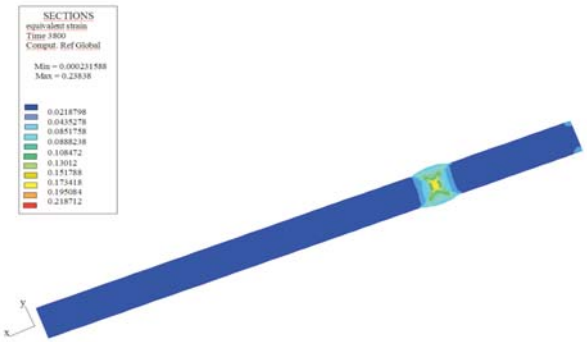

Fig. 14 Equivalent strain at the cutting plane

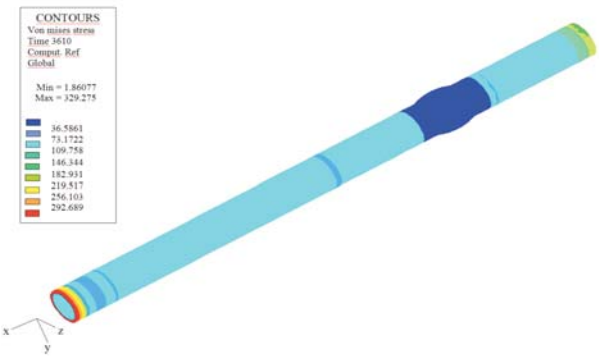

Fig. 15 Von Mises stress at the sample after snap unfix

Fig. 14 shows deformations on the top surface of the weld. To this goal it was necessary to apply a cutting plane at the welded specimen and to show deformations inside the specimen (see Fig.

15). The maximum strains outside the tick gripping are at the center of the welded joint on the meltdown border. The results of the numerical simulation have shown to presence the plastic deformation. It means that the thermal area was powerful enough for creation of residual stresses at the material.

5. Conclusion

Generally we can say that the results are in good agreement with the results published by other authors [2–6]. The differences in fatigue resistance of aluminum alloy of both series of specimens are caused by different type of loading. Fatigue under cyclic bending is not that much different in comparison with fatigue results under cyclic torsion of loading. Multiaxial fatigue strength of the welded specimens decreased in comparison with parental material, EN AW 6063-T66. The decrease in fatigue strength of the welded specimens was attributed to the stress concentration at the toe of weld.

Residual stress is an important factor influencing the structural behavior in all instability failures as well as in fatigue crack initiation and propagation when cyclic service stresses are superposed onto the residual stresses. Residual stress at the weld point was 40 MPa. Residual stresses are present in many fabricated structures due to local plastic deformation from hermal and mechanical operations during the manufacturing. The presence of residual stresses in engineering components and structures can significantly affect the fatigue behavior during external cyclic loading. The effect of residual stresses may either be beneficial or detrimental, depending on magnitude, sign and distribution of the stresses with respect to the load-induced stresses. Residual stresses in tension are detrimental and are often in the magnitude of the materials yield strength. The tensile residual stresses will reduce the fatigue life of the structure by increasing the growth of the fatigue crack, while compressive residual stresses will decrease fatigue crack growth rate. The existence of tensile residual stresses in a surface layer accelerates crack initiation reducing fatigue life due to the increase of local mean stress. An improvement in the fatigue life of the welded joints can be related to the fact that generally the T66 heat treatment produces an almost completely relief of tensile residual stresses in aluminum alloy weldments. Therefore the slope of fatigue curves in Figs. 10 and 11 are similar.

Acknowledgements

This work has been supported by VEGA grant No. 1/1089/11 and No. 1/0125/09.

The authors gratefully acknowledge this support.

References

[1] TREBUNA, F., BURSAK, M.: *Medzne stavy, lomy [Limiting States and Fractures].* Grafotlac, Presov, 2002. ISBN 807165-362-4.
[2] LEGER, J.: *Fatigue Life Testing of Crane Drive Shafts under Crane-Typical Torsional and Rotary Bending Loads.* Schenck Hydropuls Mag., No. 1, pp. 8–11, 1989.
[3] BANNANTINE, J. A., SOCIE, D. F.: A Multiaxial Fatigue Life Estimation Technique. In: *Advances in Fatigue Lifetime Predictive Techniques,* ASTM STP 1122. Eds: M. R. Mitchell a R. W. Landgraf. Philadelphia, American Society for Testing and Materials, pp. 249–275, 1992.
[4] GOUGH, H. J., POLLARD, H. V.: *Some Experiments of the Resistance of Metals to Fatigue under Combined Stresses,* Part I., Min. of Supply, Aero Res. Council, RSM 2522, 1951.
[5] MATHERS, G.: *The Welding of Aluminium and its Alloys.* Published by Woodhead Publishing Limited, Abington Hall, Abington Cambridge CB1 6AH, England, ISBN 0-8493-1551-4, 2002.
[6] BLATNICKY, M.: *Doctoral thesis.* University of Zilina, 2011.
[7] ZMINDAK, M., NOVAK, P., MESKO, J.: Numerical Simulation of arc Welding Processes with Metallurgical Transformations. *Metallurgy,* vol. 49, No. 2, pp. 595–599, ISSN 0543-5846, 2010.
[8] SAPIETOVA A., DEKYS V., VASKO M.: A Numerical Model of Rotating Machine Having Unbalance and the Measurements of its Dynamical Properties. *Metalurgija (Metallurgy)*, vol. 49, No. 2, pp. 503–507, ISSN 0543-5846, 2010.
[9] MADDOX, S. J.: *Fatigue Strength of Welded Structures,* Second Edition, Woodhead Publishing, UK, ISBN 978-1855730137, 1991.
[10] JAKUBOVICOVA, L., KOPAS, P., HANDRIK, M., VASKO, M.: *Computational and Experimental Analysis of Torsion and Bending Loading of Specimen.* Intern. Conference on Innovative Technologies, Prague, pp. 395–400, ISBN 978-80-904502-2-6, 2010.
[11] SAGA M., KOPAS P., VASKO M.: *Some Computational Aspects of Vehicle Shell Frames Optimization Subjected to Fatigue Life.* Communications – Scientific Letters of the University of Zilina, vol. 12, No. 4, pp. 73–79, ISSN 1335-4205, 2010.
[12] BATHE, K. J.: *Finite Element Procedures.* New Jersey, Prentice Hall, 1982.

Pavol Novak – Milan Zmindak *

A NEW FILLING MATERIAL FOR COLD SLEEVE

The aim of this paper is to review material properties of a new filling material for cold sleeve. The first experimental measurements were performed on samples to determine required material properties. Then the structural analysis was performed for a pressurized pipe with insufficiently welded root and installed cold sleeve. The case of depressurized pipes that could cause a breach of cohesion between the filling material and surface of pipe or sleeve with the usage of cohesive finite elements was simulated.

Keywords: *Repairing pipes, cold sleeve, stress of welded joint, cohesive finite elements*

1. Introduction

Older metal pipelines have a lot of different types of material failures or defects [1]. Defects are identified during different actions on the pipelines, as are internal inspection methods, or other activities as making control probes, pipeline rehabilitation, searching gas-escape and similarly. Comparable carrying capacity of repair of the damaged pipe with the pipe without disturbance can be achieved by applying steel sleeves filled with composite epoxy [2]. Repairing the pipes with cold sleeve can reduce stresses at failure, and provide sufficient corrosion resistance of pipelines for the next operation. The disadvantages of these methods are low resistance and low axial tensions security protection in case of pressure medium seepage and short lifetime repairs. Installation of the proposed sleeve takes place in the full operation of the pipeline. The repaired segment of the pipeline is cleaned from the original coating. For maximum adhesion between a polymer filler and pipe surface or surface of the sleeve, these surfaces are cleaned. Subsequently, the two halves of the sleeve are mounted on the pipe and the space between the sleeve and the pipeline is defined by distance prisms. Then the sleeve is welded by the classical "V" weld and is sealed with a bandimex clamp and shrink wrap (Fig. 1). The tension spring creates space and conditions for a continuous, integral filling of the space between the sleeve and the repaired pipe. Finally, by using the filler the space between the sleeve and the pipe is filled by polymer. This type of sleeve is used for the repair of insufficiently welded roots too.

2. Problem formulation

For accurate reproduction of the stress state for all components of the cold sleeve, the procedure of cold sleeve installation has to be simulated. During the cold sleeve installation the pipeline is loaded by internal gas pressure and axial force. The cold sleeve and polymer adhesive are at stress-free state at this time. The cold sleeve and polymer are stressed when we change the value of internal pressure.

The polymer material used in the cold sleeve is based on PROTEGOL polymer. We note that PROTEGOL is polymer successfully used as anticorrosion protection on steel pipes and constructions placed under ground. It is one of the materials with the highest quality which is used for the rehabilitation of transit pipeline.

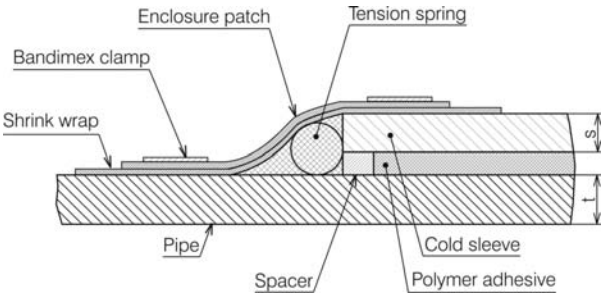

Fig.1 Cross-section of installed cold sleeve

The size and shape of the weld is created in compliance with the norm STN 131075 (Slovak technical norm). In Fig. 1 is a cut through the pipe with a cold sleeve installed. For simulation the pipes with diameters 1220 and 1420 mm are considered.

The material properties of PROTEGOL based polymer were experimentally measured and the two-parameter Mooney-Rivlin hyperelastic constitutive model was used [3]. The quality of adhesion between the polymer layer and pipe or sleeve was characterised

* **Pavol Novak, Milan Zmindak**
Department of Applied Mechanics, Faculty of Mechanical Engineering, University of Zilina, E-mail: pavol.novak@fstroj.uniza.sk

by the DPARAM parameter. The value of this parameter lies between 0 and 1 where 0 or 1 represents total adhesion or total separation of adjacent surfaces. Critical values of the DPARAM parameter were obtained when the pipe depressurisation occured.

3. Experimental tests

To get the material data needed to perform the finite element (FE) simulation, two experimental tests were made. The first of these was the tensile test of the modified polymer PROTEGOL. The tensile test was carried out in accordance with standard norm BS EN 10002-1. The results of this test are shown in Fig. 4 and they exhibit the statistical behavior of the specimens with a large variance of maximum force. The maximum force required to break the specimen was in the range ⟨200, 500⟩ N. The main reason for the large scatter of values is, in our opinion, the sensitivity of testing samples to humidity and temperature of the mixture during solidification. This affects the density and size of the bubbles contained

Fig. 2 Test sample

Fig. 3 Tearing of the test specimen

in the sample. They act as stress concentrators. These factors are difficult to maintain the necessary limits in the application of technology in the exterior.

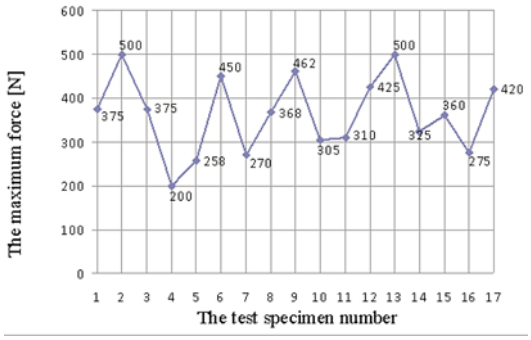

Fig. 4 Tensile test results

The next test was the tearing test. For this test cylindrical specimens were used (Fig. 2). The specimen was attached to the ZWICK tensile machine. Fig. 3 displays the tearing of the specimen in the tensile machine. The tearing test results showed the same behavior as the tensile test results. The maximal tearing force was 4150 N and minimal tearing force was 2153 N (Fig. 5).

4. Finite element simulation

Modeling with the finite element method was used to obtain stress state of all parts and risk assessment of debonding. The ANSYS Mechanical APDL was used for numerical simulation. The analysis was performed on the pressurized pipe with a subsequent depressurization to atmospheric pressure. The operating pressure was 7.35MPa. Based on the above given tests, we decided to use a two-parameter Mooney-Rivlin hyperelastic constitutive model for polymer. To determine the parameters of the Mooney-Rivlin model we broke 10 specimens. Additional three samples were used to tune the attachment to tensile testing machine and 4 specimens for optical tuning of the spray for the system ARAMIS [4]. From the performed FEM calculations we evaluated the separation of polymer from the surface of the pipe and the sleeve using the parameter d_n or DPARM.

We used the axisymmetric FE model with additional plane symmetry. For the steel parts PLANE183 element was used [5]. This element has a quadratic displacement behavior. For the polymer part PLANE182 element was used. This element has a linear displacement behavior. The combination of PLANE183 element with the two-parameter Mooney-Rivlin model had convergence problems. Contact elements CONTA171 and TARGE169 with a cohesive zone material (CZM) model were used to simulate debonding of adjacent surfaces. The CZM model consists of a constitutive relation between the traction T acting on the interface and the corresponding interfacial separation δ (displacement jump across the interface). We used the mode I dominated bilinear CZM model which assumes that the separation of the material interfaces is dominated by the displacement jump normal to the interface, as shown in Fig. 6. The point A with coordinates [σ_{max}, $\bar{u}_n$] represents start of delamination and corresponds to DPARAM = 0. The slope Kn is normal cohesive stiffness. The point C with

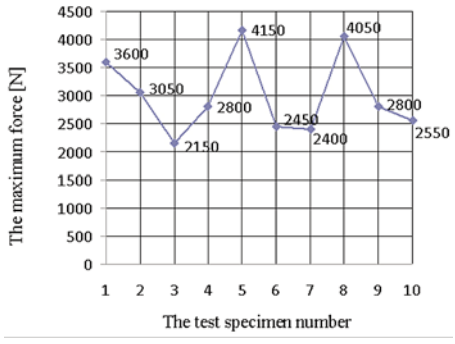

Fig. 5 Tearing force

coordinates [0, u_n^c] belongs to total separation of adjacent surfaces and corresponds to DPARAM = 1. The partial delamination represents point B. In this case the $K_n(1 - d_n)$ normal cohesive stiffness is used.

The simulation consists of two steps. In the first step only the pipeline under internal pressure was solved. The radial displacement was stored in the parameter and saved to disk. This parameter was used in a second step to modify geometry of the cold sleeve. This is necessary because the gap between the pipe and sleeve shall be defined in the pressurized pipeline. The second step consists of three substeps. In the first substep the complete model was solved (pipe with the installed cold sleeve) with internal pressure and axial force applied. In the second substep element kill/birth technique was used to ensure a stress-free state of the polymer filling and cold sleeve. In the last substep a depressurizing pipeline was simulated.

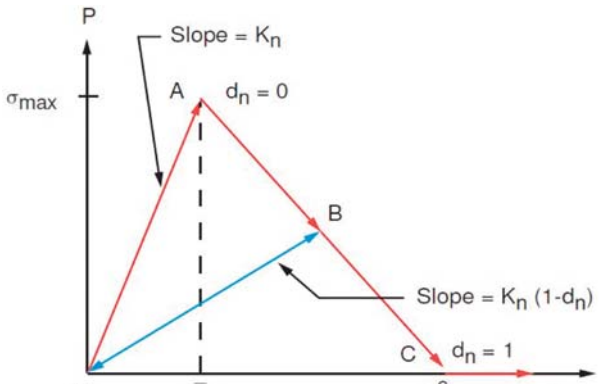

Fig. 6 Normal contact stress and curve of contact gap for bilinear mode I dominated CZM model

The simulation was executed for three geometric variants: variant 1 – pipe Ø1220 mm, thickness 15.9 mm, variant 2 – pipe Ø1220 mm, thickness 13.5 mm and variant 3 – pipe Ø1420 mm, thickness 15.6 mm. For all three geometric variants the thickness of the cold sleeve was 12 mm and the thickness of a polymer layer was 8 mm. To simulate the worst case scenario for debonding, material properties of the modified polymer were selected in this way: measurement with the highest stiffness for the Mooney-Rivlin model and measurement with the lowest tearing force for the CZM model (2153 N). The applied statically determined boundary conditions are described in Fig. 7. Gas pressure load is marked by red colour in Fig. 7.

Another load that needed to be considered was the axial load due to gas pressure in the closed pipe. This load is calculated as $FO = p \,.\, S$, where S is a cross sectional area of the pipe. For the pipe with outer diameter D = 1220 mm and thickness t = 15.9 mm the resulting applied load is FO = 7.35 × 3.14× 594.1**2 = 8.146.106 N. The pipe and sleeve are made from steel 11 523 (S355J0). Elasticity modulus in tension is E = 206.0 GPa, Poisson's number is 0.30 and yield strength is 395 MPa. In Fig. 8 is a graph of engineering strain-stress for polymer PROTEGOL. The maximum strain is approx. 64 % and maximum stress is approx. 4.5 MPa. The blue curve represents the measurement and pink curve represents the two-parameter Mooney-Rivlin approximation.

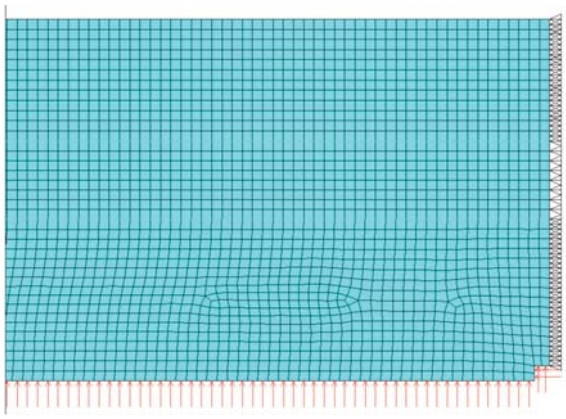

Fig. 7 Boundary conditions

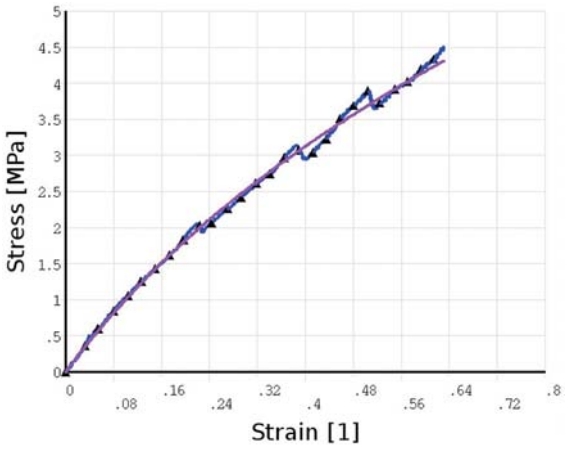

Fig. 8 Engineering stress - strain curves

The FEM calculation was performed as a geometric nonlinear analysis with elasto-plastic material properties of the pipe and sleeve [6].

5. Analysis results

In terms of the limit state of the load carrying capacity, vessels or piping are appreciated in terms of the primary stresses which are the results of acting a pressure in the piping. Table 1 summarizes the most important results of the analyses. It can be seen that the maximum value of the von Mises stress is 392 MPa. This value reaches almost the yield strength and occurs in the tip of the insuf-

ficiently welded root. It is a singularity caused by a sharp corner, i.e. transition between the pipe and the insufficiently welded root. Fig. 9 shows the distribution of the contact gap between the polymer layer and the piping and the cold sleeve. The minus sign represents the separation of the adjacent surfaces. The cohesive failure is needed to reach the value of the contact gap −2.5 mm. Fig 10. shows the detail of the contact gap at the cold sleeve beginning.

From Tab.1 it can be seen that the most critical variant of tearing is geometric variant 2. The value of DPARAM = 0.669 and contact gap is - 0.100 mm.

Results in MPa for operating pressure p = 7.35 MPa Tab.1

		Variant 1	Variant 2	Variant 3
Radial displacement (u_r) [mm]		−0.544	−0.641	−0.758
Radial stress (σ_r)	Depressurized	3.812	5.609	6.04
	Pressurized piping	90.826	112.037	107.729
Circumferential stress (σ_t)	Depressurized	−121.059	−130.894	−145.38
	Pressurized piping	347.888	414.005	412.931
Axial stress (σ_A)	Depressurized	−31.09	−35.957	−37.031
	Pressurized piping	282.299	339.009	339.089
Von Misses stress $(\sigma_A)_{max}$	Depressurized	123.102	131.233	147.416
	Pressurized piping	329.108	391.191	391.627
Contact gap [mm]		−0.060	−0.100	−0.086
D-param [1]		0.418	0.669	0.569

Sensitivity analysis considering changes to the thickness of the polymer layer and thickness of the sleeve was performed. The thickness of the polymer layer was varied in the range of 4–8 mm in increments of 0.5 mm. Fig. 11 shows the influence of the thickness of the polymer layer on the DPARAM parameter. This dependence is weak for a technologically useful range of the polymer layer thickness.

Other behavior of the DPARAM parameter is observed when we change the thickness of the sleeve. In this case, we carried out 15 variants with altered thickness calculation sleeve in the range of 5–12 mm in increments of 0.5 mm. Fig. 12 shows the DPARAM parameter dependence on the sleeve thickness. This proportionality is very strong for the range of sleeve thickness from 9 mm to 12 mm.

6. Conclusion

On the basis of the mentioned results we can conclude that repairing anomalous welds by means of the cold sleeve with a modified polymer PROTEGOL is safe with respect to a tearing polymer. With regard to the limit state, the pipeline, as well as the sleeves, are loaded in an elastic domain under the yield strength of the used steels. Since the problem was solved as a nonlinear problem with elastic-plastic behavior of materials, the results of the numerical simulation proved that plastic strains neither of the pipeline nor of the sleeve were reached.

Acknowledgement

The research work is partially supported by the Project of the Structural Funds of the EU, Operational Program Research and Development, Measure 2.2 Transfer of knowledge and technology from research and development into practice:

Title of the project: Development of Optimal Technology for the Analysis of the Limit States of Structural Elements in Contact, ITMS code: 26220220118.

We support research activities in Slovakia/Project is cofunded from sources of ES.

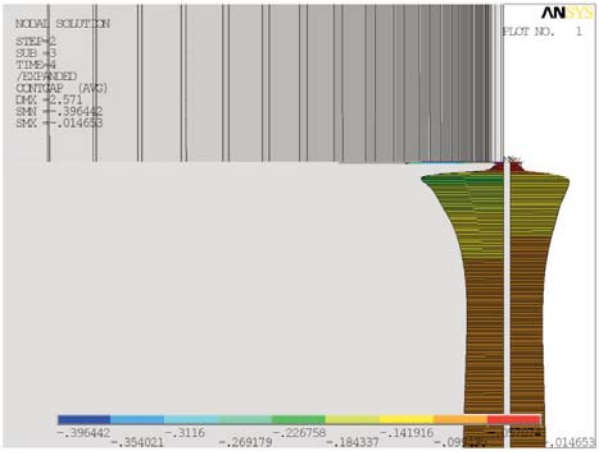

Fig. 9 Distribution of contact gap [mm] for variant 2, p = 7.35 MPa

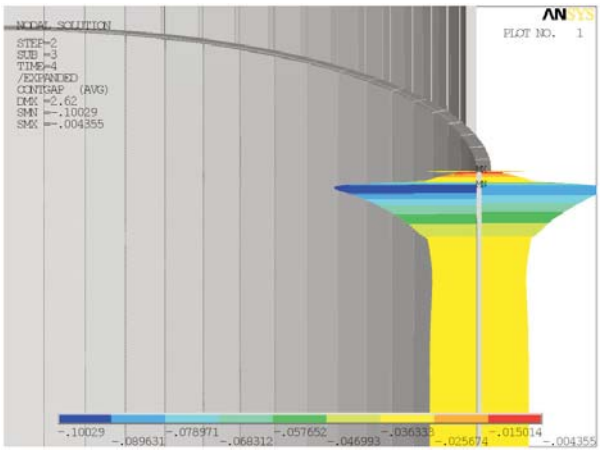

Fig. 10 Detail of distribution of contact gap [mm] for variant 2, p = 7.35 MPa considering axial force

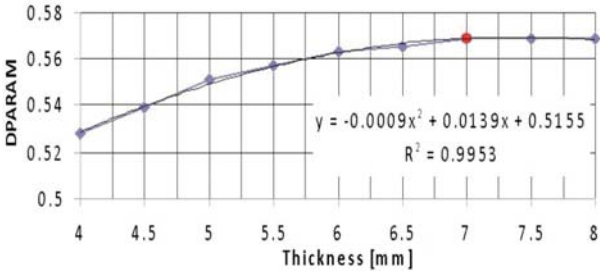

Fig. 11 Graph DPARAM vs. polymer thickness

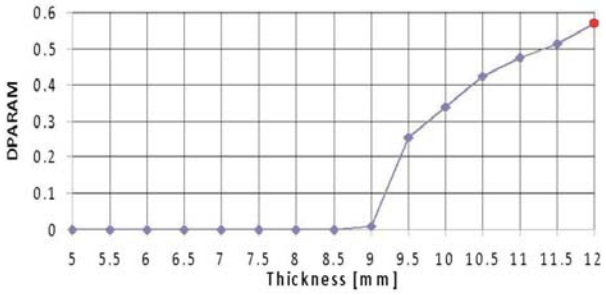

Fig. 12 Graph DPARAM vs. sleeve thickness

References

[1] KOPAS P., HANDRIK M., JAKUBOVICOVA L., SAGA, M.: Computational Simulations of Stress Distribution in Surrounding of Graphite Particles. *Machine Dynamics Research,* 2010, No. 3, Vol. 34, p. 115–123, ISSN 2080-9948.

[2] ZMINDAK, M., RIECKY, D.: Meshless modelling of laminate Mindlin plates under dynamic loads. *Communications - Scientific Letters of the University of Zilina,* 2012, vol. 14, No. 3, pp. 24–31, ISSN 1335-4205.

[3] ANSYS Release 11.0: Theory reference for ANSYS and ANSYS Workbench. ANSYS, Inc., 2007.

[4] ARAMIS – User information hardware, GOM MbH, www.gom.com.

[5] ANSYS Release 11.0: Element Reference. ANSYS, Inc., 2007.

[6] ANSYS Release 11.0: Structural Analysis Guide. ANSYS, Inc., 2007.

COMMUNICATIONS – Scientific Letters of the University of Zilina
Writer's Guidelines

1. Submitted papers must be unpublished and must not be currently under review for any other publication.
2. Submitted manuscripts should not exceed 8 pages including figures and graphs (in Microsoft WORD – format A4, Times Roman size 12, page margins 2.5 cm).
3. Manuscripts written in good English must include abstract and keywords also written in English. The abstract should not exceed 10 lines.
4. Submission should be sent: By e-mail – as an attachment – to one of the following addresses: komunikacie@uniza.sk or holesa@uniza.sk (or on CD to the following address: Zilinska univerzita, OVaV – Komunikacie, Univerzitna 1, SK-10 26 Zilina, Slovakia).
5. Uncommon abbreviations must be defined the first time they are used in the text.
6. Figures, graphs and diagrams, if not processed in Microsoft WORD, must be sent in electronic form (as JPG, GIF, TIF, TTF or BMP files) or drawn in high contrast on white paper. Photographs for publication must be either contrastive or on a slide.
7. The numbered reference citation within text should be enclosed in square brackets. The reference list should appear at the end of the article (in compliance with ISO 690).
8. The numbered references (in square brackets), figures, tables and graphs must be also included in text – in numerical order.
9. The author's exact mailing address, full names, E-mail address, telephone or fax number, the name and address of the organization and workplace (also written in English) must be enclosed.
10. The editorial board will assess the submitted paper in its following session. If the manuscript is accepted for publication, it will be sent to peer review and language correction. After reviewing and incorporating the editor's comments, the final draft (before printing) will be sent to authors for final review and minor adjustments
11. Submission deadlines are: September 30, December 31, March 31 and June 30.

COMMUNICATIONS

SCIENTIFIC LETTERS OF THE UNIVERSITY OF ZILINA
VOLUME 14

Address of the editorial office:
Zilinská univerzita
Office for Science and Research
(OVaV)
Univerzitna 1
SK 010 26 Zilina
Slovakia

E-mail: komunikacie@uniza.sk

Each paper was reviewed by two reviewers.

Journal is excerpted in Compendex and Scopus.

It is published by the University of Zilina in
EDIS – Publishing Institution of Zilina University
Registered No: EV 3672/09
ISSN 1335-4205

Published quarterly

Single issues of the journal can be found on:
http://www.uniza.sk/komunikacie